Important Notice

UNIVERSITY OF CALGARY

Estimation of Shear wave velocities from P-P and P-S seismic data

using Equivalent Offset Migration.

by

Thais Guirigay

A THESIS

SUBMITTED TO THE FACULTY OF GRADUATE STUDIES

IN PARTIAL FULFILMENT OF THE REQUIREMENTS FOR THE

DEGREE OF MASTER OF SCIENCE

DEPARTMENT OF GEOSCIENCE

CALGARY, ALBERTA

SEPTEMBER, 2012

Abstract

Prestack migration of converted wave data requires accurate acoustic and shear wave velocities V_p and V_s. This thesis presents new methods to estimate the shear velocities using a single converted wave velocity Vc, that combines V_p and V_s.

The acoustic velocity V_p, and a constant value for the V_p/V_s ratio are used to make an initial estimate of the converted wave velocity, V_c. Narrow range gathers are formed using the initial estimate of V_c that are then processed to obtained a refined value of V_c. This refined value is then used to estimate V_s. The estimated V_s is used with V_p in a full prestack migration using the equivalent offset method (EOM) to form complete prestack migration gathers. Velocity analysis of these gathers produces a more accurate V_c which is used to complete the prestack migration.

The quality of the method is demonstrated for the cases of one synthetic dataset and two real datasets. The results show superior imaging when compared with alternative migration algorithms.

Acknowledgements

To my husband Rafael, my sons Rafael David and Daniel Roberto, and those who believed in me.

Table of Contents

List of Tables

List of Figures and Illustrations

List of Symbols, Abbreviations and Nomenclature

Symbol	Definition
1C	One component
2D	Two-Dimensional
3C	Three components
3D	Three-Dimensional
μ	shear modulus
ρ	density
γ	Ratio of incident to reflected wave velocity
kg	kilograms
km	kilometers
m	meters
m/s	meters by seconds
msec	milliseconds
sec	seconds
t	time
C	Converted wave data, same as P-S
C-EOM	Converted Wave Equivalent Offset Migration
CREWES	Consortium for Research in Elastic Wave Exploration Seismology
ACCP	Asymptotic Common Conversion Point
AGC	Automatic Gain Control
AVO	Amplitude variation with offset
CCP	Common Conversion Point
CCSP	Common Conversion Scatterpoint
CMP	Common Midpoint
CRS	Common Receiver Stack
CSP	Common Scatterpoint
EO	Equivalent Offset
EOM	Equivalent Offset Migration
DSR	Double Square Root
Hz	Hertz
K	Bulk modulus
LCCSP	Limited Converted Wave Common Scatterpoint
MP	Midpoint
NEBC	Northeastern British Columbia
NMO	Normal Moveout
P	Compressional wave
P-P	Compressional reflected to compressional
P-S	Compressional reflected to Shear, same as C
RMS	Root-mean-Square
SP	Scatterpoint
SH	Transverse polarization of shear wave
SV	Radial polarization of shear wave

U of C	University of Calgary
Vave	Average velocity
Vc	Converted wave velocity
VInt	Interval velocity
Vmig	Migration velocity
Vp	Compressional wave velocity
Vrms	Root-mean-square velocity
Vs	Shear wave velocity
VSP	Vertical Seismic Profile
WCSB	Western Canada Sedimentary Basin

Chapter One: **Introduction**

1.1 Background

Seismic exploration, in the search for hydrocarbons, has been concentrated predominately with acoustic or P-wave seismic reflection surveys for many reasons. The reasons include the fact that the P-waves arrive first, they have high signal-to-noise ratios, the particle motion is close to rectilinear, they are easily generated by a variety of sources, and propagate in fluid (Stewart et al., 2002).

Many basins around the world are or will soon be in a mature stage, and it has become necessary to understand and extract more information from the full elastic wavefield that involves both the P-wave mode and the S-wave mode (Stewart, 1994). This information is required to optimize the investment, reduce risks, and estimate the reservoir characteristics, such as porosity, lithology, and pore fluid distributions.

An S-wave survey offers some advantages as it responds to different characteristics. However, this method has some limitations: it is not applicable in some environments such as marine or transition zones that do not propagate S-waves in a fluid, and its acquisition is expensive. It may also produce a poor S-wave section in comparison with a P-wave section.

A more economical method to collect S-wave information is to use mode converted waves. Energy arriving at a reflector or interface may be converted to an alternate mode. If the incident wave is a P-wave, then some of the energy could be converted into S-waves that are also reflected, and transmitted. Recording these converted waves (P-S) is referred to as a P-S survey and is a good alternative to an S-wave survey. P-S-wave surveys are less expensive than P-wave surveys as they only use a P-wave source. Both require 3 component receivers. This type of survey has more applications than conventional P-wave surveys, including application such as

1

structural imaging, lithologic estimation, anisotropy analysis, fluid description, and reservoir monitoring (Stewart et al., 2003).

1.1.1 Body waves

There are two types of body waves that can propagate through the body of an elastic solid: compressional, and shear waves.

Compressional waves (also called longitudinal, primary, or P-waves), "propagate by compressional and dilatational strains in the direction of the wave travel" (Kearey and Brooks, 1999). The velocity of propagation, V_p, of a body P-wave in any material is determined by the density ρ, the bulk modulus K, and shears modulus μ, and is given by:

$$V_p = \left(\frac{K + \frac{4}{3}\mu}{\rho}\right)^{\frac{1}{2}}. \tag{1-1}$$

Shear waves (also called transverse, secondary or S-waves) "propagate by a pure shear strain in a direction perpendicular to the direction of wave travel" (Kearey and Brooks, 1999). The velocity of a shear body wave V_s is determined by the density, and the shear modulus only, and is given by:

$$V_s = \left(\frac{\mu}{\rho}\right)^{\frac{1}{2}}. \tag{1-2}$$

In an isotropic medium, where the velocity is independent of the direction, the P-wave velocity may be treated as a scalar quantity, while S-wave propagation is a vector quantity. Therefore, S-waves may contain more information than P-waves. This information can be described in terms of its particle motion. The particle motion associated with P-wave propagation is oriented in the direction of propagation that is defined by the ray geometry.

In an S-wave, particle motion is oriented perpendicular to the direction of propagation. The particle motion can be in any direction within the plane normal to the ray and is described by two orthogonal coordinates in the plane. These two coordinates are used to describe the polarization of the S-wave particle motion (Tatham and McCormack, 1998).

Figure 1.1 shows the geometry of ray propagation and polarization direction for P- and S-waves reflected from a horizontal interface. Figure 1.1a shows a P-wave source as a vertical impulse on the surface, and a raypath is reflected, and then recorded at the surface. The particle motion is parallel to the propagation direction, i.e. in the direction of the ray, which lies in the vertical plane defined by the source and receiver (Tatham and McCormack, 1998).

For S-wave propagation, the source-receiver geometry has a considerable effect on the polarization. A horizontal impulse oriented perpendicular or transverse to the line is referred to as an SH-wave source. The particle motion is normal to the ray propagation direction and normal to the vertical plane defined by the source, receiver, and reflection point, as is shown in Figure 1.1b. (Tatham and McCormack, 1998).

If the horizontal source impulse is oriented in the in-line direction, or parallel to the seismic line direction, as shown in Figure 1.1c, the source generates in-line SV-waves, or SV-waves with radial polarization (Tatham and McCormack, 1998). The particle motion is perpendicular to the raypath, and the particle motion is entirely in the vertical plane of incidence.

1.2 Vp/Vs

The velocity of the P-wave and the S-wave is governed by the properties of the rock through which they travel. They can be identified from samples of rock in a laboratory, or from well logs. Other independent measurements can be made from data, such as vertical seismic profile (VSP), or P-wave and S-wave seismic sections. The relationship of these values to

various rocks can provide useful information about reservoir rock properties (Tatham and McCormick, 1998).
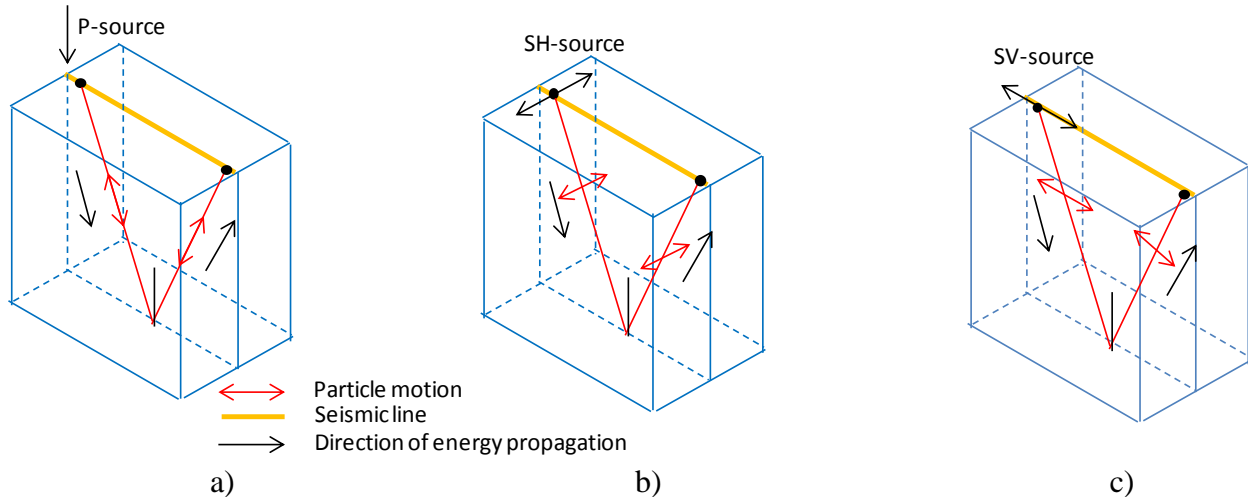
Figure 1.1: Description of geometry of ray propagation and polarization direction for P- and S-wave reflection from a horizontal interface. After Tatham and McCormack, 1998

Many authors have described relations between lithology and seismic velocities. Pickett (1963) found that clean, well-consolidated sandstone, dolomite and limestone could be distinguishing from each other using *Vp/Vs* values. Domenico (1977) found that the ratio *Vp/Vs* can be used as a lithology discriminator between sandstone, calcareous sandstone, shale, limestone and dolomite, and showed that V_p and V_s are higher for clean sandstones than shale sandstones.

Han et al. (1986) indicated that P- and S-wave velocities and the V_p/V_s ratio decrease with increasing porosity over a range of lithologies, burial depths, and pore fluid saturation.

The effect of different hydrocarbon saturations on V_p *and* V_s also has been studied. V_p/V_s is also an excellent indicator of gas saturation in the pore space (Tatham and McCormick, 1998, Castagna et al., 1993, Stewart, 1994). Murphy (1984) found that V_p and V_p/V_s decrease as gas saturation increases in tight sandstones. V_p/V_s could decrease as much as 30 % in consolidated rocks with increasing gas saturation (Gregory, 1976). *Vp/Vs* is much lower (10-20 %) for gas

saturation than for liquid saturation. Castagna et al. (1985) show that in wet sandstones V_p/V_s decreases with increasing V_p.

Other authors have found relations between seismic velocities and depth of burial. Nur and Simmons (1969), and Wang and Nur (1987), have related increasing V_p and V_s values with increasing depth. Sandstone V_p/V_s values vary more with increasing depth than the limestone V_p/V_s values do.

The effect of consolidation on V_p and V_s is "not easy to quantify because there are many physical changes in the sediments during this process" (Tatham and McCormick, 1998). V_p/V_s is often large in near-surface unconsolidated sediments (from 3 to 10) but rapidly decrease with depth. At depths greater than 10000 ft, quartz sandstones have V_p/V_s values between 1.5 to 1.7, and carbonates range from 1.8 to 1.9.

The effects of temperature on P- and S-wave velocities also have been reported in the literature. Timur (1977) reported that "for a large set of sedimentary rocks, the average decrease in velocities was 1.7 percent for P-waves and 0.9 percent for S-waves for a 100° C rise in temperature". The effect of temperature on oil-saturated sandstone have been reported by Tosaya et al. (1984), which suggested that for a 100° C increase, both P- and S-wave velocities decrease about 35 percent.

1.3 Thesis objectives

The main objective of this thesis is to find a simple method for estimating the converted or P-S wave velocity V_c, and the shear wave velocity V_s, using P-P and P-S wave data, and then use them with a migration algorithm known as Equivalent Offset Migration. A 2D converted wave prestack migration by equivalent offsets is developed and implemented. These methods will be tested on a synthetic dataset and two real datasets.

1.4 Datasets used

1.4.1 Synthetic dataset

The Channel Model was created in 2008 by CREWES (Margrave et al., 2008, Lloyd and Margrave, 2010) as a 3D volume of P- and S-wave velocity and density. The layer velocities and depth were based on the Bow River in Calgary, Alberta. One 2D line was extracted from the 3D volume for this thesis. The line has an N-S orientation and intersects the channel. More details are discussed in Chapter 4.

1.4.2 Hussar data set

This seismic data were acquired by CREWES in collaboration with Husky Energy, GeoKinetics, and Inova in September 2011. In addition to the seismic data, well log information with compressional and shear logs were also used. These data are from the Hussar area, Alberta, approximately 50 miles east of Calgary. The line is 4.5 kilometers and runs to NE-SW. This dataset is further described in Chapter 4.

1.4.3 Northeastern British Columbia data set

This data set was acquired by GeoKinetics for Nexen Inc in March 2011 as a refraction survey to provide a detailed description of the near-surface P- and S-wave velocity-depth structure in Northeastern British Columbia (NEBC). The dataset was processed by Sensor Geophysical. Compressional sonic logs and shear sonic logs from a well in the survey area are taken over the entire length of the wellbore (from 40 m to 2054 m). More details on this dataset are given in Chapter 4.

1.5 Software used

Most basic processing of the data used in this thesis was performed using VISTA software provided by Gedco and ProMax provided by Landmark Graphics Corporation.

MatLab was used to compute V_c and V_s, compute common scatterpoint gathers with the EOM code. MatLab code from the CREWES toolbox was also used.

All figures in this thesis were editing using Microsoft PowerPoint, and the text was processed using Microsoft Word.

1.6 Thesis outline

This thesis reviews the P-S method, the development of two methods to estimate V_c and V_s, and then demonstrates their application in various datasets.

Chapter 2 is a review of the fundamental concepts. It starts with a review of the P-S mode conversion and then considers P-S wave processing. After that, a review of conventional poststack and prestack migration is presented. A summary of Kirchhoff Prestack Migration concepts base on the Cheops pyramid is shown. The concepts of Equivalent Offset Migration and of a scatter point are explained.

Chapter 3 contains my theoretical contributions for estimating and using a single converted wave velocity V_c and using it to form prestack migration gathers , which are then used to estimate the shear wave velocities, for a complete prestack migration of converted wave data using the equivalent offset method.

A collection of examples that demonstrate the application of the new concepts and analysis are presented in chapter 4.

In Chapter 5, the conclusions of this thesis and recommendations for future work are presented.

1.7 My contributions

1. Prepare seismic data using the VISTA seismic processing software to form CCSP gathers.

2. Perform velocity analysis, stack and evaluate the CCSP gathers to produce a refined estimated of V_c and V_s.

3. Create prestack migrations from CSP gathers and test for parameters.

4. Develop the theory for using converted wave velocities of forming initial estimation of V_c.

5. Testing and evaluation results.

Chapter Two: **Review of current method**

2.1 Converted wave overview

Tessmer et al. 1988 have discussed the geometry of P-S wave raypaths and the problem associated with the gathering of converted-wave data

P-S waves usually have a P-wave source, convert to S-waves at a reflector, and are then recorded at the surface. P-S surveys use conventional sources, but require several times more recording channels per receiving location, and some special processing. The data quality of modern P-S sections approach and in some cases exceeds the quality of conventional P-P seismic data (Stewart et al., 2002).

The reflection/refraction/transmition of acoustic waves has been visualized as a simple geometry problem following Shell's law and a partitioning of energy between the reflected /transmitted energy across an interface between two media of contrasting acoustic properties. In an elastic medium, the problem is more complex, because it involves mode-conversion from P- to S-wave, or S- to P-wave, associated with both the reflection and refraction process.

Figure 2.1 shows the simplest elastic case of a P-wave striking a horizontal interface between two elastic solids. Four different waves are generated as result of the interaction of a single P-wave with the interface: a reflected P-wave, a reflected mode-converted SV-wave, a transmitted/refracted P-wave, and a transmitted/refracted S-wave. V_{p1} and V_{s1} are the P- and S-wave velocities for the first medium. V_{p2} and V_{s2} are the P- and S-wave velocities for the second medium.
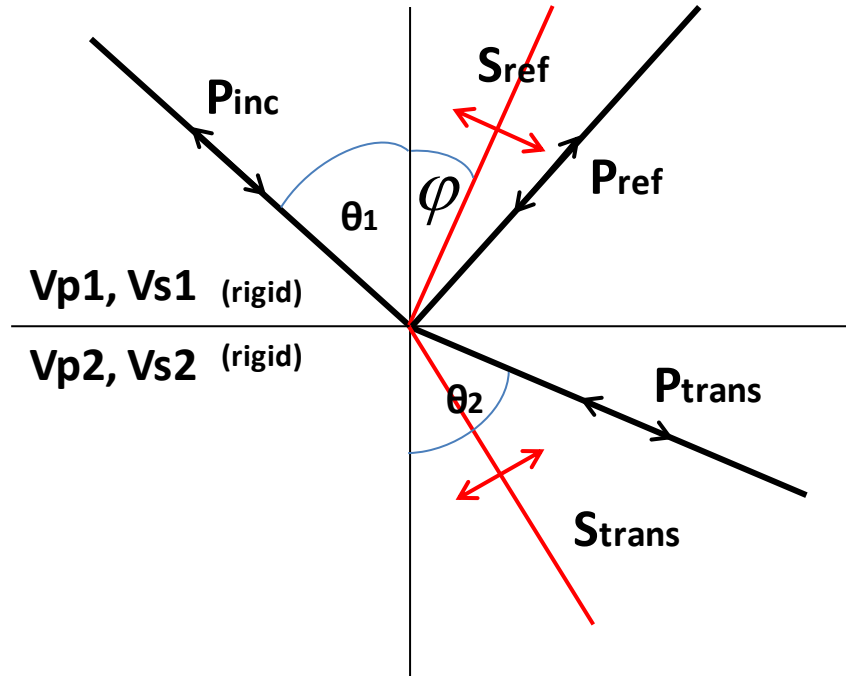
Figure 2.1: Partitioning of energy into different waves types upon reflection and refraction while propagating in a solid and intersecting an interface to a different solid. After Tatham and McCormack, 1998

Figure 2.1 shows an incident P-wave at an angle θ_1 from the vertical, and the reflected or mode-converted S-wave ray at an angle φ. The two angles are related by Shell's Law:

$$\frac{\sin\theta_1}{V_{p1}} = \frac{\sin\theta_2}{V_{p2}} = \frac{\sin\varphi}{V_{s1}} = p, , \tag{2-1}$$

where θ_2 is the P-wave angle of refraction, and p is the ray parameter.

In the case when the initial medium is liquid, there is no reflected/mode-converted S-wave, because liquids do not support S-wave propagation. Therefore, only three modes leave the interface: a reflected P-wave, a transmitted/refracted P-wave, and a transmitted/refracted S-wave. This situation is common in marine acquisition. (Tatham and McCormack, 1998)

Figure 2.2 shows the case for an elastic isotropic medium with a flat reflector. It is possible to observe some characteristics of P-S converted wave reflections that make them different and of particular interest when compared with the traditional P-P wave reflections. The

ray path geometries of the two types of reflections are different: the P-P raypath is symmetric, whereas the P-S raypath is asymmetric since V_s is lower than V_p. See Figure 2.2
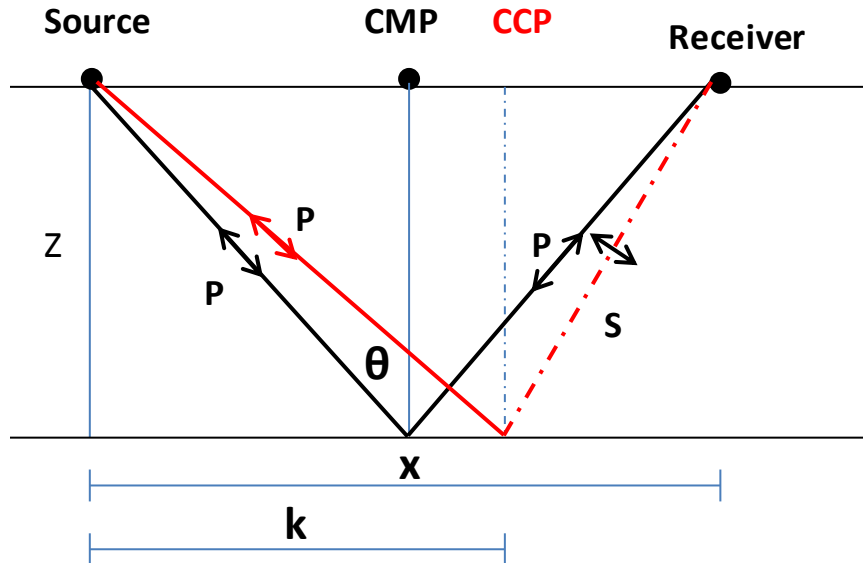
Figure 2.2: A converted wave (P-S) reflection at its common conversion point (CCP) compared to a pure P-wave reflection at its common mid-point (CMP). θ and φ are the P-wave angle of incidence and S-wave angle of reflection, respectively. After Stewart et al., 2002

The reflection point is known as the common conversion point (CCP), since this is where P energy is converted into shear energy. This reflection point is no longer at the common midpoint (CMP) between the source and receiver, but moves closer to the receiver.

Another difference between P- and S-waves is their polarization. The polarization for the P-wave is in the ray path direction while the polarization of S-waves is perpendicular to the ray path. Presuming that the ray pass of retuning waves is almost vertical as the surface due to the low velocity of the overburden, P-waves will move a receiver vertically, while S-waves will move a receiver horizontally only the rays come up vertically. It is therefore necessary to use 3 orthogonal component geophones, with one vertical component and two horizontal components. Figure 2.3a shows a single component geophone which only records the vertical component of

the ground motion, dominated by P-wave energy, and Figure 2.3b shows a three component geophone which records the full tree-dimensional ground motion.

| a) | b) |

Figure 2.3: Geophones using in seismic acquisition, a) single component geophone, and b) three component geophone. Taken from htto://www.crewes.org/ResearchLinks /ConvertedWave/page2.php)

The acquisition of the horizontal component can be done in any two orthogonal spatial directions, but it may be necessary to re-orientate these horizontal components in a horizontal plane to align the radial component with the direction of the seismic line and the trasnsverse component normal to the seismic line.

2.2 P-S wave processing consideration

Although P-S wave exploration has several benefits that make it very appealing to the exploration world, it also offers major challenges at the time of processing. One of them is the asymmetry of the P-S raypath. Converted wave stacking requires a CCP to be computed. The location of a CCP is time variant and depends on the offset and the ratio V_p/V_s. As events get deeper, the CCP location tends asymptotically to a position, called the Asymptotic Common Conversion Point (ACCP).

Consider a single, horizontal, homogeneous layer, with a source-receiver offset that is much smaller than the depth of the conversion point. A first-order approximation for the distance from the source to x_p, the CCP can be computed from the simplified relation:

$$x_P = \frac{2h}{1+\left(\frac{V_S}{V_p}\right)},$$ (2-2)

where h is half the distance from the source to the receiver. This asymptote location may be used to stack the P-S data and is called ACCP binning, which was developed by Fromm et al. (1985). This ACCP algorithm is simple and fast. It is only a first-order approximation of the true conversion point (Tessmer et al., 1988). However, converted wave data can be stacked using the location of the CCP, though it is more expensive.

Figure 2.4 shows some schematic raypaths, converting at various reflector depths. The vertical dotted line (in red) at the midpoint is the location for P-P reflections. The dashed line at the right (in blue) is the asymptotic approximation given by the conversion point at infinite depth.
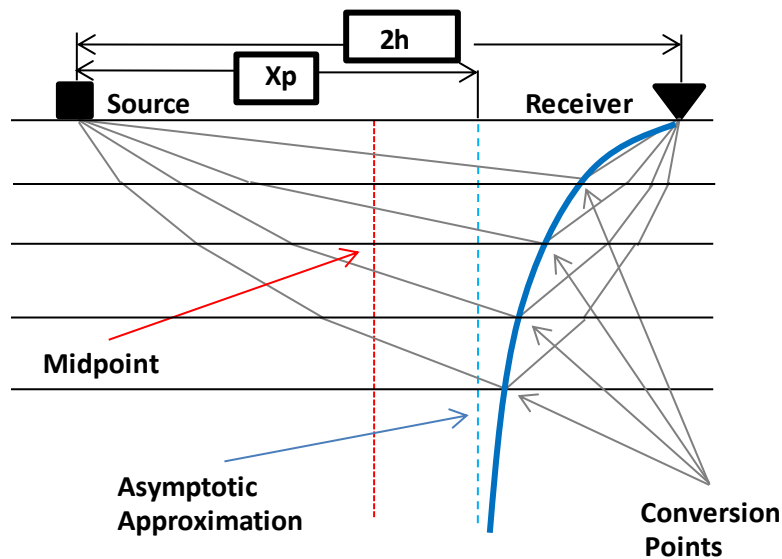
Figure 2.4: Schematic diagram for 2D common conversion point (CCP) binning. After Wang, 1997

Another consideration that should be taken into account during processing is anisotropy, however in this thesis, I assume that earth is isotropic and inhomogeneous, anisotropy is not considered.

There are a number of other problems in processing P-S data. The change of polarity for positive versus negative offset, also known as reverse the polarity of the negative offset traces is a necessary step in seismic processing of converted wave (Brown et al., 2000). In an isotropic medium, the recorded S-wave data may require the rotation to align the energy with the radial and transversal components (Gedco, 2011, Simmons, 1999).

A more accurate moveout correction was developed by Slotboom (1990) who derived a shifted hyperbola equation for P-S data that can correct the offset traveltimes better than a normal hyperbolic velocity analysis.

Another important consideration, and the most problematic for converted wave processing, is the estimation of the S-wave static due to the very low S velocities at the receiver solution. The challenge lies in solving the residual S-wave statics, which is often ten times larger than P-wave statics at the same location due to the very low S velocities (Tatham and McCormack., 1998; Cary et al., 1993).

2.3 Migration

"The purpose of migration is to construct an image of the subsurface from seismic reflection data" (Bancroft, et al., 1998). Prestack migration is a "direct process that moves each input sample into all the possible reflection positions, and invokes the principles of constructive and destructive interference to recreate the actual image". "All traces are searched to find energy that contributes to the output sample" (Bancroft et al., 1994).

2.3.1 Conventional Migration

Bancroft et al. 1994 described several conventional methods of prestack and poststack migration. "Conventional processing has been concentrated on producing a stacked section from CMP gathers, followed by a poststack migration based on the stacking velocities" (Bancroft et al., 1996). "The stacking velocities are used to remove the normal moveout (NMO) that may vary with dip, even when the propagation velocities are constant. The velocities used for migration should have these dip effects removed; therefore some estimation of migration velocity is required" (Bancroft et al., 1994).

Prestack partial migration (Shultz and Sherwood, 1980, Sattlergger et al., 1980) emerged as a remedy to remove the effect of midpoint smearing after stacking sections with dipping events (Yilmaz and Claerbout, 1980).

Prestack migration methods that permit variable velocities include source (shot) record migration (Schultz and Sherwood, 1980; Reshef and Kosloff, 1986; Van der Schoot, 1989; Le and Zhang, 1992; Ng, 1994), prestack constant (or limited) offset migration (Sattlegger, 1980; Deregowki, 1990; Ehinger et al. 1986), migration by altering downward continuation between shot gathers and geophone gathers (Denelle, 1986; Diet et al.,1993) and full prestack Kirchhoff Migration (Lumley 1989, Lumley and Claerbout, 1993). The basic theoretical development of prestack migration dates in the early 1970's by Lindsay and Herman (1970) and Rockwell (1971).

2.3.1.1 Poststack migration

Poststack migration is performed after a stack section has been made. When the velocity is constant, the poststack operator moves the energy from a stacked sample to a semi-circle on

the migrated section. All other stacked sample are mapped in a similar manner to construct the migrated section (Bancroft et al., 1994).

2.3.1.2 Prestack Source (Shot) Record Migration

Prestack data are acquired in shot records, and each record can be migrated separately. In a constant velocity environment, the migration of one trace is represented by a series of prestack migration ellipses with the source and receiver at the foci of the ellipse. The collection of all migrated traces can be stacked directly to complete the migration process (Bancroft et al., 1994).

2.3.1.3 Prestack constant offset migration

Input data can be sorted into section where the source-receiver distance, or offset is constant. A prestack constant offset migration also uses a series of prestack migration ellipse. Prestack shot record migration and prestack constant offset migration should produce identical result when the migrated traces are projected to the zero offset section (Bancroft et al., 1994).

2.3.1.4 Full Prestack Kirchhoff Migration

Full Prestack Kirchhoff migration creates one output migrated trace by summing energy from all input traces within the migration aperture. In this manner, each sample from a given input trace could be moved in time and position to all possible output traces in the migration aperture (Bancroft et al., 1994).

There are many other methods of migration that are available, however the Kirchhoff method will be used in this thesis for converted wave data and will be presented in more detail in the next section.

2.4 Kirchhoff Prestack Migration concepts

Kirchhoff prestack migration is based on a model of the subsurface as an organized set of scatterpoints which scatter energy from any source to all receivers. The model assumes that

energy may come from a source located anywhere on the surface. The energy on a recorded trace is located in time at the total traveltime along the ray path from the source down to the scatterpoint and back up to the receiver (Bancroft, 1994). The objective of prestack migration is to gather all of the scattered energy and relocate it to the position of the scatterpoints. Prestack Kirchhoff migration assumes an output location (or scatterpoint), and then sums the appropriate energy from all available input traces. This procedure is repeated for every output sample.

The surface location of a vertical array of scatterpoints is referred to as the common scatterpoint (CSP). The collection of all input traces that record energy from a given scatterpoint is referred as the migration aperture (Bancroft et al., 1994, 1996). CSP gathers are similar in function to the CMP gathers of conventional processing, however each CSP gathers contains all traces in the migration aperture.

2.4.1 The Cheops pyramid

Most prestack Kirchhoff time migrations assume linear ray paths in a time section from the source to scatterpoint, and from the scatterpoint to the receiver, as illustrated in Figure 2.5. The traveltime t is estimated by adding the time t_s from the source to the scatterpoint, and the time t_r from the scatterpoint to the receiver, or

$$t = t_s + t_r \ .$$
(2-3)

From the geometry, and assuming that the velocity V is constant, the total or two-way, traveltime can be computed from:

$$t = \left[\left(\frac{z_0}{V} \right)^2 + \frac{(x+h)^2}{V^2} \right]^{1/2} + \left[\left(\frac{z_0}{V} \right)^2 + \frac{(x-h)^2}{V^2} \right]^{1/2},$$
(2-4)

where z_o is the depth of the scatterpoint, x is the distance from the midpoint (MP) to the scatterpoint (SP) located at $x=0$, and h is half the source-receiver offset. This equation is referred to as the double square root (DSR) equation (Bancroft et al., 1996).

Extending equation (2-4) to include lateral velocity variation, the DSR equation can be modified to:

$$t = \left[\left(\frac{t_0}{2} \right)^2 + \frac{(x+h)^2}{V_{mig}^2} \right]^{1/2} + \left[\left(\frac{t_0}{2} \right)^2 + \frac{(x-h)^2}{V_{mig}^2} \right]^{1/2}, \tag{2-5}$$

where V_{mig} is the RMS migration velocity approximation of Tanner and Koehle (1969) evaluated at t_0, and is assumed to be locally constant. The time $t_0=t(x=0, h=0)$ is the two-way zero-offset time and is derived from the data. Equation (2-5) defines the traveltime surface over which the Kirchhoff summation or integration takes places. We can define the depth z_o as

$$z_0 = \frac{t_0 V_{ave}}{2}. \tag{2-6}$$
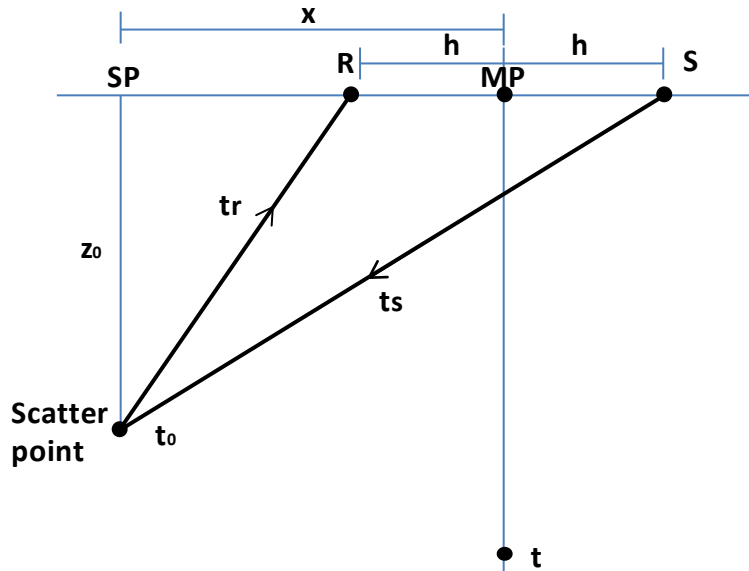
Figure 2.5: Geometry for Kirchhoff prestack time migration with source S and receiver R. The total traveltime is the sum of source to scatterpoint time, t_s, and the scatterpoint to receiver time, t_r. After Bancroft et al., 1998.

The DSR equation may be used to compute the traveltime t for one scatterpoint at t_o into a continuum of 2D x and h locations. This surface is known as Cheops pyramid (Claerbout 1984). "A CMP gather that is located at scatterpoint ($x=0$), intersects Cheops pyramid on a hyperbolic path and allows conventional NMO correction. However, when the intersections of all other CMP gathers ($x \neq 0$) have nonhyperbolic paths, the energy will be mispositioned with hyperbolic NMO correction" (Bancroft et al., 1998).

"The Cheops pyramid is the prestack migration equivalent to the zero offset hyperbola of 2D poststack migration" (Bancroft et al., 1996). Prestack migration refers to the process by which energy distributed over Cheops pyramid is summed or collapsed back to the scatterpoint location at the pyramid's apex (Bancroft et al., 1996) as shown bellow.
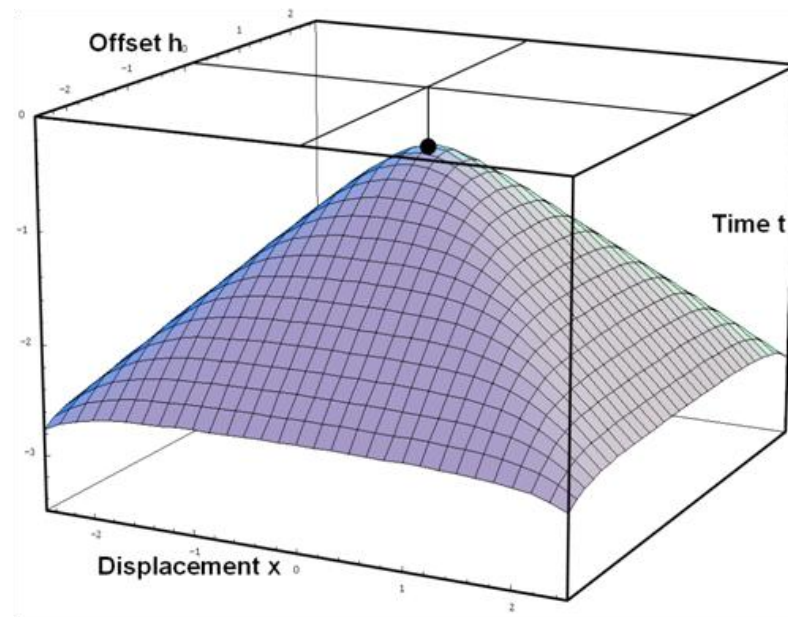
Figure 2.6: Cheops pyramid for continuous range of midpoints and offsets from one scatterpoint is referred to a Cheops pyramid. Taken from Bancroft, 2012

2.5 Equivalent Offset Migration

Equivalent Offset Migration (EOM) is a fast method for performing a Kirchhoff migration and computes an equivalent offset for a trace based on the acquisition geometry relative to a scatterpoint location.

The equivalent offset is defined by converting the DSR equation (2-5) into an equivalent single square root or hyperbolic form (Bancroft et al., 1996). This reformulation achieved by defining a new source and receiver collocated at the equivalent offset position E as illustrated in Figure 2.7. For convenience, the CSP gather is located at $x=0$. The equivalent offset h_e is chosen to maintain the yield traveltime as defined in equation (2-3):

$$t = 2t_e = t_s + t_r. \tag{2-7}$$

This traveltimes can be written as:

$$2\left[\left(\frac{t_0}{2}\right)^2 + \frac{h_e^2}{V_{mig}^2}\right]^{1/2} = \left[\left(\frac{t_0}{2}\right)^2 + \frac{(x+h)^2}{V_{mig}^2}\right]^{1/2} + \left[\left(\frac{t_0}{2}\right)^2 + \frac{(x-h)^2}{V_{mig}^2}\right]^{1/2}. \tag{2-8}$$

This equation may be solved for the equivalent offset h_e to get:

$$h_e^2 = x^2 + h^2 - \left(\frac{2xh}{tV_{mig}}\right)^2. \tag{2-9}$$

A derivation of this equation may be found in Bancroft et al., 1998. The equivalent offset is roughly a quadratic sum of the distance x between the CSP and the CMP, and h, the source-receiver half offset. The parenthesized cross term in equation (2-9) contributes a small time and velocity dependence to the equivalent offset (Bancroft et al., 1996).

2.6 Common scatterpoint gathers

The following description is taken *from Bancroft et al., 1996* with minimal changes. Equation (2-9) shows that scattered energy from a particular scatterpoint, when considered as a function of equivalent offset will be distributed along a hyperbolic path on a CSP gather.

Start of quotation: This new type of prestack migration gather can be formed by ordering all traces according to their equivalent offset from a presumed scatterpoint location. The energy in each input trace will be copied to all CSP gathers without time shifting.
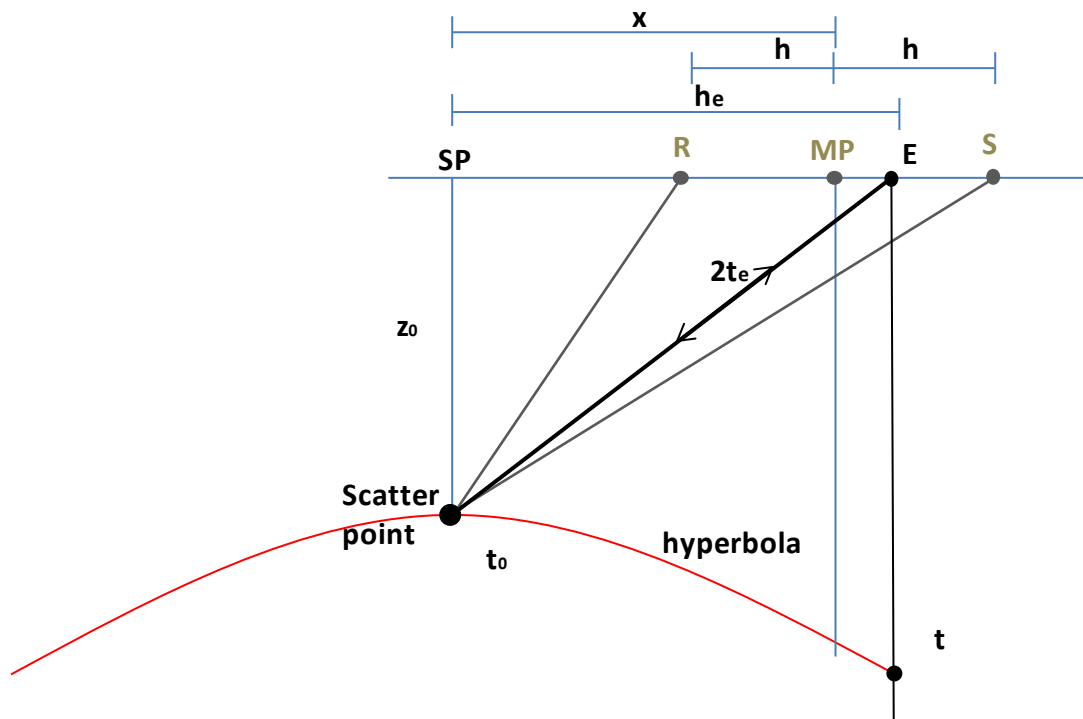
Figure 2.7: The equivalent offset h_e is defined as the offset from the surface to a collocated source-receiver having h_e at same traveltime as the original source-receiver. Scattered energy from all source pairs lies along the hyperbola at their equivalent offset. After Bancroft et al., 1998.

The equivalent offset is quantized into discrete bins, and all energy which falls into a bin is summed. Therefore, an input trace may have its samples spread over a number of offset bins. The first useful energy in the input trace comes from a zero depth scatterpoint at the CSP location $(x=0, t= 0)$ and has an equivalent offset h_{ea} defined by

$$h_{e\alpha} = x. \tag{2-10}$$

The starting time T_α of this useful energy is given by

$$T_\alpha = \frac{2h_{e\alpha}}{V_0}. \tag{2-11}$$

Energy at this point will migrate to the surface of the CSP trace with a dip of 90 degrees. When the input time tends to a large value, the equivalent offset tends to a vertical asymptote $h_{e\omega}$ given by

$$h_{e\omega}^2 = x^2 + h^2. \tag{2-12}$$

It may appear from equation (2-9) that the equivalent offset needs to be computed for each sample in each input trace. However, since the CSP gather is formed by combining traces into equivalent offset bins with a spacing δh, only times at which the input starts in a new offset bin need to be computed. The initial equivalent offset $h_{e\alpha}$ may be computed using equation (2-10) and assigned to an appropriate offset bin. The following samples t_α are added to this bin until the equivalent offset increases to the next bin boundary, at which point the input sample are added to the next bin. The time at which this transition occurs is T_n, where n is the bin index and may be found by rearranging equation (2-9) to yield

$$T_n = \frac{(2xh)}{V_{mig}[x^2 + h^2 - h_{en}^2]^{1/2}}, \tag{2-13}$$

where h_{en} is the equivalent offset of the nth bin boundary. The transition times of each offset bin for a given input trace may be computed to allow efficient copying of the sample into the respective bins *End of quotation from Bancroft et al., 1996.*

The CSP gathers have high fold and offsets that can be greater than the maximum source-receiver offset. This high fold improves the resolution of velocity analysis over conventional CMP gathers. After velocity analysis, NMO and stacking completes the prestack migration.

EOM results will be the same as prestack Kirchhoff time migration, but with shorter run times. The method is easy to implement, and uses standard processing algorithms such as velocity analysis (Bancroft et al., 1995).

Chapter Three: **Converted wave migration using the EO concept**

3.1 Introduction

The prestack migration by equivalent offset and common scatter point is an alternative method to conventional prestack migration. This method is also ideally suited for converted wave processing.

Converted wave processing assumes that the downward propagating energy is a P-wave and the reflected energy is a shear wave. This S-wave is recorded with 3-component receivers (Bancroft et al., 1994, Wang, 1997). The processing methods start with the DSR equation (2-5) or (2-8), with the appropriate P and S velocities for each leg of the ray path, as illustrated in Figure 3.1.

From equation (2-5) and using the concepts of prestack time migration and RMS velocities for both, the P-wave and S-wave energy, the traveltime is defined by:

$$t = \left[\left(\frac{t_{0p}}{2}\right)^2 + \frac{h_s{}^2}{V_{p-rms}^2}\right]^{1/2} + \left[\left(\frac{t_{0s}}{2}\right)^2 + \frac{h_r{}^2}{V_{s-rms}^2}\right]^{1/2}, \qquad (3\text{-}1)$$

where $V_{p\text{-}rms}$ and $V_{s\text{-}rms}$ are the respective RMS velocities for P and S waves. The vertical zero-offset traveltime of the source raypath is t_{0p}, and the vertical zero-offset traveltime of the receiver raypath is t_{0s}. The distances h_s and h_r are shown in Figure 3.1. The depth of the conversion point is z_0 and corresponds to t_{0p} and t_{0s}, i. e.,

$$z_0 = \frac{t_{0p} \; V_{p-ave}}{2} = \frac{t_{0s} \; V_{s-ave}}{2}. \qquad (3\text{-}2)$$

Replacing t_0 by z_0, yields:
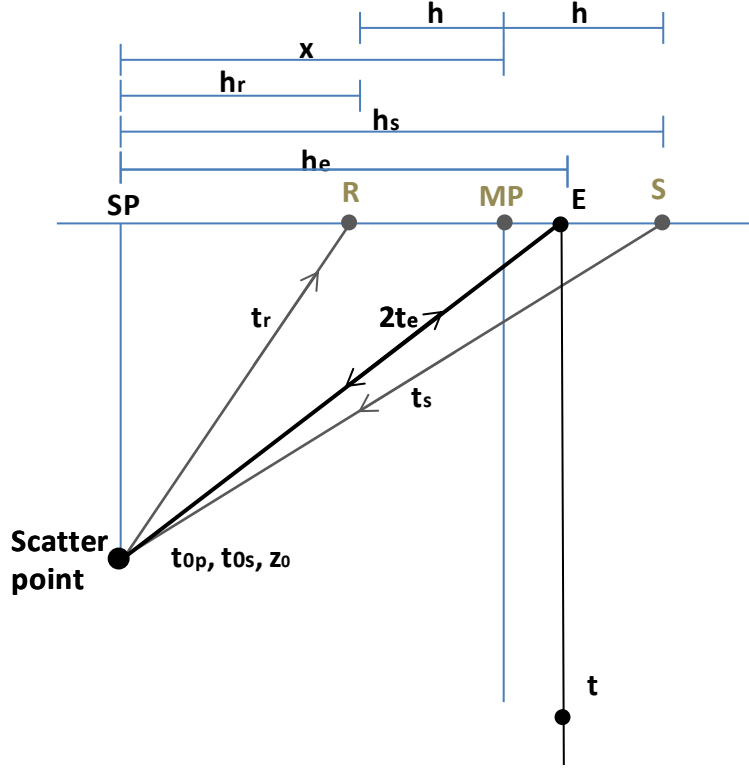
Figure 3.1: The raypaths and traveltime for a scatter or conversion point.

$$t = \left[\left(\frac{z_0}{V_{p-ave}}\right)^2 + \frac{h_s{}^2}{V_{p-rms}^2}\right]^{1/2} + \left[\left(\frac{z_0}{V_{s-ave}}\right)^2 + \frac{h_r{}^2}{V_{s-rms}^2}\right]^{1/2}, \qquad (3\text{-}3)$$

or

$$t = \frac{1}{V_{p-rms}}\left[\left(\frac{z_0\, V_{p-rms}}{V_{p-ave}}\right)^2 + h_s{}^2\right]^{1/2} + \frac{1}{V_{s-rms}}\left[\left(\frac{z_0\, V_{s-rms}}{V_{s-ave}}\right)^2 + h_r{}^2\right]^{1/2}. \qquad (3\text{-}4)$$

The same traveltime t for the equivalent offset h_e is given by:

$$t = \frac{1}{V_{p-rms}}\left[\left(\frac{z_0\, V_{p-rms}}{V_{p-ave}}\right)^2 + h_e{}^2\right]^{1/2} + \frac{1}{V_{s-rms}}\left[\left(\frac{z_0\, V_{s-rms}}{V_{s-ave}}\right)^2 + h_e{}^2\right]^{1/2}. \qquad (3\text{-}5)$$

If we assume the ratio of the RMS and average velocities, V_{rms} and V_{ave} for the P and S wave velocities to be constant, the constant k may be defined as

$$k \approx \frac{V_{rms}}{V_{ave}} \approx \frac{V_{p-rms}}{V_{p-ave}} \approx \frac{V_{s-rms}}{V_{s-ave}}, \qquad (3\text{-}6)$$

This allows for the definition of a pseudo depth

$$\hat{z}_0 = z_0 \frac{V_{rms}}{V_{ave}}, \tag{3-7}$$

for each square root equation (3-5) can be written as

$$t = \frac{1}{V_{p-rms}}\sqrt{\hat{z}_0^2 + h_e^2} + \frac{1}{V_{s-rms}}\sqrt{\hat{z}_0^2 + h_e^2} \, . \tag{3-8}$$

The square-root portions are equal, giving the hyperbolic traveltime equation

$$t = \left(\frac{1}{V_{p-rms}} + \frac{1}{V_{s-rms}}\right)\sqrt{\hat{z}_0^2 + h_e^2} \, . \tag{3-9}$$

This equation can also be written as

$$t = \frac{2}{V_c} \, (\hat{z}_0^2 + h_e^2)^{1/2}, \tag{3-10}$$

where V_c is defined as

$$V_c = \frac{2V_{p-rms}V_{s-rms}}{V_{p-rms} + V_{s-rms}} = \frac{2V_{p-rms}}{(1+\gamma)} = \frac{2\,\gamma V_{s-rms}}{(1+\gamma)} \, . \tag{3-11}$$

The ratio of the P and S RMS velocities $\hat{\gamma}_{rms}$ is defined by

$$\hat{\gamma}_{rms} = \frac{V_{p-rms}}{V_{s-rms}}. \tag{3-12}$$

The equivalent offset h_e for converted waves can be written as:

$$h_e^2 = \frac{t^2 V_c^2}{4} - \hat{z}_0^2. \tag{3-13}$$

From equation (3-13), the converted wave data in the prestack migration gathers will have wave reflection energy with hyperbolic moveout defined with the velocity V_c.

At this point, V_c can be only be used after the gathers are formed. However, initial estimates of V_c can be formed and used to estimate V_s, which is then used to form the common conversion scatterpoint (CCSP) gathers.

After P-S data are transformed into CCSP gathers by equivalent offsets, the asymmetry of the P-S ray paths is removed and conventional velocity analysis will provide a more accurate estimate of V_c.

We obtain V_c from equating the zero offset traveltimes with the original offset traveltimes, i.e.

$$t = \frac{1}{V_p} \sqrt{\hat{z}_0^2 + h_s^2} + \frac{1}{V_s} \sqrt{\hat{z}_0^2 + h_r^2} = \left(\frac{1}{V_p} + \frac{1}{V_s}\right) \sqrt{\hat{z}_0^2 + h_e^2} = \frac{2}{V_c} \sqrt{\hat{z}_0^2 + h_e^2}, \quad (3\text{-}14)$$

where, h_e can also be redefined as

$$h_e^2 = \frac{V_c^2}{4} \left(\frac{1}{V_p} \sqrt{\hat{z}_0^2 + h_s^2} + \frac{1}{V_s} \sqrt{\hat{z}_0^2 + h_r^2}\right)^2 - \hat{z}_0^2. \quad (3\text{-}15)$$

From the equation (3-15), h_e varies with the trace geometry h_s, and h_r, but also varies with depth $\hat{z}_0$ and the velocity $V_c(z_o)$, as V_p can also be a function of depth $\hat{z}_0$.

3.2 Mapping input data to a CSP gather using the equivalent offset

We now ask the limits of h_e as depth tends towards either zero or infinity. The first usable time sample may be found when z_0 approaches zero.

Substituting (3-11) in (3-15) h_e can be defined as:

$$h_{e\alpha} = \frac{(h_s + \gamma h_r)}{1 + \gamma}. \quad (3\text{-}16)$$

Details are shown in Appendix A.

When z_o goes to infinity, the equivalent offset tends to an asymptote $h_{e\omega}$ which may be defined as

$$h_{e\omega}^2 = \frac{(h_s^2 + \gamma h_r^2)}{1 + \gamma}. \quad (3\text{-}17)$$

Details and definitions are shown in Appendix B.

27

The first sample and asymptotic function similar to conventional P-P equivalent offset asymptotes and define the range of offsets for the samples in the input trace.

Figure 3.2 shows a CSP gather with one trace using the values V_p=4000 m/s, V_s=2000 m/s, the distance between the CSP and CMP as x=100 m, and a source-receiver half offset of h= 50 m. The equivalent offset h_e has a range between 83.33 m (h_{ea}) and 95.74 m ($h_{e\omega}$).
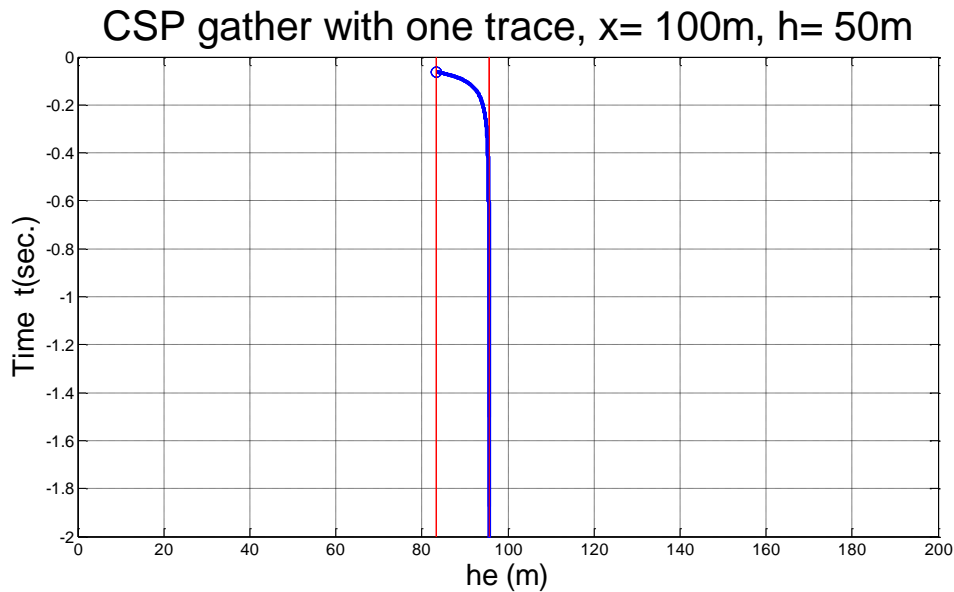
Figure 3.2: Equivalent offset for constant velocity *Vp*=4000 m/s, *Vs*=2000 m/s, *x*=100 m, *h*=50 m

Figure 3.3 shows h_e curves for the same input trace at different CSP surface locations. Using same the values for V_p and V_s, the distance between the CMP and the CSP range from 200 $< x <$ 2000 m with increments of 200 m, and a source-receiver half offset of h= 200 m. Note how the equivalent offset tends to the asymptotic values as t increases. Note also, how h_e starts at different t_a as x increases.

28
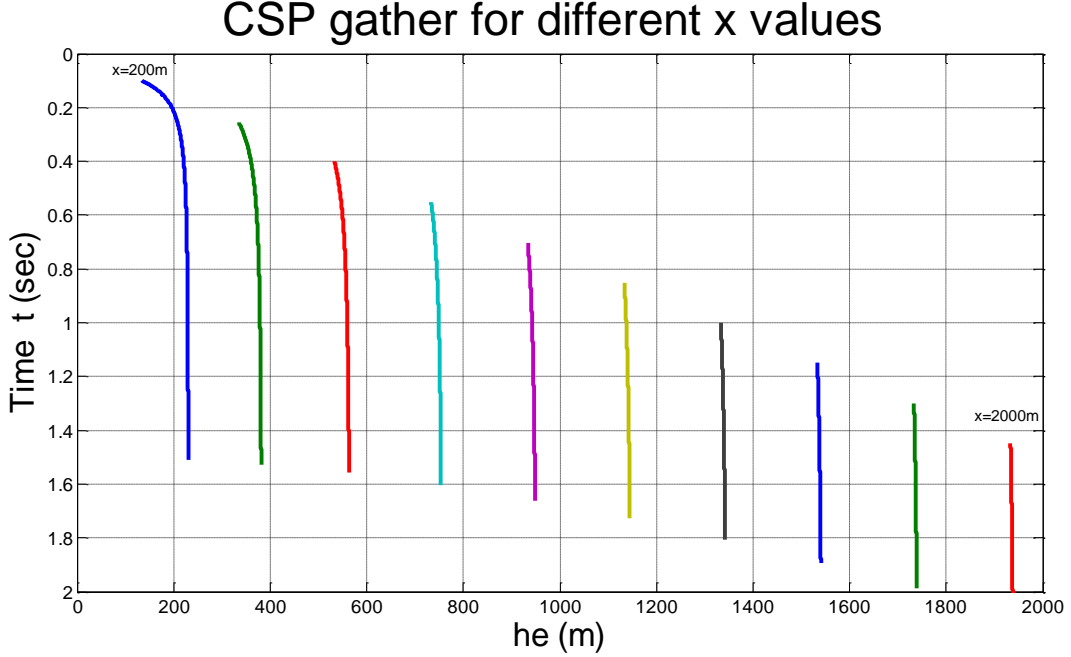
Figure 3.3: Equivalent offsets for one input trace with _Vp_=4000 m/s, _Vs_=2000 m/s, _x_=from 200 to 2000m, and _h_=200m.

3.3 Extending the use of the converted wave velocity V_c.

The velocity V_c is used to apply moveout correction on the converted wave CSP gathers. This raises the question whether it is possible to ignore V_p and V_s and simply use V_c as a velocity for a limited range of input data. We now want to know how much input data can be used with this assumption. Then, we can estimate V_s using V_p and V_c in equation (3-11).

We know from the equation (3-4) that

$$t_{p-s} = \frac{1}{V_p} \sqrt{z_0^2 + h_s^2} + \frac{1}{V_s} \sqrt{z_0^2 + h_r^2}, \qquad (3\text{-}18)$$

and now we define a time t_{Vc} assuming a single velocity of the medium, V_c, we replace V_p and V_s with V_c, i.e.,

$$t_{Vc} = \frac{1}{V_c} \sqrt{z_0^2 + h_s^2} + \frac{1}{V_c} \sqrt{z_0^2 + h_r^2}. \qquad (3\text{-}19)$$

How close is t_{Vc} to t_{p-s}? Given $h_s = x + h$ and $h_r = x - h$ (as shown in Figures 3.1), and if we assume either $x=0$ or $h=0$, then $t_{h \, or \, x=0} = t_{Vc}$. For all other conditions,

29

$$t_{h \ or \ x \neq 0} \neq t_{Vc}. \qquad\qquad (3\text{-}20)$$

However, there is a short range of usable data when the CMP displacement, x, is small. Using this small range of x, we can get an initial estimate of V_c from the data that will lead to a simple estimate of the shear velocity V_s.

The time difference between equations (3-18) and (3-19) can give us a difference in sign that is dependent on the polarity of x, and will tend to remove any bias in the sum when x becomes larger, allowing a greater range for gathering.

The difference between t_{Vc} and $t_{p\text{-}s}$ is defined as δt and is given by

$$\delta t = t_{Vc} - t_{p-s} \qquad\qquad (3\text{-}21)$$

Figure 3.4 was created to illustrate the error δt that can be expected for offset ranges h, and depth z, using the values V_p=4000 m/s, V_s=2000 m/s, a distance between the CSP and the CMP of x= 100 m, and a source-receiver half offset h from 0 to 200 m. This figure also illustrates the error as a function of depth.

In this figure, we can tolerate a small error in t_{Vc}, for example 5 ms or 10 ms that will allow us to collect near offset traces into a gather for velocity analysis. If so, we may get enough traces into a limited converted wave CSP (LCCSP) gather to quickly and accurately estimate V_c.

We now assume a vertical array of scatterpoints at depth z from 0 to 1000 m, that are at a spatial location of $x = 0$. A range of mid-point locations are located to the left and right of this vertical array, of a distance x, i.e. $x = $ -1000 to 1000 m. We assume a fixed value for a half-offset, h. Two-way traveltimes (equation 3.18) are then computed to and from the scatterpoint as a function of x and z, i.e. $t(x,z,h)$. This is repeated for t_{Vc} (equation 3.19), and the plots are shown in Figure 3.5, where h was chosen to be 50 m.
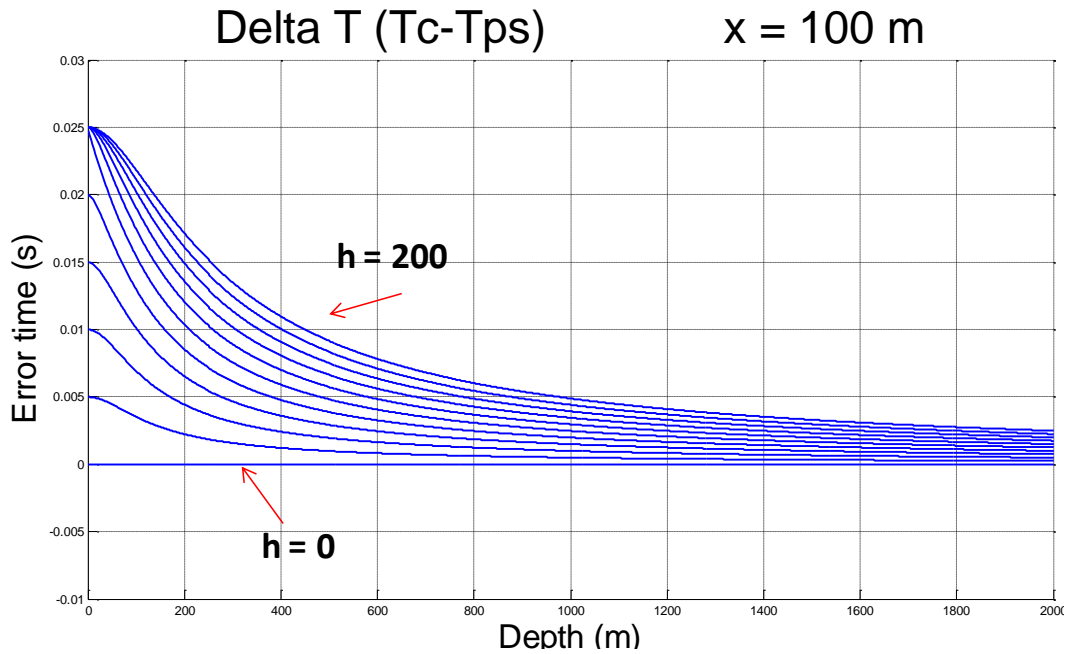
Figure 3.4: Error time for different source-receiver half offsets *h* (from 0 to 200 m), in increments of 20 m, for constant velocities. *Vp*=4000 m/s, *Vs*=2000 m/s, distance between the CSP and CMP *x*=100 m.

With a half-offset of 50 m, the difference in the two traveltimes is difficult to view. The

following plot (Figure 3.6) shows traveltimes, and the magnitude of the difference in traveltimes.
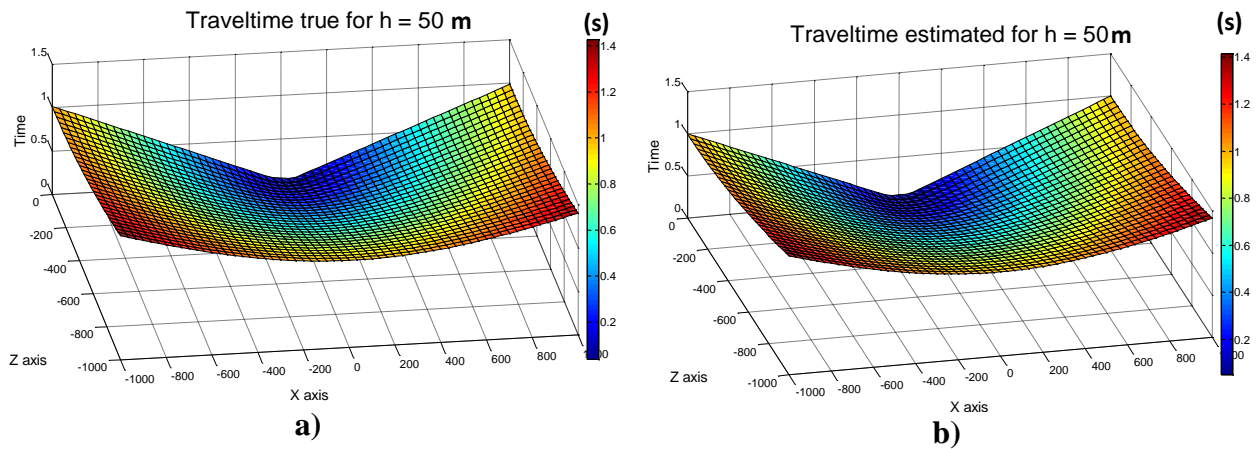
Figure 3.5: Traveltime for one vertical array of scatterpoints at x = 0, with a) the true traveltimes (*$t_{p\text{-}s}$*) and b) the traveltimes computed assuming a constant converted wave velocity (*t_{Vc}*) for h = 50m.
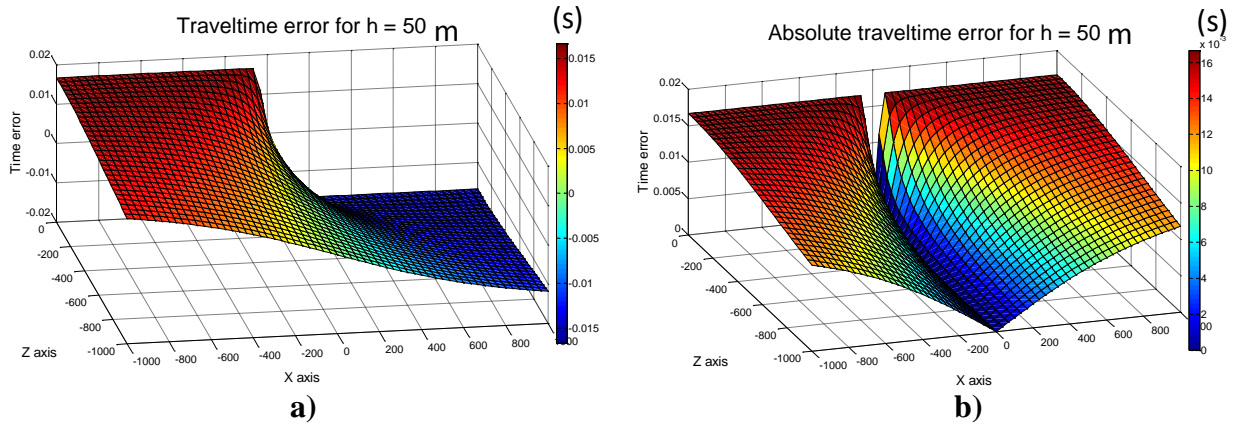
Figure 3.6: Traveltime differences with a) the actual traveltime and b) the magnitude of the calculated traveltime.

Figure 3.6a shows the traveltime error to range from -15 ms to approximately +15 ms. If we limit the absolute traveltime difference in Figure 3.6b to a maximum of 10 ms, then the data in traces that have geometry in a blue hue could be used. Figure 3.6a illustrates that there is an opposite polarity of the time error. Stacking traces with an opposing time differences will lower the frequency content of these traces, but will not introduce a time shift bias in the data. Consequently, a larger time difference, say 20 ms, may be usable.

The absolute traveltime is plotted below in a plan view with the colour defining the absolute time difference, in Figure 3.7. The coordinates of this plot are in space and depth (x, z), representing the location of the midpoint and the depth of the scatterpoint for a fixed source-receiver offset *h*. These coordinates are not convenient for evaluating a LCCSP gather. We remap the data first to two-way time in Figure 3.8, and then to equivalent offset in Figure 3.9. This figure now represents the location of energy on a CSP gather, and shows where the limited offset data will lie. Note, the reflected energy of the converted wave is zero when the offset is zero.
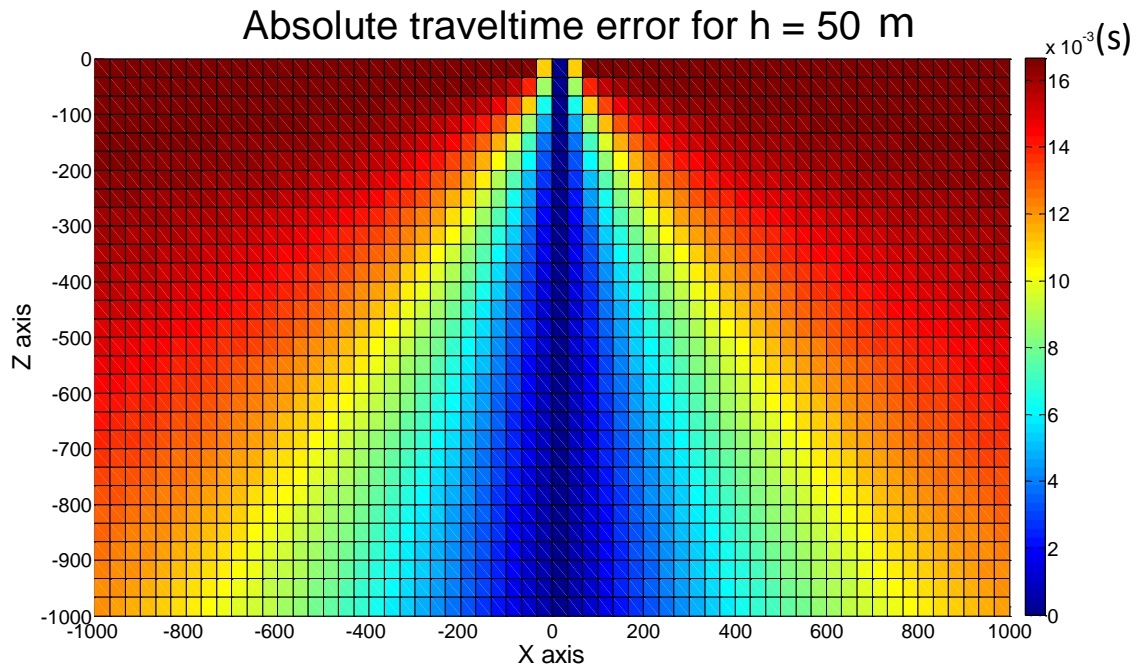
Figure 3.7: Plan (or map view) of the absolute value of the traveltime difference.
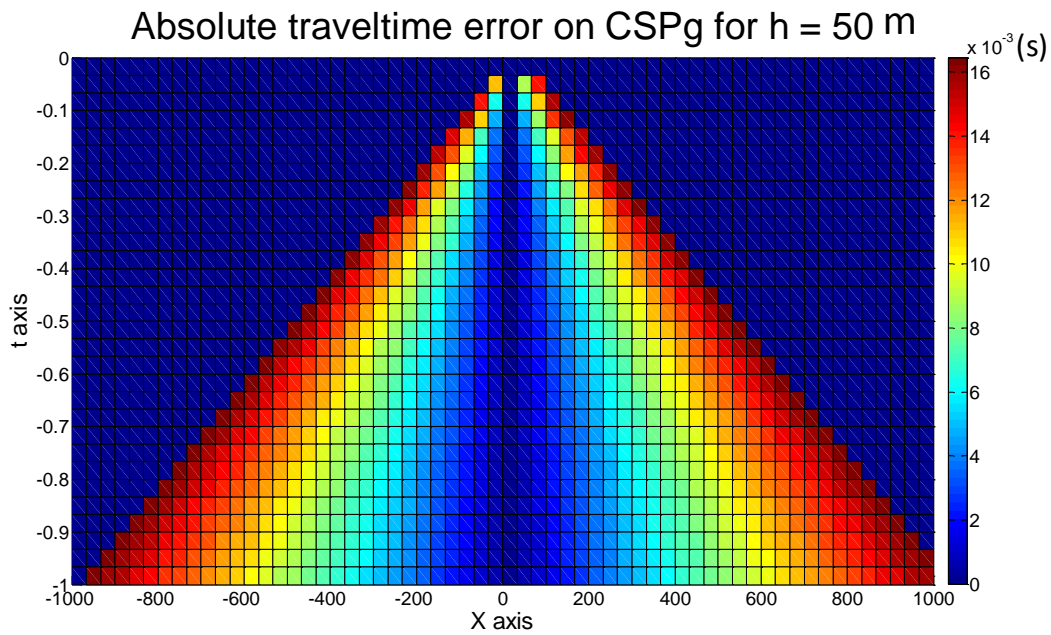
Figure 3.8: Traveltime error plotted as two-way time and depth.
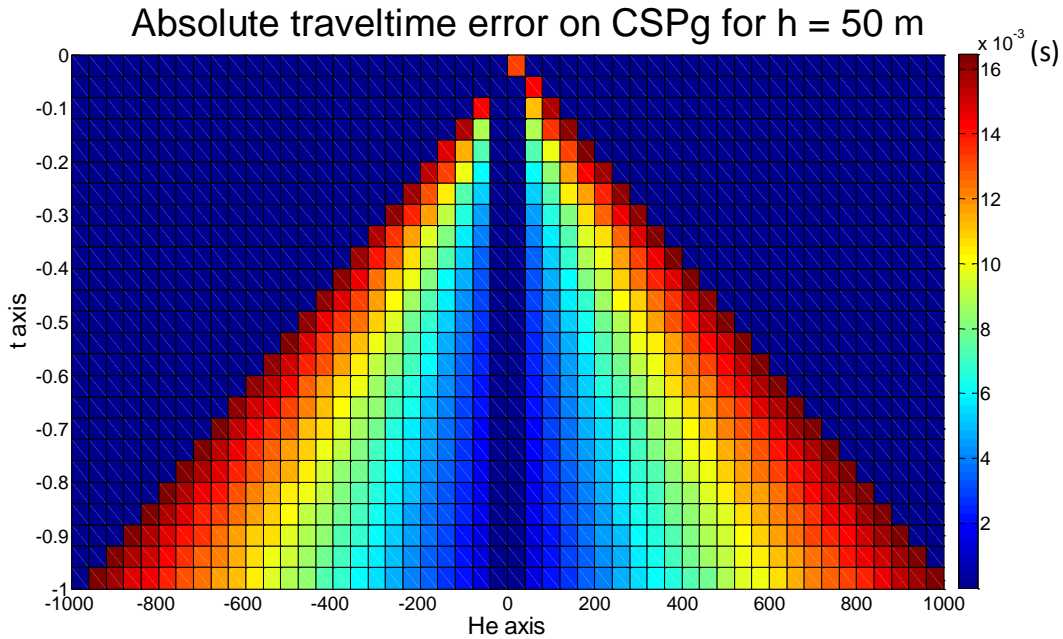
Figure 3.9: Traveltime error plotted as two-way time and equivalent offset.

The following Figure 3.10 shows the traveltime errors for CSP gathers with offsets of h = 50, 100, 200, and 500. The source is on the left and the receiver is on the right. The converted wave ray-paths are asymmetrical and produces an image that is asymmetrical about $x = 0$. Swapping the source-receiver locations will reverse the equivalent offsets. A center spread acquisition system will produce LCCSP gathers with opposite polarities of the traveltime difference that will tend to sum to zero and remove any bias in the gather.

A limiting value for the time difference could be equal to half the size of the positive part of the wavelet peak. Equal half shifts in opposite directions may tend to cancel the wavelets.

3.4 Velocity consideration

One of the major problems of converted wave processing is the scale of the axis that defines the velocities. This scale may be in time or depth, and the time scale could be in P-wave times, S-wave times, or C-wave times.

34

There are numerous properties that use the term velocity which are related to the actual velocity of the medium. These are referred to as velocity types, with the main four "velocities" referred to as: interval, average, root-mean-squared, and stacking velocities.
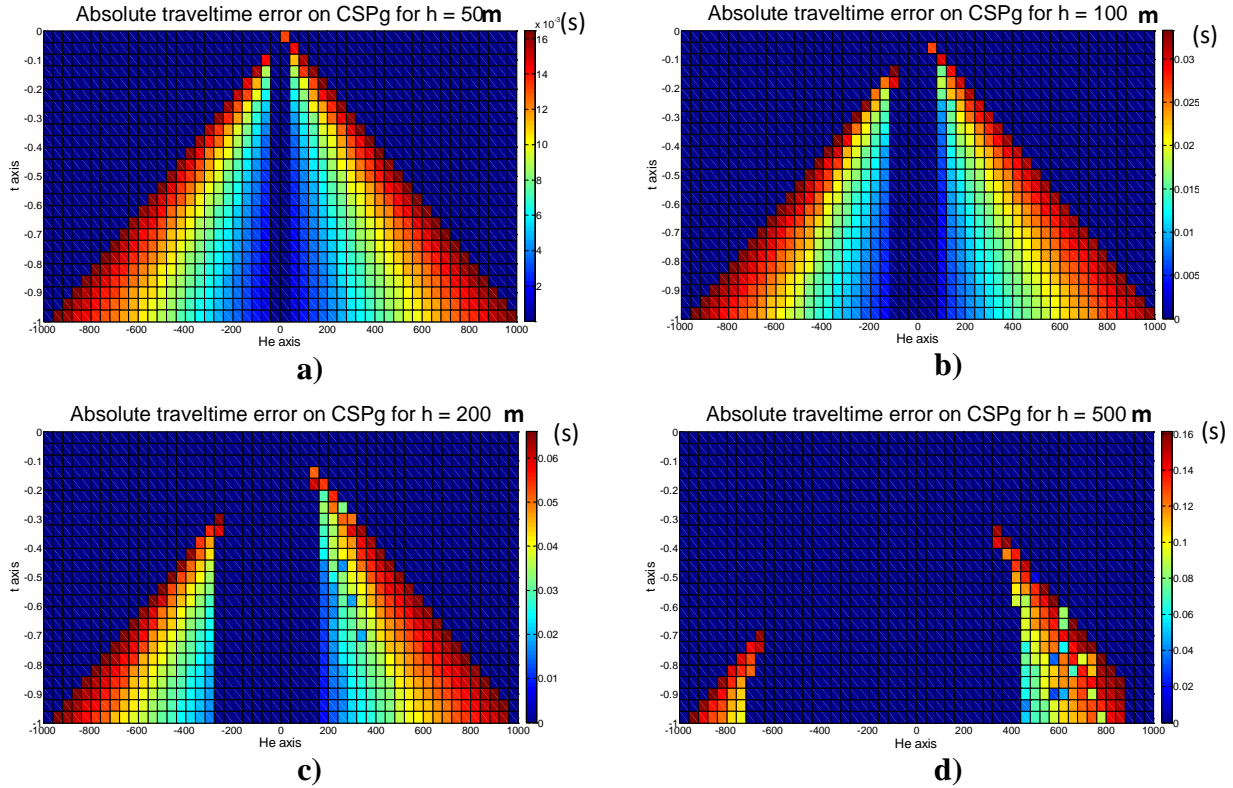
Figure 3.10: Traveltime difference on a CSP gather for various half offsets h equal to: a) 50 m, b) 100 m, c) 200 m, and d) 500 m. Note that the values on the colour bar vary for each figure.

The average velocity is the ratio of the distance along a certain path to the time to traverse this path. Vertical two-way traveltimes t_0 are related to vertical depths z_0 with the average velocity V_{ave}

$$V_{ave}(t_0, or\ z_0) = \frac{2}{t_0}z_0, \tag{3-22}$$

where the average velocity may be defined in time or space, depending on the direction of the conversion. It is defined from the instantaneous velocity $V_{Int}(n)$ and interval time t_n defined in the nth layer by

35

$$V_{ave}(t_{0-n}) = \frac{\sum_{i=1}^{n} V_{Int}(n)\, t_n}{\sum_{i=1}^{n} t_n},$$ (3-24)

When using the root-mean square (RMS) velocity V_{rms}, the scale is in vertical time. These velocities are also computed from the interval velocities using:

$$V_{rms}(t_{0-n}) = \sqrt{\frac{\sum_{i=1}^{n} V_{Int}^2 t_n}{\sum_{i=1}^{n} t_n}}.$$ (3-25)

Equations (3-24) and (3-25) can be modified to compute the interval velocity from average or RMS velocities, allowing one type of velocity to be converted into another. With one mode, velocities can be expressed in time or, if necessary, in depth.

3.5 Introducing an new value for γ based on RMS velocities

The ratio between P-wave and S-wave velocities as been defined in equation (3-12) but should be written as a function of depth using interval velocities

$$\gamma(z) = \frac{V_{p-Int}}{V_{s-Int}}.$$ (3-26)

We can have RMS velocities for P-wave, S-wave and also for C-wave, and hence could write a relationship γ between the corresponding RMS velocities. However, the times of the corresponding velocities are different, i. e.,

$$\hat{\gamma}_{rms}(z\ or\ ?) = \frac{V_{p-rms}(t_p)}{V_{s-rms}(t_s)},$$ (3-27)

Where the times t_p and t_s are at the same depth.

Ideally we should continue to use depth as the common parameters to compare different modes of propagation; however it is convenient to use one common time scale. Here, we are going to use P-wave time t_p, as the P-wave velocities are usually defined first, and are more reliable. Then, scale the S and P-data to align events on the same display.

This requires converting the S-wave velocity from t_s time to t_p time, i, e.,

$$\hat{\gamma}_{rms}\left(t_p\right) = \frac{V_{p-rms}\left(t_p\right)}{V_{s-rms}\left(t_p\right)}. \tag{3-28}$$

The following section will consider practical methods for estimated V_c by using a small range of x and allows h to range from zero to maximum values of h_{max} according to the geometry shown in Figure 3.1.

3.6 Estimating an initial value for V_c.

One method of computing an initial velocity for V_c is to scale V_p with an assumed value for $\hat{\gamma}$. This requires adjusting of the velocity V_p, and shifting the time t_{0p} to a larger time of t_{0c}, i.e.,

$$V_{c-rms}(t_{0s}) = \frac{2}{(1+\hat{\gamma})} V_{p-rms}\left(t_{0p}\right), \tag{3-29}$$

where

$$t_{0s} = \frac{1+\gamma}{2} t_{0p}. \tag{3-30}$$

Tests could be run with different values of $\hat{\gamma}$ to establish more accurate values of V_c that vary with time t_0.

Another method for estimating V_c is to use the equivalent offset method with short offsets. Consider again equation (3.1), but now expressed in the midpoint location x and half offset h

$$t_c = \frac{1}{V_{p-rms}} \sqrt{\frac{t_{0p}^2}{4} + \left(\frac{x+h}{V_{p-rms}(t_{0p})}\right)^2} + \frac{1}{V_{s-rms}} \sqrt{\frac{t_{0s}^2}{4} + \left(\frac{x-h}{V_{s-rms}(t_{0s})}\right)^2}. \tag{3-31}$$

Using a pseudo depth, we have

$$t_c(\hat{z}_0^2) = \frac{1}{V_{p-rms}(\hat{z}_0^2)} \sqrt{\hat{z}_0^2 + (x+h)^2} + \frac{1}{V_{s-rms}(\hat{z}_0^2)} \sqrt{\hat{z}_0^2 + (x-h)^2} . \quad (3\text{-}32)$$

When x is small relative to h, we can assume

$$|x + h| \approx |x - h| \approx |h|, \qquad (3\text{-}33)$$

And we combine the two square-roots, and convert the S velocity to a P velocity giving

$$t_{c, x \ll h} = \frac{1 + \gamma_{rms}}{V_{p-rms}(\hat{z}o)} \sqrt{\hat{z}_0^2 + h^2} , \qquad (3\text{-}34)$$

where $\hat{\gamma}_{rms}$ is the ratio

$$\hat{\gamma}_{rms}(\hat{z}) = \frac{V_{p-rms}(\hat{z}0)}{V_{s-rms}(\hat{z}0)}. \qquad (3\text{-}35)$$

Equation (3-34) can be written in terms of a RMS converted wave velocity

$$t_{c, x \ll h} \approx \frac{2}{V_c(\hat{z}o)} \sqrt{\hat{z}_0^2 + h^2} , \qquad (3\text{-}36)$$

giving a converted wave velocity $V_{c\text{-}rms}(\hat{z}_0)$, as

$$V_{c-rms}(\hat{z}_0) = \frac{2}{(1 + \hat{\gamma}_{rms})} V_{p-rms}(\hat{z}_0) . \qquad (3\text{-}37)$$

The equation (3-37) tells us that we can approximate an initial equivalent offset h_e with an estimate of $V_{c\text{-}rms}$ to form gathers with short displacements x.

There will be no energy at zero offset, but if a gather can be formed with a short displacement x, then a simple velocity analysis will provide a more accurate converted wave velocity V_c . This velocity may also be used for moveout correction but more importantly can be used for an initial estimation of V_s, which can then be used to form complete CSP gathers. This is similar to conventional data processing where a supergather CMP is formed by stacking neighbouring CMP gathers. The difference however is that the actual equivalent offset h_e is used when forming the CSP gathers. We may also try an approximation $\hat{h}_e^2$ to the equivalent offset.

$$\hat{h}_e^2 = x^2 + h^2. \tag{3-38}$$

If x is very small, equation (3-38) reduces to a super CMP gather to find the velocities. If the displacement x is too small, there may not be enough energy as the amplitude of a converted wave is zero when $x = 0$.

3.7 Extending to all offsets

Given the P-wave velocity and a good estimate of the S-wave velocity, the source and receiver traveltimes can be computed for an EOM that encompasses all offsets. Equation (3-32) may be used to compute a converted wave traveltime and is repeated with the actual times of the velocity,

$$t_c(t_{0p}, x, h) = \frac{1}{V_{p-rms}(t_{0p})} \sqrt{\hat{z}_0^2 + (x+h)^2} + \frac{1}{V_{s-rms}(t_{0s})} \sqrt{\hat{z}_0^2 + (x-h)^2}, \tag{3-39}$$

that is equated to an equivalent offset for a collocated source and receiver,

$$t_c(t_{0p}, h_e) = \frac{1}{V_{p-rms}(t_{0p})} \sqrt{\hat{z}_0^2 + h_e^2} + \frac{1}{V_{s-rms}(t_{0s})} \sqrt{\hat{z}_0^2 + h_e^2}, \tag{3-40}$$

or

$$t_c(t_{0p}, h_e) = \left[\frac{1}{V_{p-rms}(t_{0p})} + \frac{1}{V_{s-rms}(t_{0s})} \right] \sqrt{\hat{z}_0^2 + h_e^2}, \tag{3-41}$$

or

$$t_c(t_{0p}, h_e) = \frac{2}{V_{c-rms}(T_{0p})} \sqrt{\hat{z}_0^2 + h_e}. \tag{3-42}$$

This equation tells us that we can compute a converted traveltime using equation (3-39), and assign it an equivalent offset h_e using equation (3-42). A prestack migration gather can be formed using $V_{p\text{-}rms}$ and $V_{s\text{-}rms}$, and then been processed like conventional data using $V_{c\text{-}rms}$. This process is referred to as converted wave equivalent offset migration (C-EOM).

Note however, that the times of the velocities in equation (3-39) are different and need to be aligned. This is discussed in the following section where I match the traveltime for P, S and C wave data.

3.8 Matching the traveltime for P-, and C-wave data.

The objective is to map the traveltimes between various velocities for the different modes. In the case where we want to map P velocities to match an initial guess of V_c, we start with $V_{p\text{-}rms}$ (t$_{0p}$). Then, scale the amplitude and times to an estimated converted wave velocity $V_{c\text{-}rms}$ (t$_{0c}$) to t_{op} times $V_{c\text{-}rms}$ (t$_{0p}$). I shall use real data in the following sections to illustrate the progress of the methods. The input velocities that were picked from the real data were smoothed for easier viewing.

Please note that some migration methods use interval velocities, but a Kirchhoff migration requires the velocities to be in an RMS form. The velocities may be converted from one form to another. The γ function is usually defined for layers in depth with defined interval velocities. A corresponding γ can be defined for RMS velocities.

3.8.1 Method 1

This method starts with the RMS P velocities, $(V_{p\text{-}rms})$ and converts then to interval P velocity $(V_{p\text{-}Int})$, then $(V_{c\text{-}Int})$ then to the RMS C velocities $(V_{c\text{-}rms})$.

1. Convert $V_{p\text{-}rms}(t_{0\text{-}p})$ to interval velocities $V_{p\text{-}Int}(t_{0\text{-}p})$

$$V_{p-Int}(n) = \sqrt{\frac{t_n V_{p-rms}^2(n) - t_{n-1} V_{p-rms}^2(n-1)}{t_n - t_{n-1}}}. \tag{3-43}$$

RMS, interval, and average P velocities $(V_{p\text{-}rms}(t_{0\text{-}p}), V_{p\text{-}Int}(t_{0\text{-}p})$ and $V_{p\text{-}ave}(t_{0\text{-}p})$ are illustrated in Figure 3.11a.

2. Use the interval velocities to map the times to depth $t_{0\text{-}p} \Rightarrow z_0$.

$$z_n = \frac{1}{2} V_{p-Int}(n) * (t_n - t_{n-1}). \tag{3-44}$$

3. Scale the amplitude of V_{c-Int} to V_{p-Int} at z (same as t_{0-p}) using γ, (as illustrated in Figure 3.11b where $V_{p-Int}(z)$ is in blue and $V_{c-Int}(Gz)$ is in green),

$$V_{c-Int}(z, or\ t_{0p}) = \frac{2}{(1+\gamma)} V_{p-Int}(z, or\ t_{0p}). \tag{3-45}$$

4. Use $V_{c-Int}(z)$ and the corresponding depth increments, compute the C times at each depth.

$$V_{c-Int}(t_{0c\ at\ z_n}) = V_{c-Int}(z_n). \tag{3-46}$$

5. Resample V_{c-Int} from irregular times (at depth) to equal time increments

$$V_{c-Int}(t_{0p\ at\ z_n}) \Rightarrow V_{c-Int}(n\delta t). \tag{3-47}$$

6. Convert the interval C velocity (V_{c-Int}) to RMS C velocities (V_{c-rms}),

$$V_{c-rms}(n) = \sqrt{\frac{\sum_{i=1}^{n} t_i\ V_{c-Int}^2(i)}{\sum_{i=1}^{n} t_i}}, \tag{3-48}$$

as illustrated in Figure 3.11c as V_{c-rms1}.

3.8.2 Method 2

This method uses a single approximation, is much simpler than method 1, but has a similar accuracy. Using the corresponding average velocity we get the depth z_0 from

$$2\ z_0 = t_{0c}\ V_{c-ave}(z) = t_{0p}\ V_{p-ave}(z), \tag{3-49}$$

and assuming the ratio of average P and C velocities to be similar to the ratio of P and C RMS velocities

$$t_{0c} = t_{0p} \frac{V_{p-ave}(z)}{V_{c-ave}(z)} \approx t_{0p} \frac{V_{p-rms}(z)}{V_{c-rms}(z)}, \tag{3-50}$$

we relate the time t_{0p} and t_{0c} with γ, using equation (3-45), i. e.,

$$t_{0c} \approx t_{0p} \frac{1+\hat{\gamma}}{2}. \tag{3-51}$$

Equation (3-51) allows us to simply map the P-wave times to converted wave times without the need to convert to interval velocities. We can get the C velocity values by converting $V_{p\text{-}rms}$ (t_o) on approximate depth using the RMS velocities $V_{p\text{-}rms}$ (z) using:

$$V_{c-rms}(z) = \frac{2}{1+\gamma_{Int}(z)} V_{p-rms}(z). \tag{3-52}$$

The estimated $V_{c\text{-}rms}$ velocities in approximate depth are then converted back into time to complete mapping equation:

$$V_{c-rms}(t_{0p}) = \frac{2}{1+\gamma_{Int}(t_{0p})} V_{p-rms}(t_{0p}). \tag{3-53}$$

If we are given the P-wave velocities, and a chosen specific value for γ_{Int}, we can scale the P velocities to C velocities, and then map the P times to the C times. In summary the processing steps are:

1. Create an initial array of $\hat{V}_{c-rms}(n)$ by scaling the amplitude of $V_{p-rms}(n)$ using

$$\hat{V}_{c-rms}(n) = \frac{2}{1+\hat{\gamma}} V_{p-rms}(n). \tag{3-54}$$

2. Resample $\hat{V}_{c-rms}$ (m) to V_{c-rms} (n) using equal increments of m, where

$$m = \frac{1+\hat{\gamma}}{2} n. \tag{3-55}$$

The second method is illustrated in Figure 3.11c where values from the fast method are also plotted in yellow colour ($V_{c\text{-}rms2}$). Note that the time uses by the fast method is less than that of the exact method and only extend to 4 sec. The error between the two methods is shown in Figure 3-11d and is less than 0.1%.

Once we have an initial estimate of V_c, then we can create LCCSP gathers at a few locations to get an improved estimate of V_c from a semblance analysis of the gathers. These

improved or picked V_c velocities were converted to interval velocities and then depth and are displayed as the red curve in Figure 3.11b $V_{c\text{-}int}(Pz)$.

3.9 Estimating the S velocities

3.9.1 Introduction

The previous section of estimating the C velocities in now used to estimate the S velocities for the full prestack migration that uses the DSR equation (3-32).

C velocities are useful for estimating a γ function and S-wave velocities. However, C velocities are not useful for forming CSP gather for a complete prestack migration of P-S data. After the LCCSP gathers have been formed, a new estimate of V_c can be picked from the LCCSP gathers for moveout correction to complete the prestack migration.

The full prestack migration requires P and S velocities that use the DSR equation (3-32), defined at the same depths. Depth arrays are computed from the P and C velocities respectively. The depths of the C velocities are matched to the depths of the P velocities. At a defined depth, P and C velocities are used to compute the S velocities, which are then mapped to the corresponding time of the P velocity. Now, when the DSR equation (3-31) is used to compute a traveltime, the t_0 time can be used for both the P and S velocities. When the S velocities are mapped to $t_{o\text{-}p}$ times, and using the same pseudo depths $\hat{z}_0$ in each of the square roots, equation (3-32) becomes

$$t_c(\hat{z}_0^2) = \frac{1}{V_{p-rms}(\hat{t}_{0p}^2)} \sqrt{\hat{z}_0^2 + (x+h)^2} + \frac{1}{V_{s-rms}(t_{0p}^2)} \sqrt{\hat{z}_0^2 + (x-h)^2} \,, \text{(3-56)}$$

This equation is then used to compute the times and equivalent offset for forming the CSP gathers. After these gathers are formed a third estimated of V_c is obtained from velocity

analysis to apply moveout correction, amplitude scaling, and stacking to complete the prestack migration.
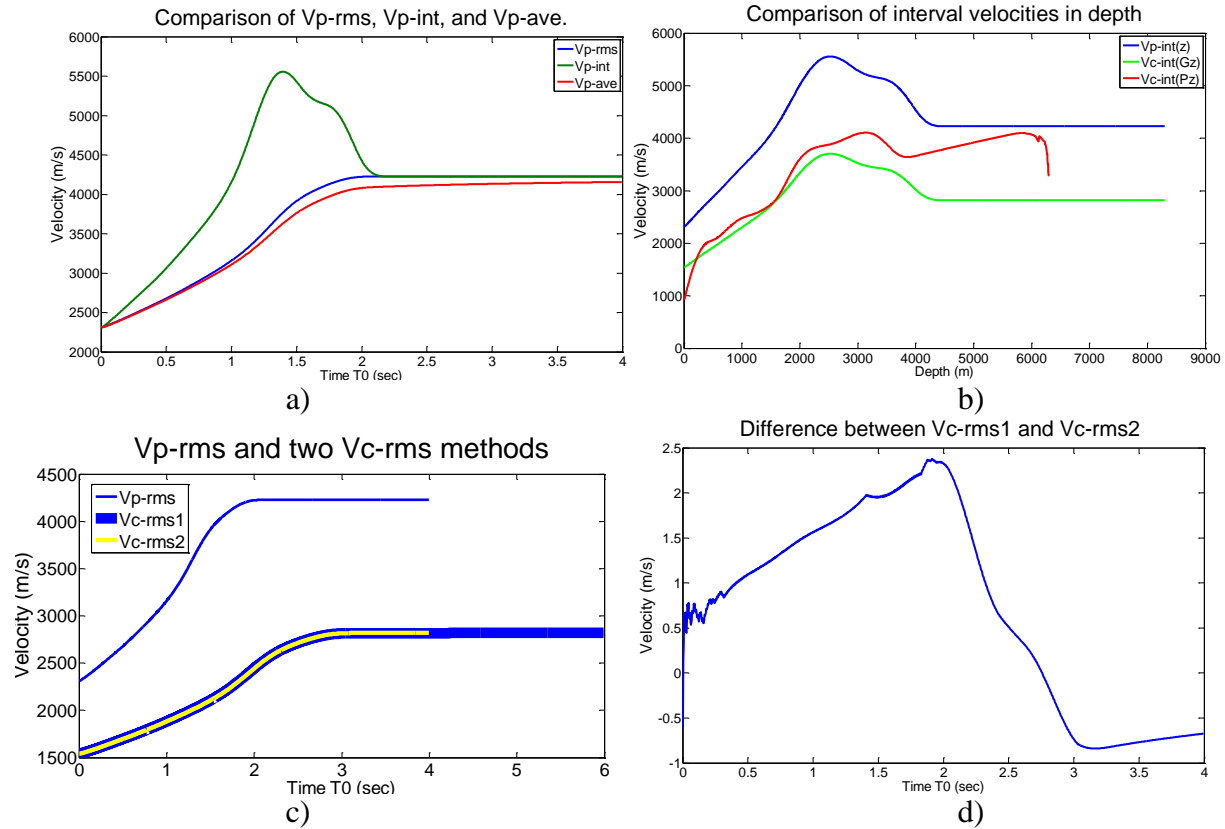
Figure 3.11: Plots of initial estimates of the converted wave velocity V_c with a) the RMS, interval, and average P velocities, b) the interval P and C velocities in depth, c) the P RMS velocities and the two methods of computing the C RMS velocities in time, and d) the error in the two methods of computing C RMS velocity V_c.

3.9.2 Computing the S velocities

The interval S velocities $V_{s\text{-}Int}$ are computed similar to the V_c process using $V_{p\text{-}Int}$ and $V_{c\text{-}Int}$ from equation (3-26 at the same depth $\hat{z}_0$ from

$$V_{s-Int}(\hat{z}_0) = \frac{V_{p-Int} * V_{c-Int}}{2V_{p-Int} - V_{c-Int}}. \qquad (3\text{-}57)$$

The interval velocities $V_{p\text{-}Int}$, $V_{s\text{-}Int}$ and $V_{c\text{-}Int}$ in time are shown in Figure 3.12a.

The interval S velocities $V_{s\text{-}Int}$ are then converted to RMS velocities, $V_{s\text{-}rms}$, and mapped to

P times at the corresponding depth.

3.9.3 Fast methods of Vs

The comparison required by this process can be performed more efficiently similar to the

V_c process with the assumptions of $\hat{z_0}$ that is computed from the RMS velocities $V_{p\text{-}rms}$ and $V_{c\text{-}rms}$

when

$$\hat{z}_{Vs-rms}(t_s) = \hat{z}_{Vp-rms}(t_p) \ , \tag{3-58}$$

then

$$\breve{V}_{c-rms}(t_p) = V_{c-rms}(t_c) \ , \tag{3-59}$$

and we estimate $V_{s\text{-}rms}$ from

$$V_{s-rms}(t_p) = \frac{V_{p-rms}(t_p) * \breve{V}_{c-rms}(t_p)}{2V_{p-rms}(t_p) - \breve{V}_{c-rms}(t_p)} \ . \tag{3-60}$$

Figure 3.12b shows this RMS Velocity $V_{s\text{-}rms}$ using the method 1, $V_{s\text{-}rms\ exact}$ and method 2,

$V_{s\text{-}rms\ fast}$. Figure 12.3c shows the RMS velocities for P, S and C, ($V_{p\text{-}rms}$, $V_{s\text{-}rms,}$ $V_{c\text{-}rms}$, and $V_{s\text{-}rms}$

(t_p).

The improved estimate of V_c is used for as initial estimate of V_s for the formation of the

unlimited CCSP gathers. The V_p and V_s velocities in t_{op} times can then be used to compute the

RMS velocity value for γ. Figure 12.3d shows a γ function from the Interval velocities in blue,

from the RMS velocities in green, and from a well log in red.
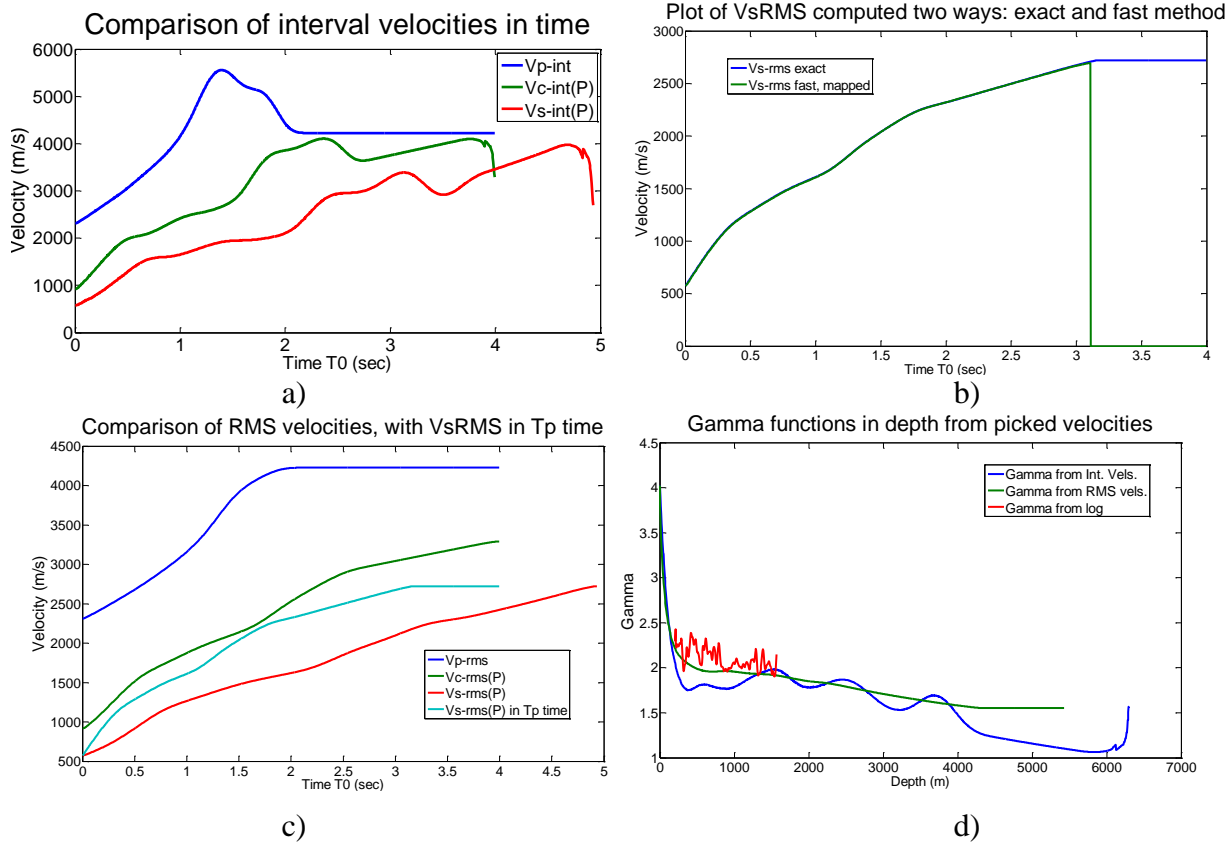
Figure 3.12: Plots of initial estimates of the converted wave velocity V_s with a) the Interval P, C and S velocities, b) the RMS S velocity using two methods of computing the RMS velocities in time, c) the RMS velocities P, S and d) Gamma functions from interval velocities, RMS velocities, and the well log.

Chapter Four: **Results**

4.1 Introduction

The theory presented in Chapter 3 was tested with synthetic data and real data from Hussar and Northeastern British Columbia areas.

In each case V_c was first estimated from V_p using a constant γ, then LCCSP gathers were formed. New V_c velocities were picked from these gathers. The V_p and new V_c velocities were then used to compute the S velocities V_s. Both V_p and V_s where then used for C-EOM method of prestack migration of the converted wave data.

4.2 Data

4.2.1 Hussar

4.2.1.1 Acquisition

These seismic data were acquired by CREWES in collaboration with Husky Energy, GeoKinetics and Inova in September 2011. The experiment was conducted near Hussar, Alberta. Figure 4.1 shows the location of the study area, and the direction of the 2D line with the well locations nearby. The survey was designed to test the use of different sources and receivers to investigate the extension of the seismic broadband as far into the low frequency range as possible without sacrificing the higher frequencies (Isaac et al., 2011; Margrave et al., 2011). Both dynamite and Vibroseis sources with five different types of receivers were used in this experiment.

The sources included dynamite (2 kg) and two different Vibroseis: INOVA's AHV-IV (model 364), and conventional Eagle Failing Vibroseis (Y2400) with low-dwell sweep. The INOVA 364 vibrator is specially designed to operate at low frequencies. The line was shot twice

with different sweeps using this vibrator: a special low-dwell sweep and a normal linear sweep, both extending from 1 to 100 Hz.

The type of receivers used were 3C 10 Hz Sensor SM7 geophones, 1C 4.5 Hz Sunful geophones, 3C Vectorseis accelerometers, Nanometrics Trillium seismometers, and 1C 10 Hz SM24 high sensitivity geophones.

The combination of all of these sources and receivers result in a quite large dataset, consisting in a total of 12 PP section and 8 P-S sections (Margrave et al., 2011).

The data were recorded to 10 seconds at sample rate of 2 msec. The line is 4.5 km long and runs NE-SW. Figure 4.1 shows the location of the study area, and the Hussar seismic line with the well locations nearby

The analysis to be shown in this section is for the datasets acquired with 3C SM7 10 Hz geophones, and an INOVA 364 Vibroseis a with a custom low-dwell sweep as a source. The sweep length was 24 seconds with a 10 second listen time. The sources spacing was 20 m and the receivers spacing was 10 m. In addition to the seismic data, well information was added to this thesis. Compressional sonic logs and shear sonic logs from a well (from 208 m to 1569 m depth) over the 2D line are also considered in this study.

4.2.1.2 Processing

The P-P and P-S radial dataset were processed at the University of Calgary by Dr. Helen Isaac at the University of Calgary through a standard processing sequence illustrated in Figure 4.2 and 4.3 respectively, using ProMAX processing software. The data was preprocessed to a horizontal datum at the mid elevation of the topography. The standard processing steps of noise removal, amplitude recovery, and deconvolution were also applied. The receiver statics of the

converted wave data required special attention and were estimated by investing the lateral variability in the time events identified on the common receiver stacks (CRS)(Ion and Galbraith, 2011).
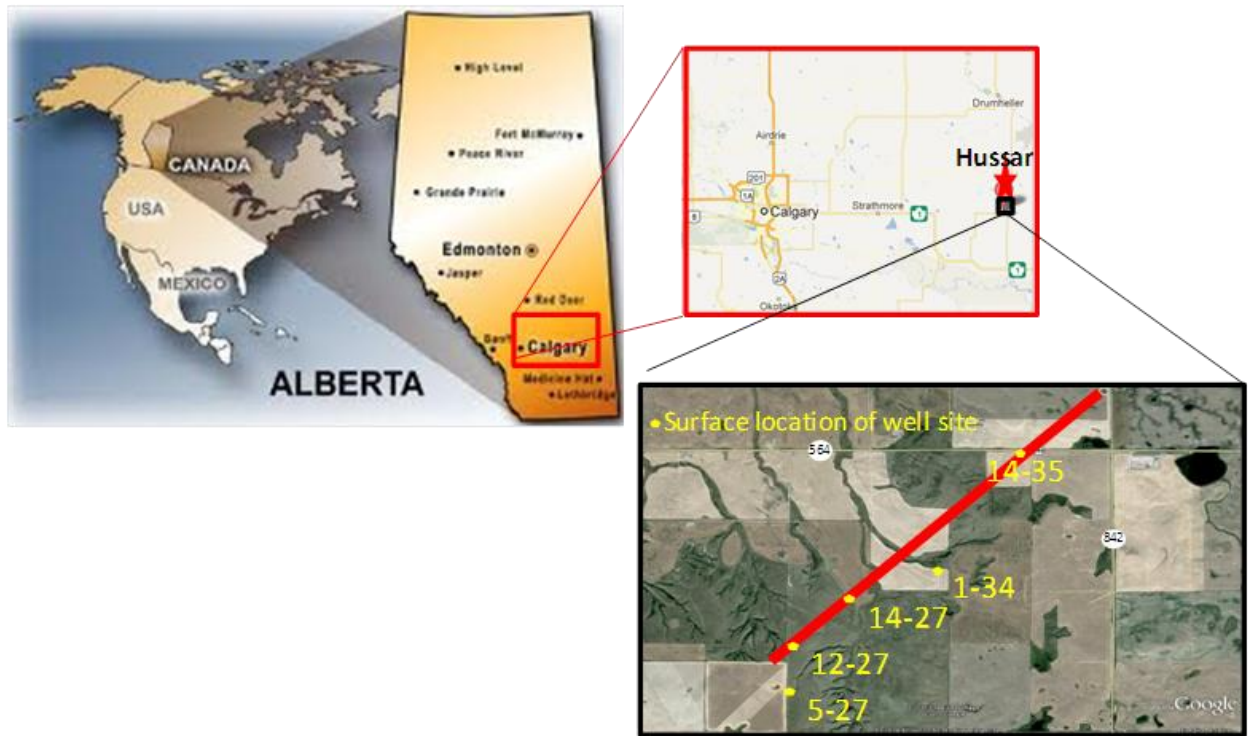
Figure 4.1: Area of study including the Hussar seismic line and the location of nearby wells. After Margrave et al., 2011.
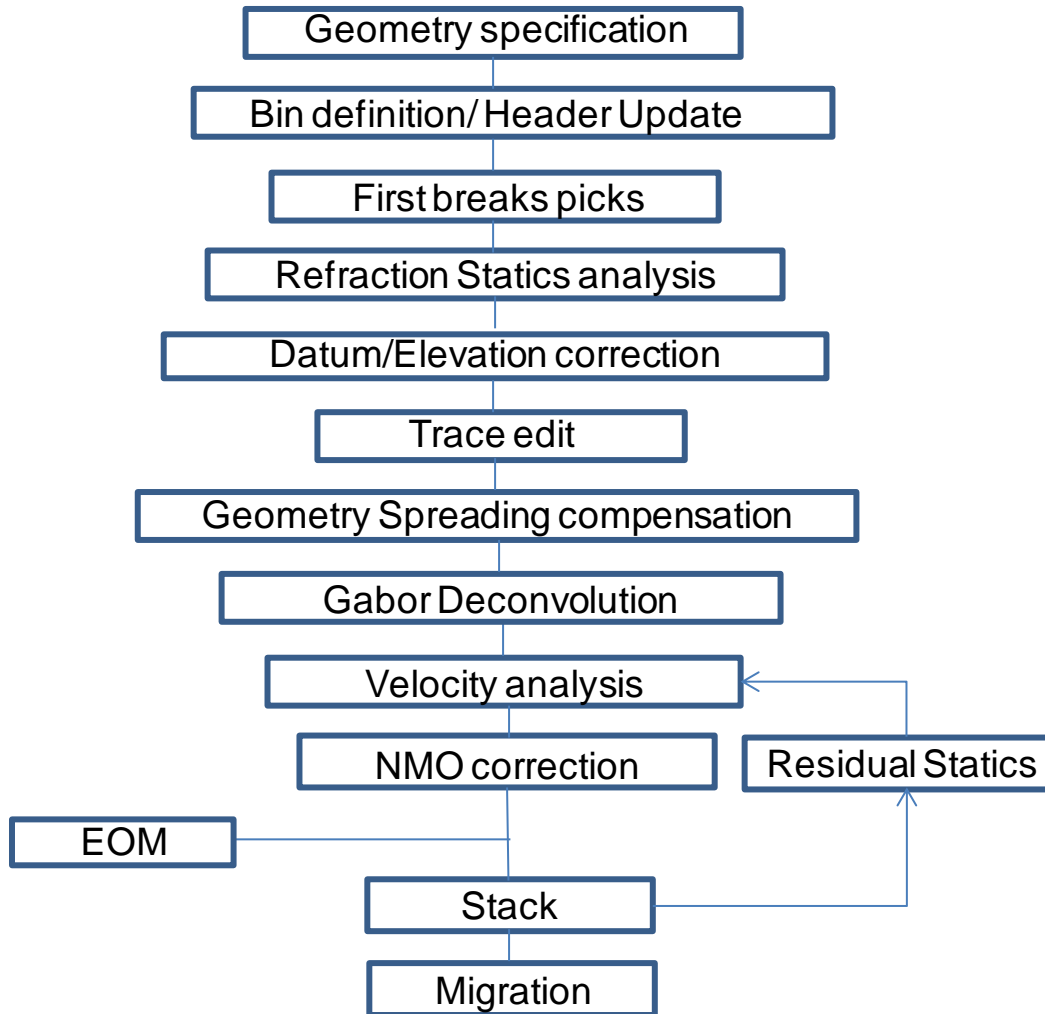
Figure 4.2: Processing flow for the PP Hussar seismic dataset. (Helen Isaac, 2012 personal communication)

After the velocity analysis, the dataset is ported to MatLab to apply EOM code which generates CSP gathers that were then ported to Vista software for velocity analysis, NMO correction and Stack. The prestack migration is completed at this step. Figure 4.4 shows the flow processing for EOM data.

A more accurate and simple method to estimate V_c using the equivalent offset method with short offsets was explained in Chapter 3. The radial component line was processed with the

Equivalent Offset algorithm. The equivalent offset gathers were formed with a limited range of lateral displacements.


```
Rotation into radial component
        Asymptotic CCP binning
    Geometry Spreading compensation
    Import P-wave shot static and applied
Calculate and applied receiver elevation S statics
            Edit bad traces
    Noise attenuation: Radial filter
          Gabor Deconvolution
    Surface wave noise attenuation
      Velocity analysis, Initial Vc
  Common Receiver Brute Stack (CRS)
  Estimate S-wave receiver statics from CRS
Check the CRS for additional significant receiver statics
      Repeat S-wave receiver statics
  EOM
            PS wave Stack
              Migration
```

Figure 4.3: Processing flow for the P-S Hussar seismic dataset. (Helen Isaac, 2012 personal communication)

51

```
┌─────────────────────────────┐
│  Generation of CSP gathers  │
└──────────────┬──────────────┘
    ┌──────────┴──────────┐
    │  Velocity analysis  │
    └──────────┬──────────┘
      ┌────────┴────────┐
      │  NMO correction │
      └────────┬────────┘
        ┌──────┴──────┐
        │    Stack    │
        └─────────────┘
```
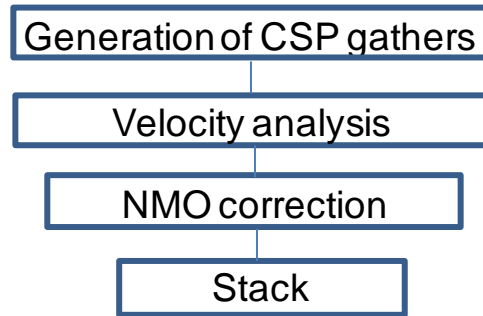
Figure 4.4: Processing flow for EOM.

4.2.1.3 First estimate of V_c

As was mentioned earlier, there is a short range of usable data when the CMP displacement x is small, therefore a simple velocity analysis will provide a converted wave velocity V_c.

Tests to find a best displacement x, was conducted using eighteen traces spaced evenly across the line. These tests were done using three methods:

1. Supergather

2. EO using a simplified (equation (2-12) or (3-38))

3. A Full EO method (equation (2-9))

The test was conducted using eighteen supergathers spread evenly across the line. This was repeated using values of x_{max} ranging from 25, 50, 100, 200, 400, to 800 m, and then stacked with the first estimate of V_{c-rms} using the V_{p-rms} velocity and $\gamma=2$. The results are shown in Figure 4.5 which shows the eighteen stacked traces, (micro-stack), for each x_{max}. The quality of the traces improves with increased x and could be used for an initial estimate of V_c. However, these data are very flat and not all supergathers of this size are used, as they depend on offset.

The test was repeated using methods 2 and 3, using the same values of x_{max}, as shown in Figure 4.6 and Figure 4.7 respectively. The panel with x_{max} 100 m shows the better image of the reflectors mainly in the shallow part of the sections above 1.0 sec and tended to produce more coherent energy. An example of one limited LCCSP gather is shown in Figure 4.8 for $x_{max} = 100$ m, in the central portion of the line.

The CSP gathers were formed and normal moveout was applied using the first estimate of $V_{c\text{-}rms}$ and $\gamma=2$ using the methods described in chapter 3. Figure 4.8 shows the LCCSP gathers formed by a supergather using a maximum displacement x of 100 m (top). The same LCCSP gathers section with NMO correction (bottom). Figure 4.9 and 4.10 shows the LCCSP gathers formed by EO simplified method and Full EO method, respectively, using a maximum displacement x of 100 m (top). The same LCCSP gathers section with NMO correction (bottom).

The following describes the process of forming the velocities by matching traveltimes of the velocity procedure explained in chapter 3. Figure 4.11a shows a comparison of P-wave velocities: RMS, interval velocity and average velocity, $V_{p\text{-}rms,}$ $V_{p\text{-}int}$ and $V_{p\text{-}ave}$ (step 1, using method 1). Figure 4.11b shows a comparison between interval velocity for P- and C-waves, using $\gamma=2$ (step 3, method 1). Figure 4.11c shows a comparison of interval velocities in depth for P- and C-wave data, $V_{p\text{-}int}$ and $V_{c\text{-}int}$ are in blue and green respectively. Figure 4.11d shows a comparison of RMS velocities for C-wave using method 1, $V_{c\text{-}rms\text{-}1}$ (in blue), and method 2, $V_{c\text{-}rms2}$ (in yellow).

4.2.1.4 Second estimation of V_c Velocities

After an initial estimate of V_c, LCCSP gathers at a few locations allow us to get an improved estimate of V_c from a semblance analysis of the gathers. Figure 4.12 shows a semblance panel for a CSP located in the middle of the line, formed with $x_{max}= 100$ m and

produced using (a) supergathers, (b) EO simplified, (c) full EOM methods from 0 to 4000 msec.

Parts (d), (e), and (f) are the same semblance plot from 0 to 600 msec. The panel formed with the

full EO method show a better focus of the energy mainly in the shallow part of the section.
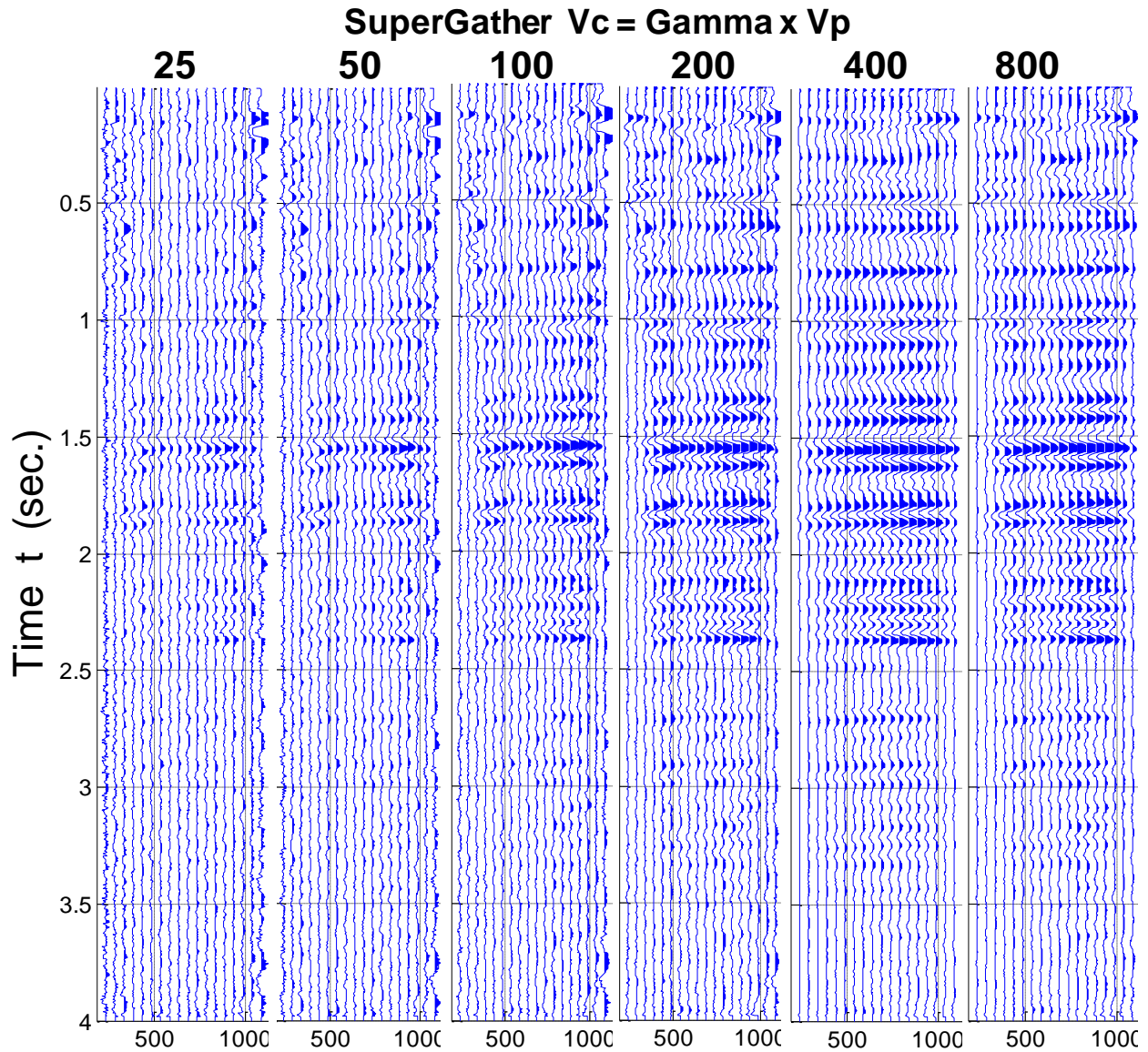
Figure 4.5: Six micro-stacks formed for various x_{max} as identified by the distance in meters on the top of each panel. The CSP gathers were formed using Super-Gathers. The bottom of each panel indentifies the CMP number of the stacked traces. Each panel, (micro-stack), contains eighteen traces taken at equal increments across the converted wave line.
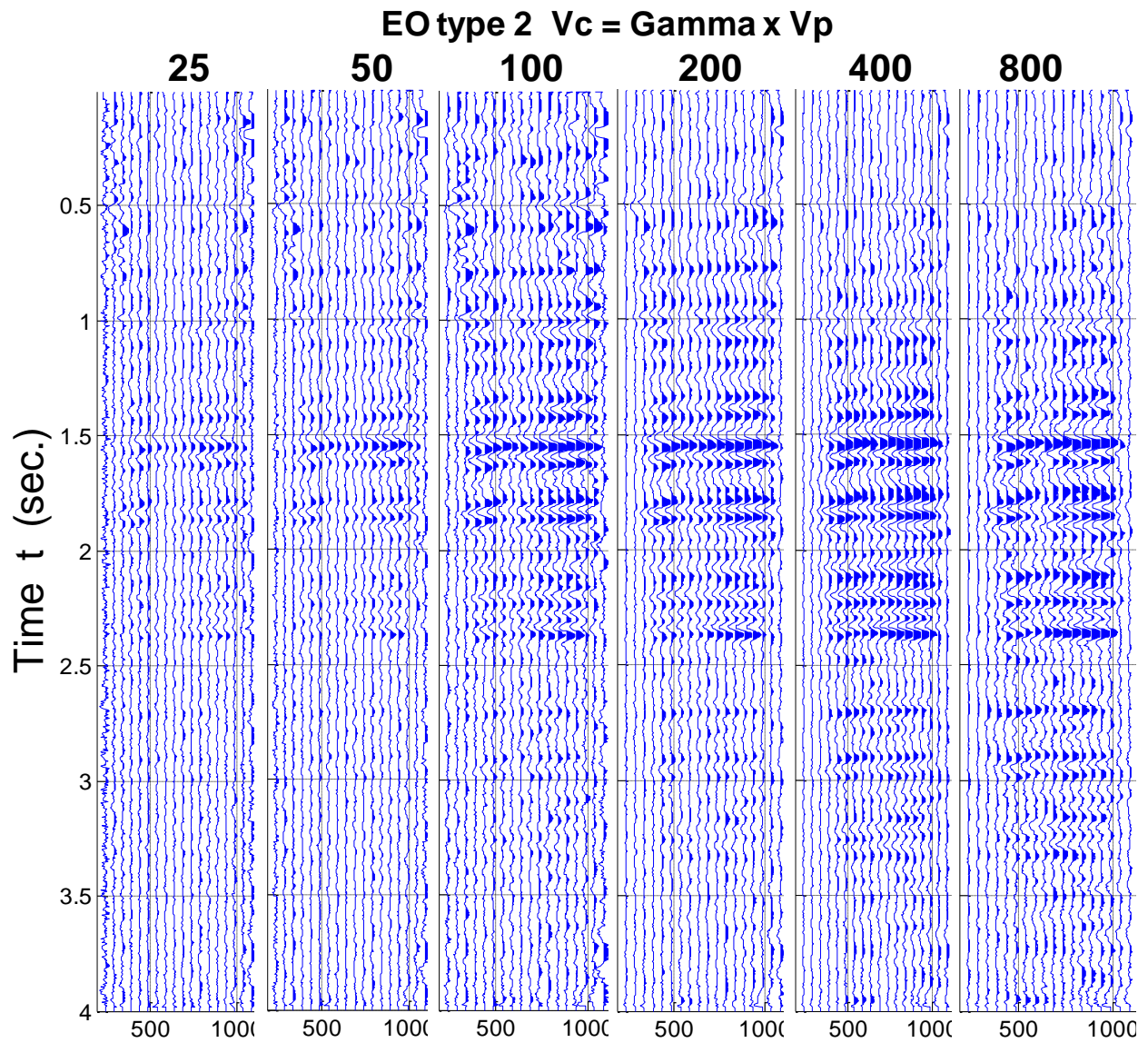
Figure 4.6: Six micro-stacks formed for various x_{max} as identified by the distance in meters on the top of each panel. The CSP gathers were formed using simplified EOM. The bottom of each panel indentifies the CMP number of the stacked traces. Each panel, (micro-stack), contains eighteen traces taken at equal increments across the converted wave line.
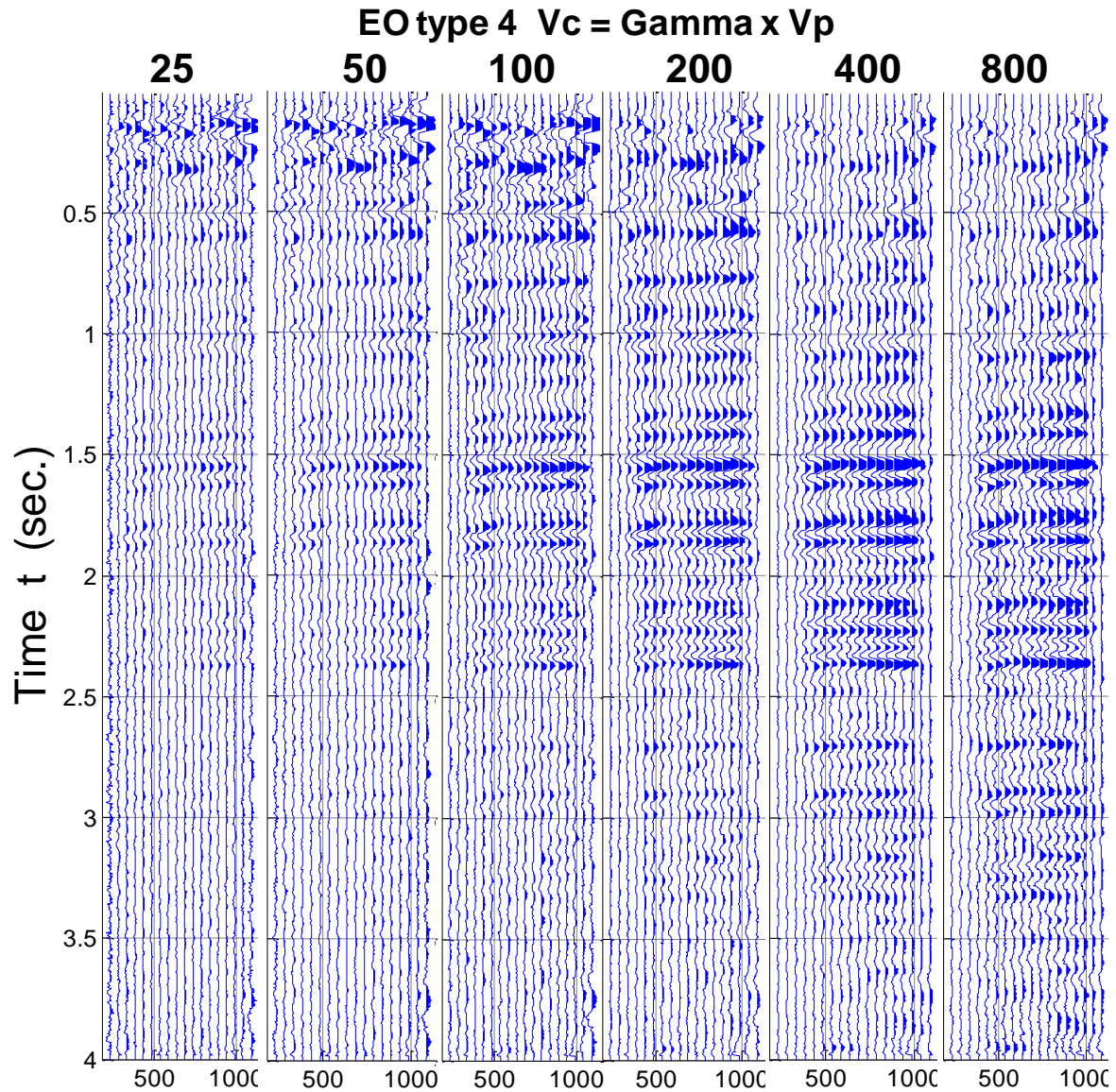
Figure 4.7: Six micro-stacks formed for various x_{max} as identified by the distance in meters on the top of each panel. The CSP gathers were formed using full EOM type 4. The bottom of each panel indentifies the CMP number of the stacked traces. Each panel, (micro-stack), contains eighteen traces taken at equal increments across the converted wave line. .
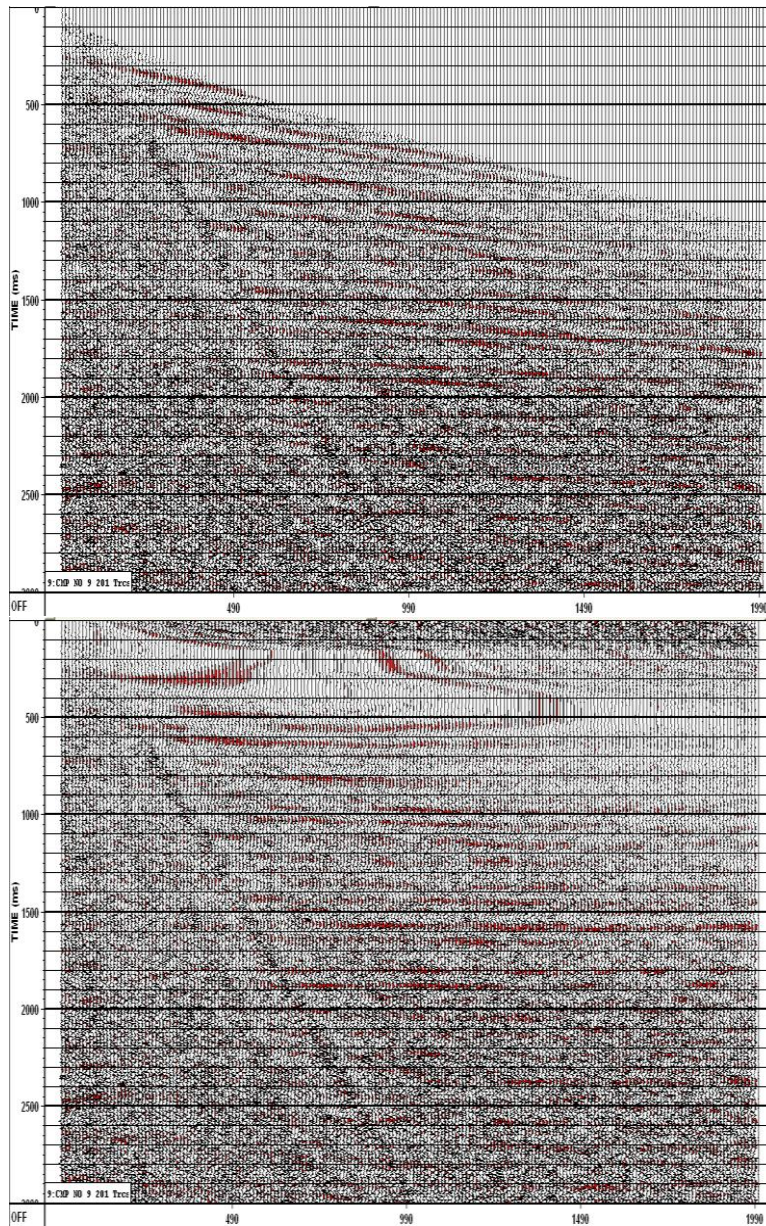
Figure 4.8: Limited converted wave CSP gathers (LCCSP) (top) and after applied NMO correction (bottom) formed by a supergather.
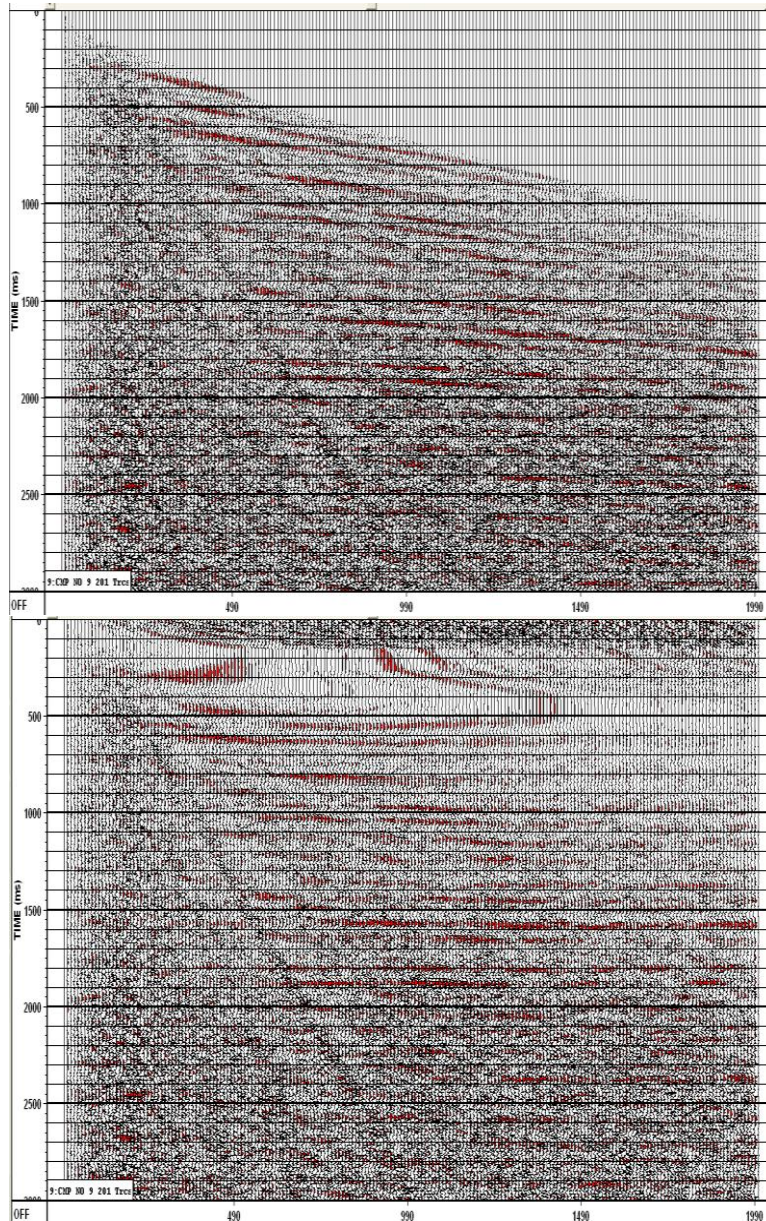
Figure 4.9: Limited converted wave CSP gathers (LCCSP) (top) and after applied NMO correction (bottom) formed by EO simplified.
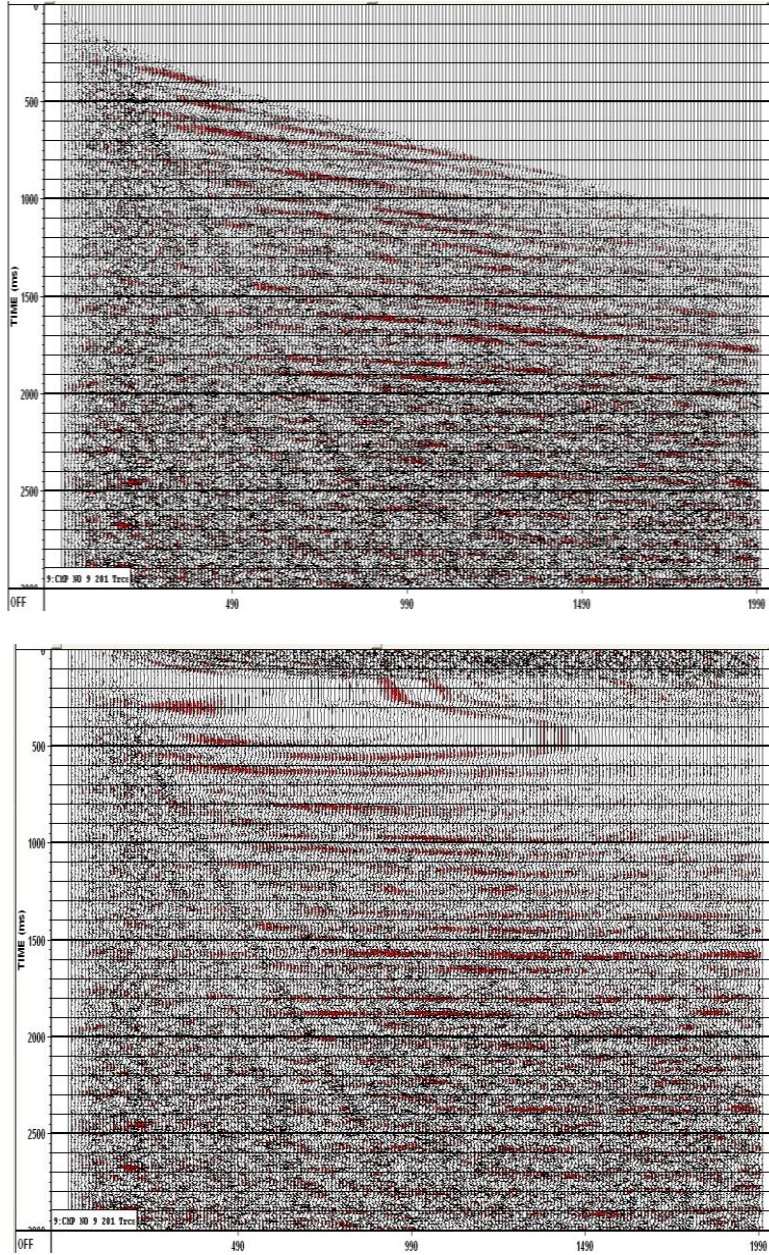
Figure 4.10: Limited converted wave CSP gathers (LCCSP) (top) and after applied NMO correction (bottom) formed by Full EO method
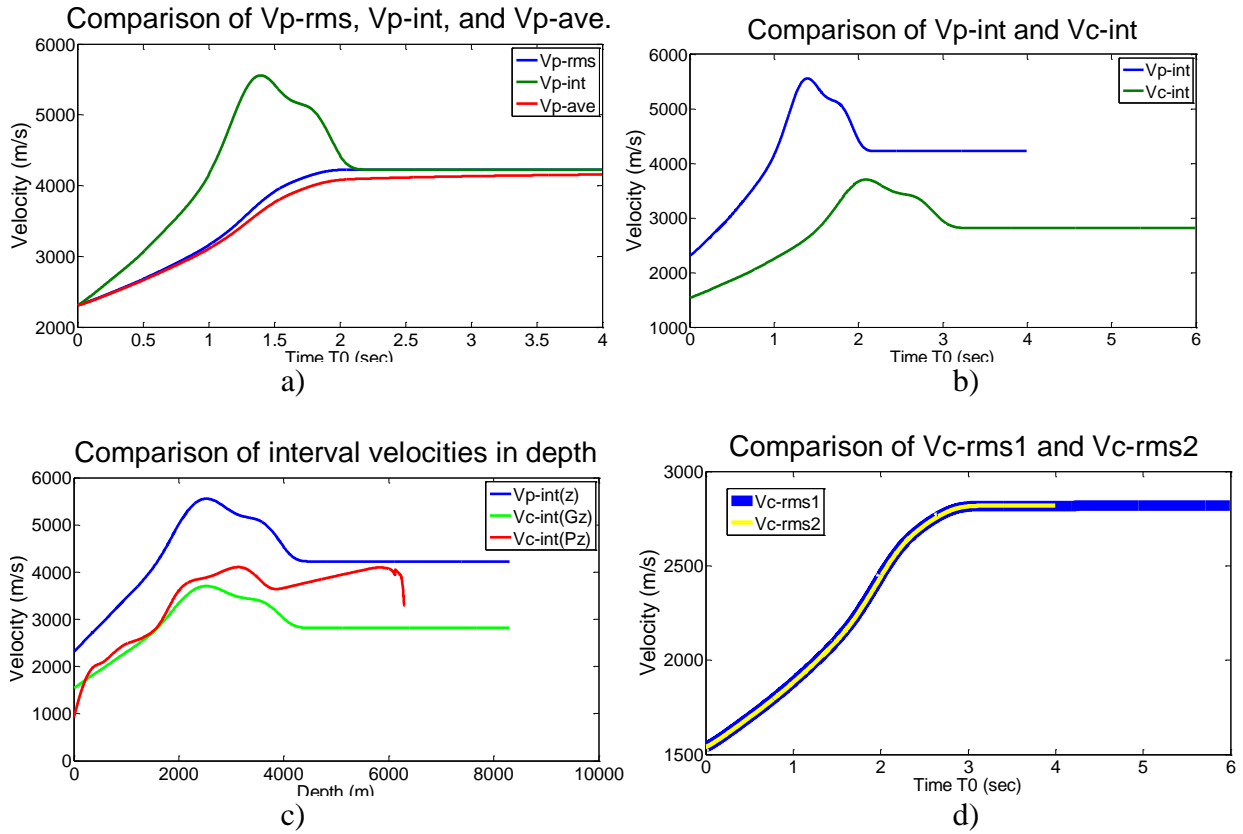
Figure 4.11: Sequence delineating progress from RMS P velocities to interval P and C velocities, then back to RMS C velocities. a) a comparison of P-wave velocities: RMS, interval velocity and average velocity, (b) velocity for P- and C-wave, using γ=2, c) comparison of interval velocities in depth for P- and C-wave, and d) a comparison of RMS velocities for C-wave using method 1 (in blue), and method 2 (in yellow).
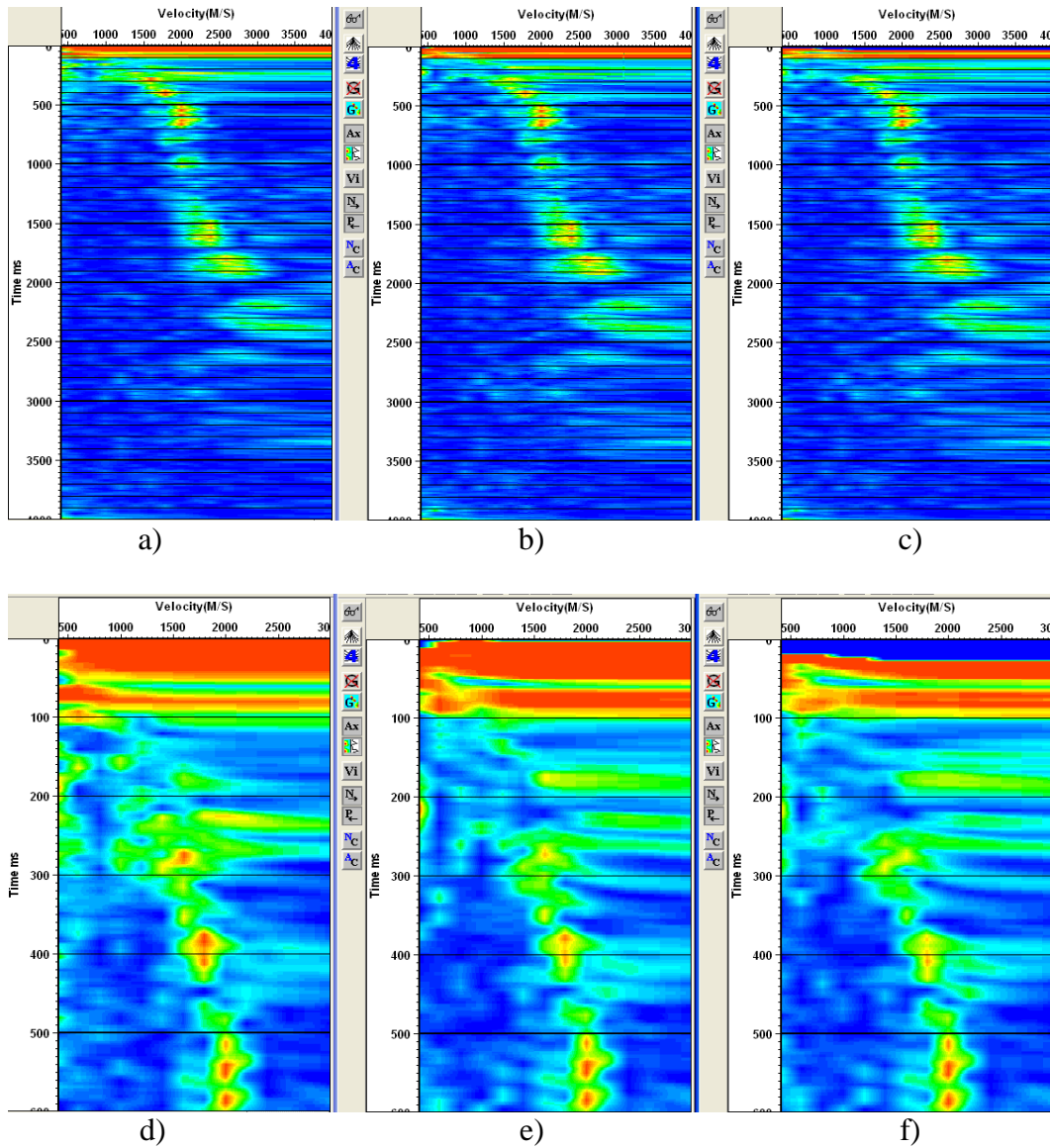
Figure 4.12: Three semblance panels formed with x_{max}= 100 m and from 0 to 4000 ms. The left panel a) was obtained with supergathers, b) the middle uses EO simplified, and c) the right is uses the full EO. The same semblance plots d), e), and f) are corresponding expanded views from 0 to 600 msec

Velocity analysis of the LCCSP gathers produced a more accurate velocity estimate of $V_{c\text{-}rms}$ (P) than $V_{c\text{-}rms}$ (G) computed from $V_{p\text{-}rms}$. These velocities are compared in Figure 4.13a, showing the original $V_{p\text{-}rms}$ velocity in blue, $V_{c\text{-}rms}$ (G) computed from $V_{p\text{-}rms}$ in green, and the more accurate $V_{c\text{-}rms}$ (P) in red. It is interesting to note that the two converted wave velocities are equally close to a time of 1 to 1.5 sec, corresponding to the best horizontal fit of the moveout

61

data in Figure 4.10. Figure 4.14b shows a comparison between interval velocities for P-wave and converted wave data derived from P-wave data and using γ=2 and picked from the CSPs in time (b), and (c) in depth.

a)

b)

c)
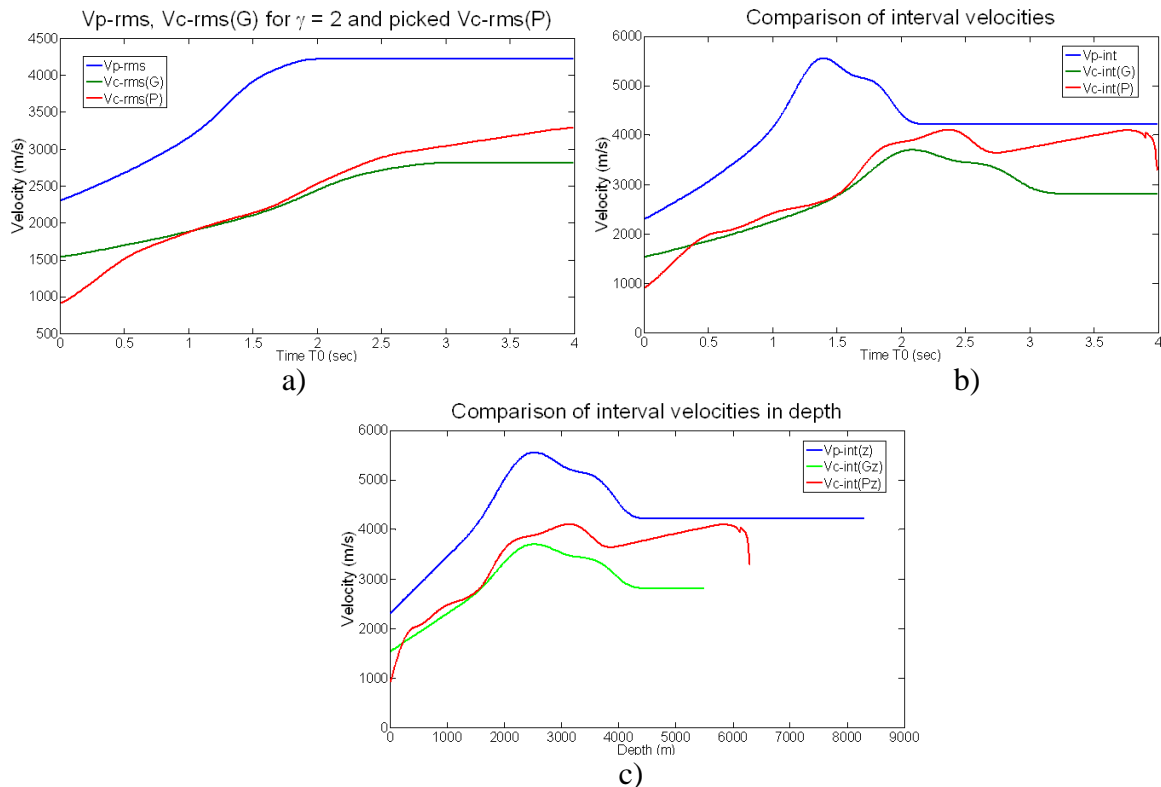
Figure 4.13: a) Comparison of the velocities $V_{p\text{-}rms}$, and $V_{c\text{-}rms}$ (G) computed from $V_{p\text{-}rms}$, and more accurate $V_{c\text{-}rms}$ (P), b) Comparison between P-wave interval velocities $V_{p\text{-}Int}$, and converted wave velocities derived from P-wave using γ=2 $V_{c\text{-}Int}$ (G), and accurate $V_{c\text{-}Int}$ (P), in time, c) in depth

Now that an improved $V_{c\text{-}rms}$ is obtained, shear velocities can be estimated. Figure 4.14.a shows interval velocities for P-, C-, and S-wave velocities in time and the same interval velocities in depth is shown in Figure 4.14.b. Figure 4.14c shows the RMS velocities for P-, C-, and S-waves. The last velocity mentioned is shown in t_p time as the cyan curve.

62
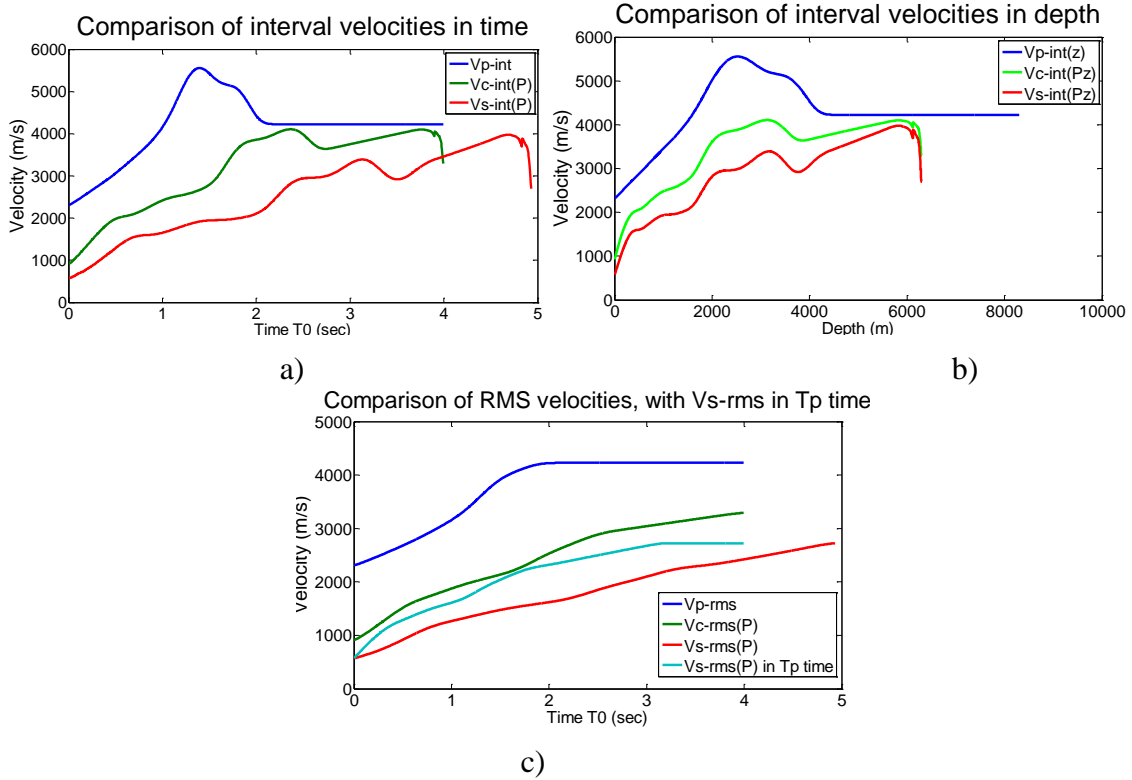
Figure 4.14: a) **Comparison between interval velocities for P-wave $V_{p\text{-}Int}$, , C-wave and S-wave in time, b) the same in depth. c) Comparison of RMS velocities for P, C and S, $V_{p\text{-}rms}$, $V_{c\text{-}rms}$, and $V_{s\text{-}rms}$.**

The interval velocities derived from picked velocities are compared with velocities measurements from a well log, as illustrated in Figure 4.15a for P-P data, and (b) for P-S data. Using these velocities, a new estimate of γ can be obtained. Figure 4.15c shows the new estimated γ in depth and the initial γ used. The new estimate of γ tends to be higher than 2.0 near the surface, and lower than 2.0 deeper in the section as anticipated, though these are only initial estimates. The new gamma function derived from $V_{c\text{-}rms}$ from $V_{p\text{-}rms}$ using γ=2, and from $V_{c\text{-}rms}$ picked is now ready be to compared with the logs of Well 12-27, which contains information from 208 to 1585 meters.

63
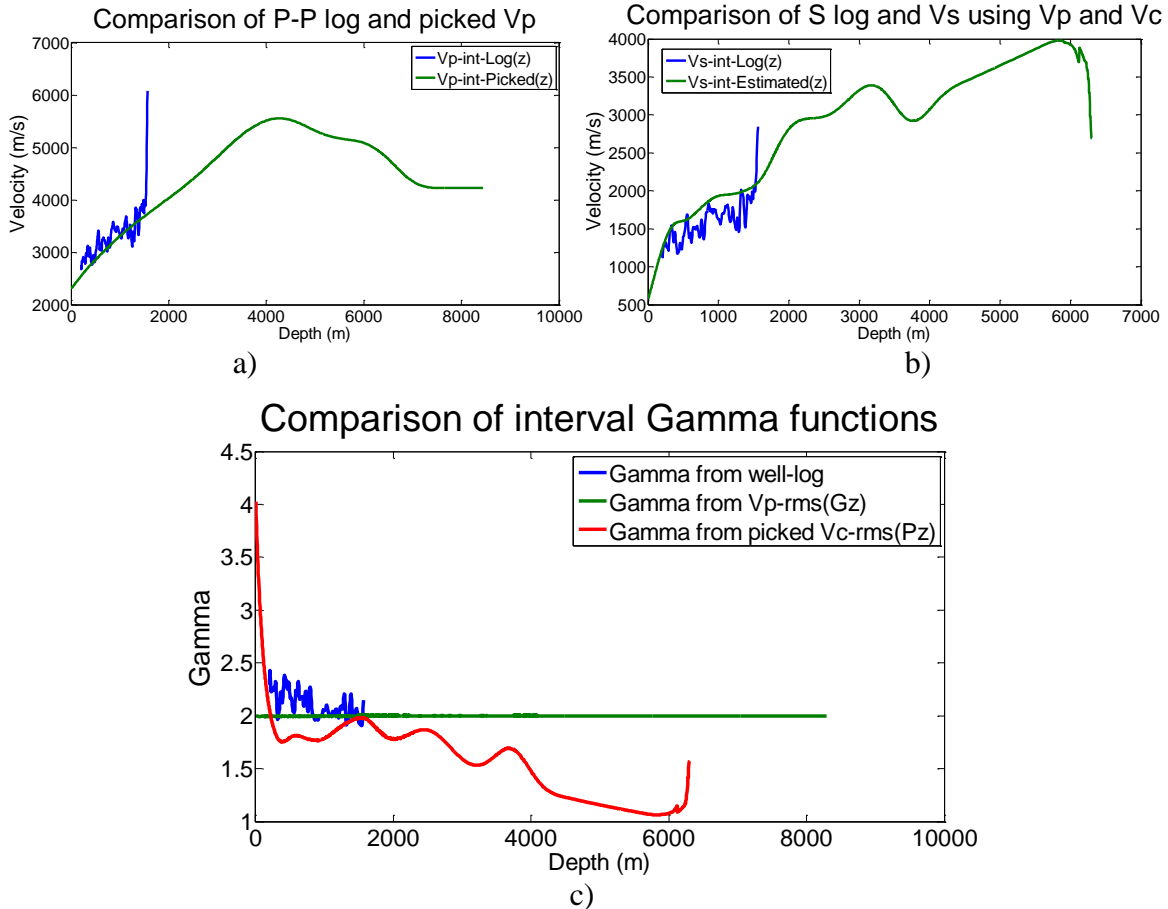
Figure 4.15: Comparison between interval velocities from well logs and estimated values with a) Vp and, b) Vs, and c) comparison of estimated γ functions derived from the well logs, the assumed initial value of γ=2, and γ derived from picked P and C velocities.

The new velocity $V_{c\text{-}rms}$ was used to repeat the test with a supergather of eighteen traces using various values of x_{max} from 25, 50, 100, 200, 400, and 800 m, as indicated at the top of the panels in Figure 4.16. The supergathers show better images of the reflectors with increasing x_{max}.

Again, the test was repeated using the simplified and the full EO method, and using the same values of x_{max}, to derive the results shown in Figures 4.17 and Figure 4.18 respectively. The panels with x_{max} 100 and 200 m show better images of the reflectors mainly in the shallow part of the sections, above 1.0 sec.

The full EO method was applied to form all CCSP gathers using the best velocity V_c. After the gathers were formed, new velocities $V_{c\text{-}rms}$ were picked, and NMO with a stretch mute

of 60 % for P-P data and 100 % for P-S data was applied. The gathers were then stack. Figure 4.19a shows a CSP gather around in the middle of the line, with NMO applied in (c) and after applying stretch mute of 60 % in (e). Figure 4.19b shows a CCSP gather around in the middle of the line, with NMO applied in (d) and after NMO correction and applying stretch mute of 100 % in (e).

Figure 4.20a shows the final stacked P-P and (b) the P-S sections after EOM. Figure 4.21a shows the P-P poststack migrated section (b) the P-S poststack migrated section, processed by Dr. Helen Isaac using a Finite Difference algorithm. The final stacked of Figure 4.20 and 4.21 have the same band pass 0rmsby filter of 5-10-60-80 Hz, and the AGC gain scaling for purpose display. Figure 4.22 shows both final stack sections after EOM with P-S scaled to an approximate P-P time. Figure 4.23 shows an amplitude spectrum graph for unfiltered final stack after EOM for (a) P-P data, and (b) P-S data.
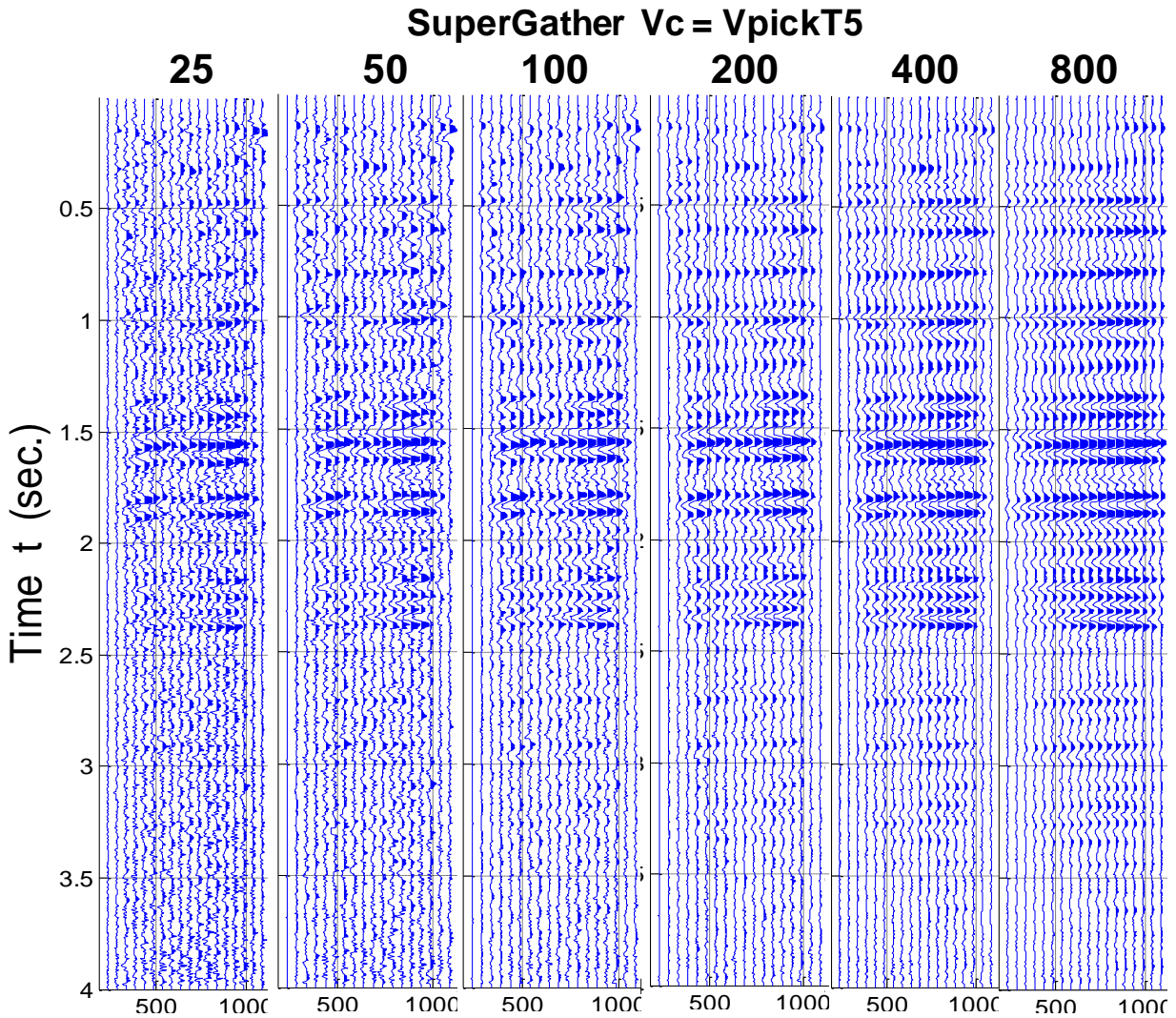
Figure 4.16: Six micro-stacks formed for various x_{max} as identified by the distance in meters on the top of each panel. The CSP gathers were formed using Super-Gathers and the new velocity $V_{c\text{-}rms}$.. The bottom of each panel indentifies the CMP number of the stacked traces. Each panel, (micro-stack), contains eighteen traces taken at equal increments across the converted wave line.
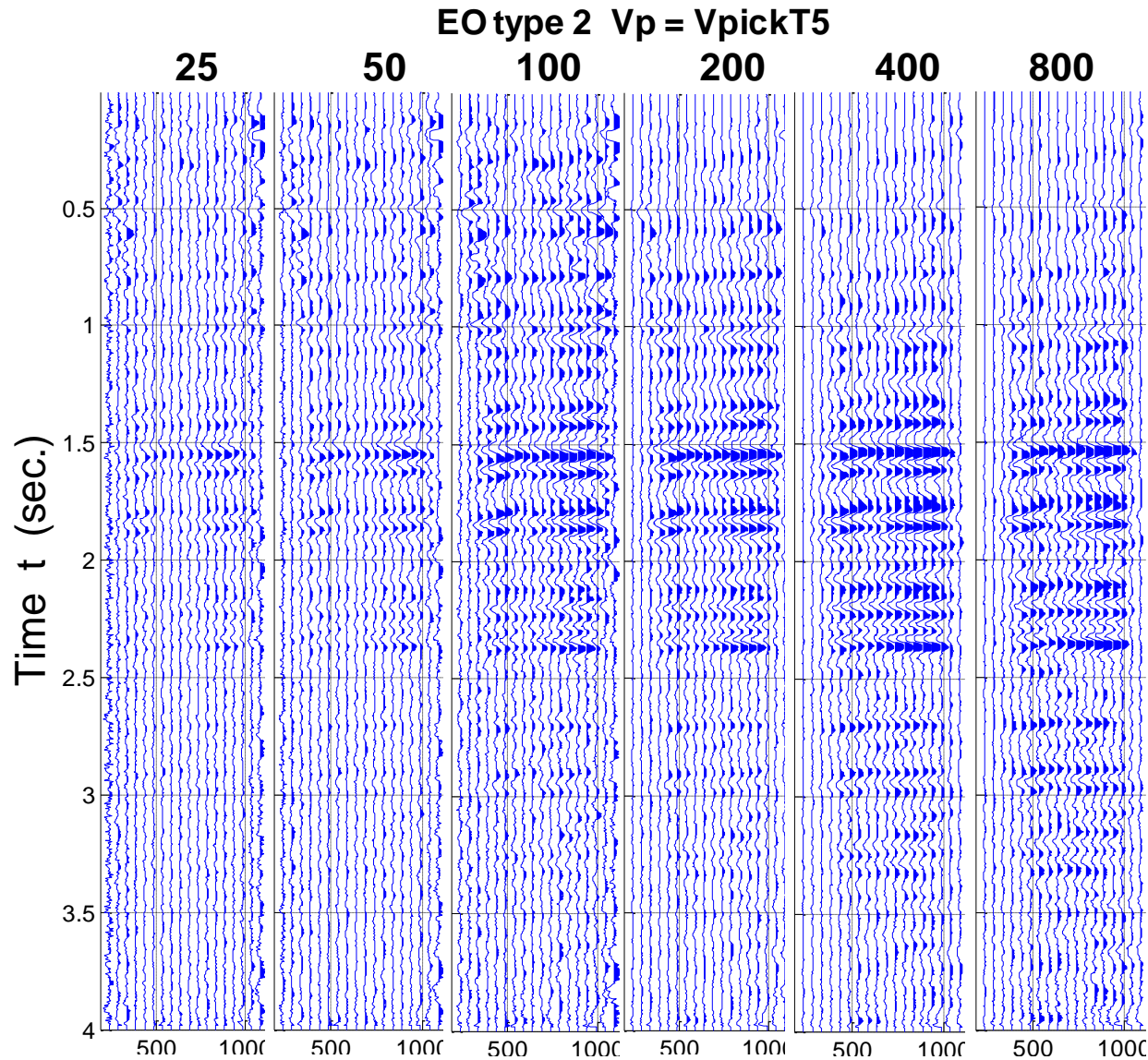
Figure 4.17: Six micro-stacks formed for various x_{max} as identified by the distance in meters on the top of each panel. The CSP gathers were formed using simplified EOM and the new velocity $V_{c\text{-}rms}$. The bottom of each panel indentifies the CMP number of the stacked traces. Each panel, (micro-stack), contains eighteen traces taken at equal increments across the converted wave line.

EO type 4   Vp = VpickT5
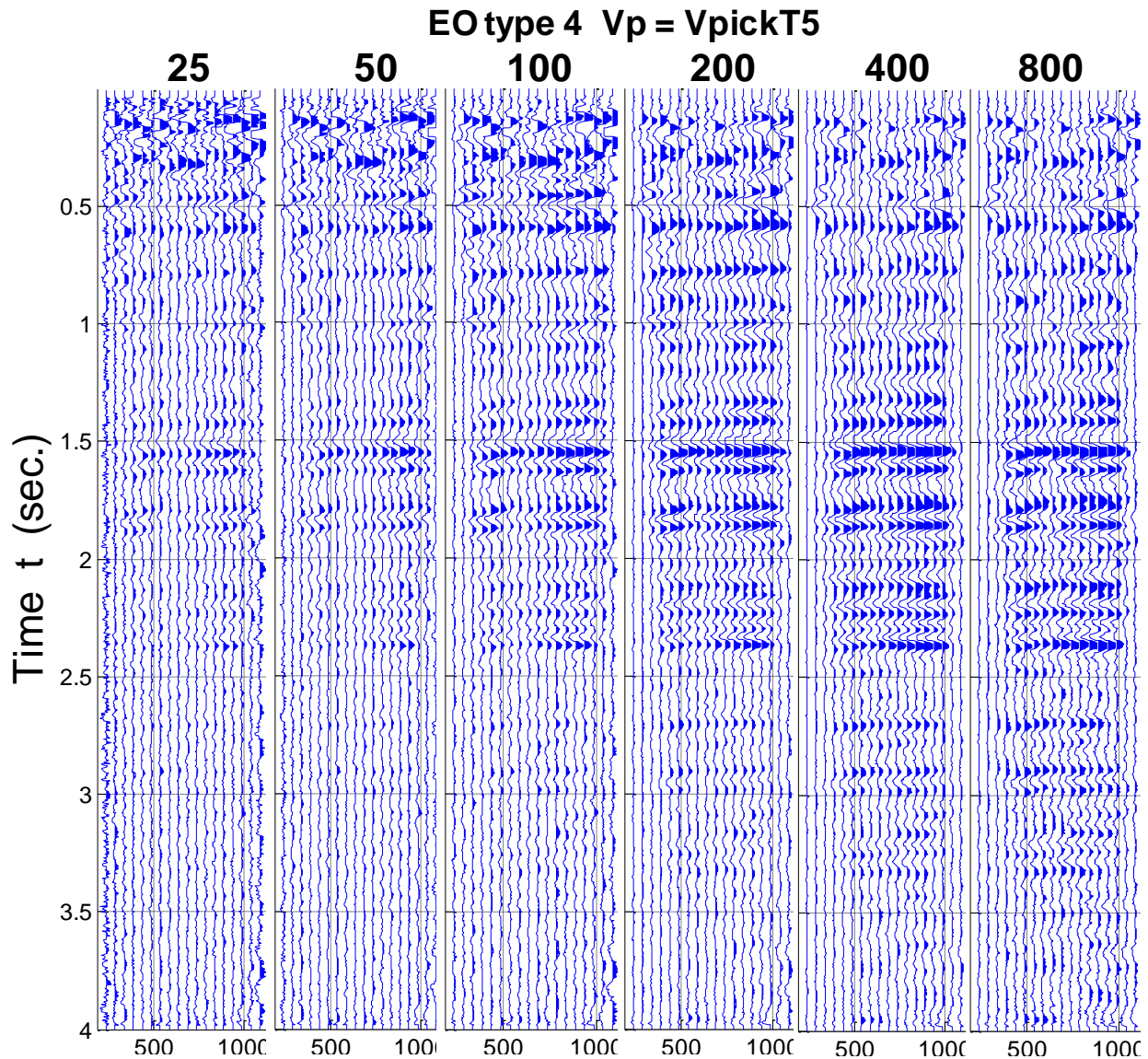
Figure 4.18: Six micro-stacks formed for various x_{max} as identified by the distance in meters on the top of each panel. The CSP gathers were formed using full EOM type 4 and the new velocity $V_{c\text{-}rms}$.. The bottom of each panel indentifies the CMP number of the stacked traces. Each panel, (micro-stack), contains eighteen traces taken at equal increments across the converted wave line.
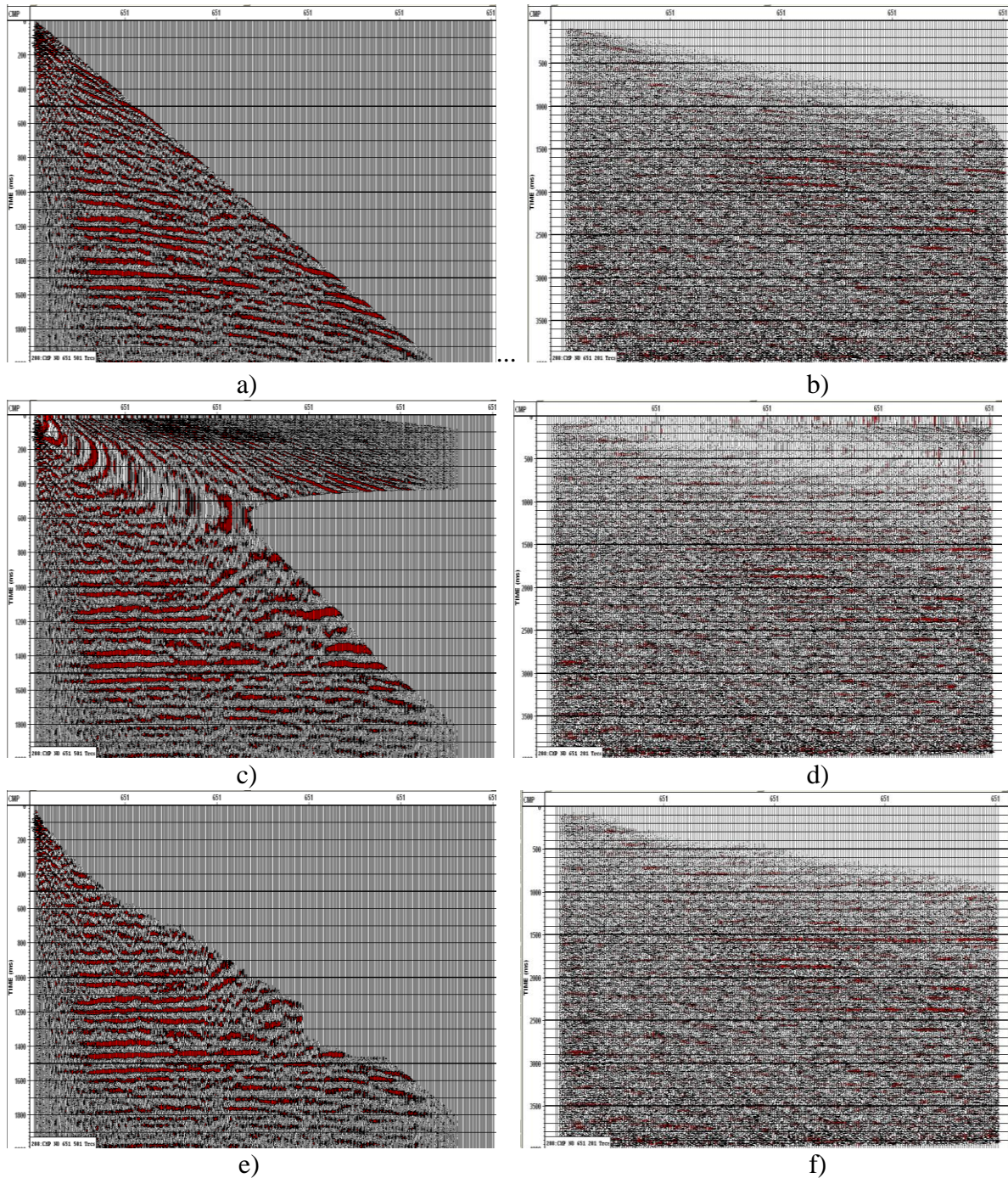
Figure 4.19: CSP (left) and CCSP(right) in the middle of the line (a) and (b) before NMO, c) and d) with NMO applied, e) with 60 % stretch mute applied and f) and with 100% stretch mute applied.

a)   b)
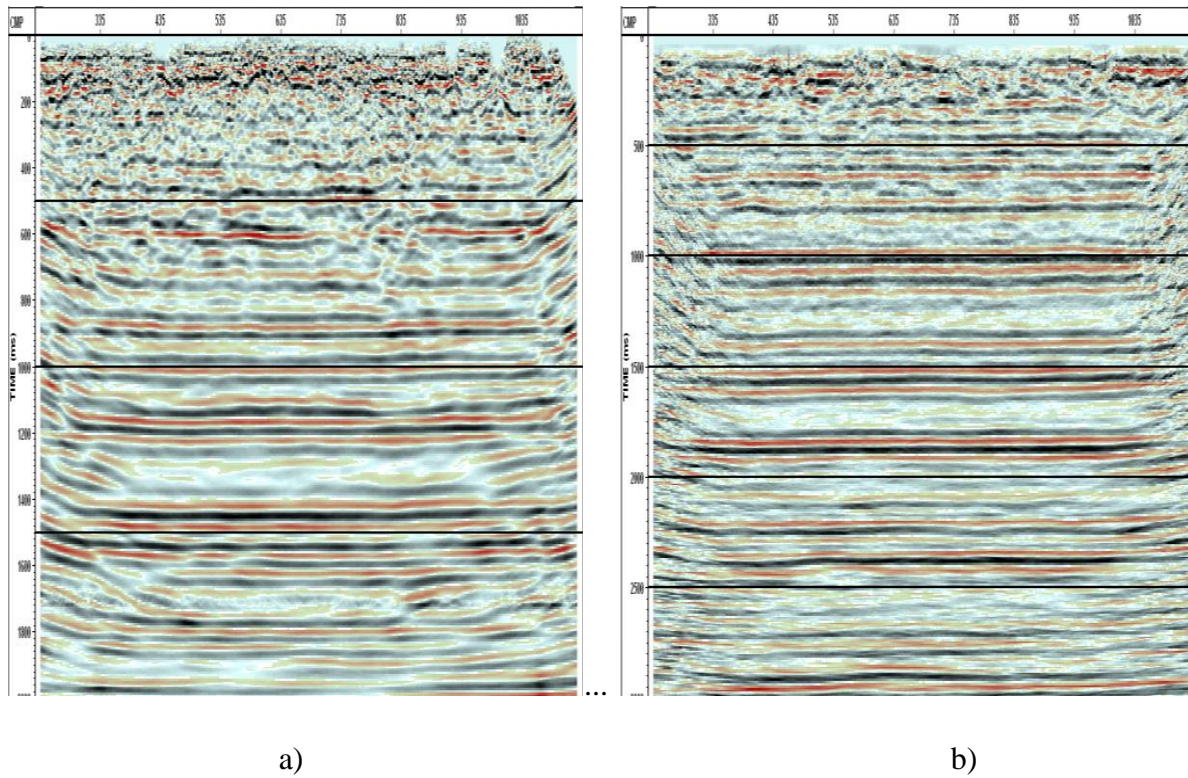
Figure 4.20: a) Final stacked P-P section after EOM b) and final stacked P-S section after EOM.

a)   b)
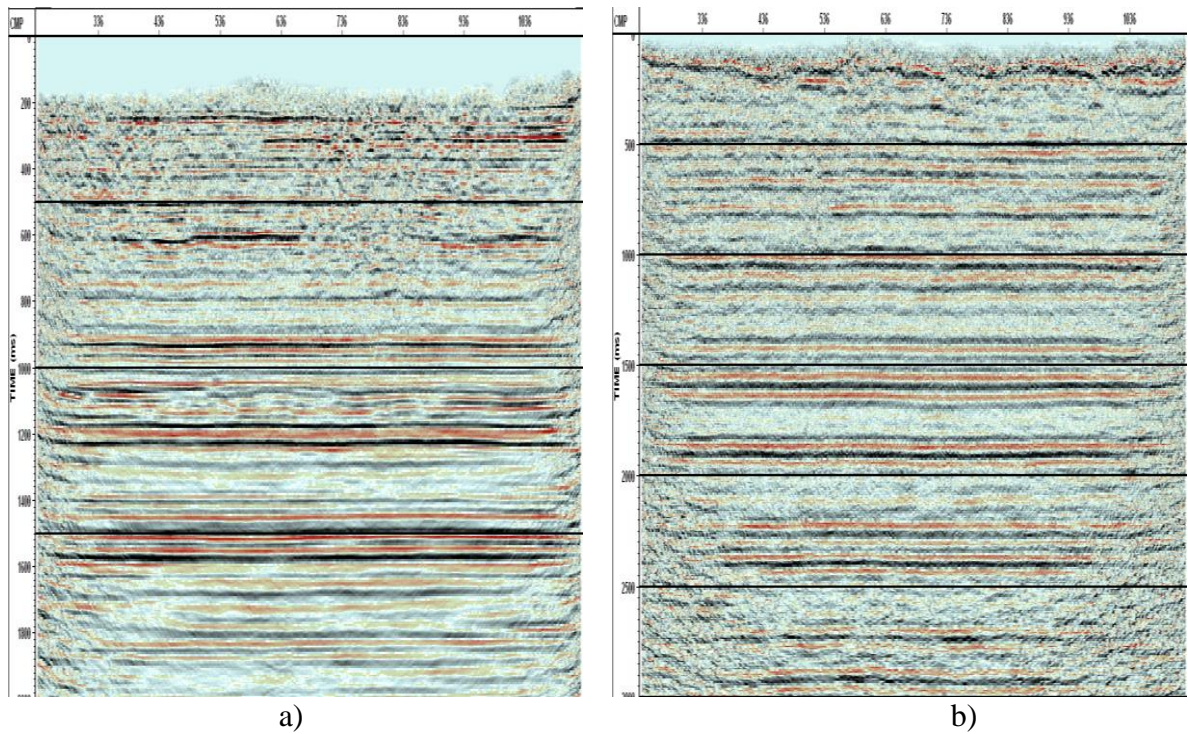
Figure 4.21: Conventional processing, a) P-P poststack time migration, b) P-S poststack time migration section for comparison.
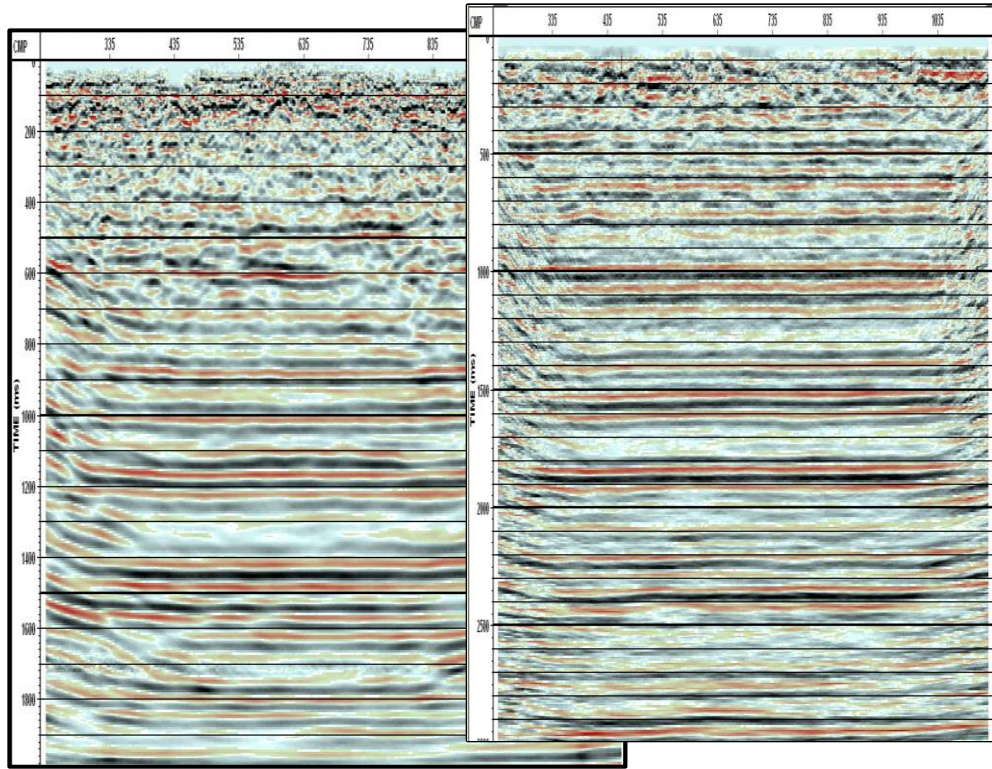
Figure 4.22: Final stacked P-P section after EOM (left) and Final stacked P-S section after EOM scale to P-P time.

a)   b)
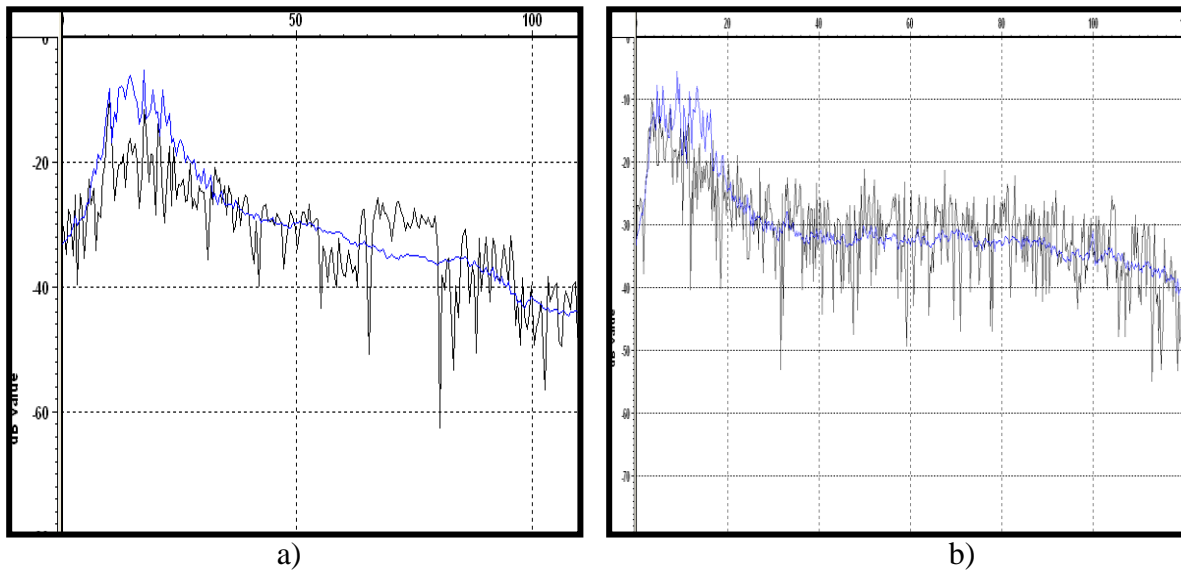
Figure 4.23: Amplitude spectrum a) for final stack P-P section after EOM, and b) for final stack P-S section after EOM

4.2.2 Synthetic dataset

4.2.2.1 Acquisition

The Channel Model was created in 2008 by CREWES (Margrave et al., 2008, Lloyd and Margrave, 2010) as a 3D volume of P and S wave velocity and density. The data are a 3D isotropic elastic model which represents a glauconitic buried channel sequence beneath a stratified overburden. The layer velocities and depth were based on the Bow River in Calgary, Alberta. The channel sequence is 120 m thick. The top of the channel model was placed at 1500 meters in the velocity model. Figure 4.24 shows the gradient model overburden profile taken from Lloyd et al., 2010 and velocities P and S and density were taken from the same figure. The P-, and S-wave velocities and their ratio γ can be seen in Table 4.1
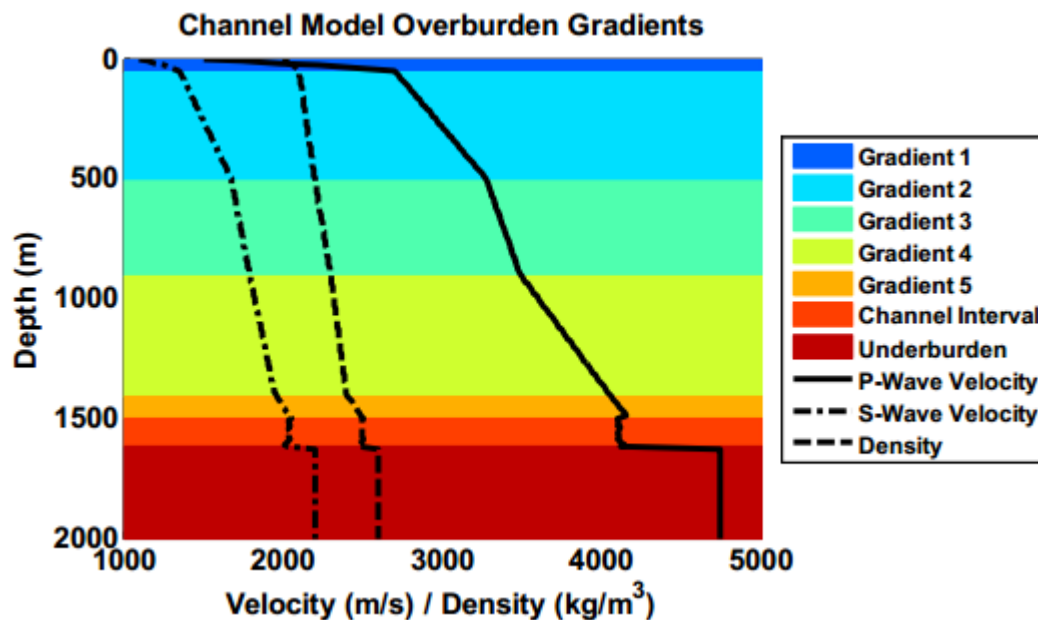
Figure 4.24: Synthetic model showing the gradient overburden profile. Taken from Lloyd and Margrave, 2010.

3D seismic dataset were created using a source wavelet was a 50 Hz Ricker wavelet with a delay time of 0.1 seconds. The data were recorded to a total of 2 sec with a time sample rate of 4 msec. The receivers were placed on a 10 by ten 10 m grid. Lines separation is 100 m. The

sources ran perpendicular to the receiver lines as a 40 m offset. One additional 2D line was calculated in the middle of the survey and with additional shots. This 2D line was extracted from the 3D volume for this thesis for shot spacing of 20 m and receiver spacing of 10 m. The line is assigned a N-S orientation and intersects the channel. Figure 4.25 shows a map view of the V_p/V_s ratio γ in the model at a depth of 1500 m where the location of line is indicated with a dashed black line.

Table 4.1: Velocities for the model

Layer	Vp	Vs	γ
1	1500	500	3
2	2750	1100	2.5
3	3287	1700	1.93
4	3487	1800	1.94
5	4090	2000	2.03
6	4175	2050	2.04
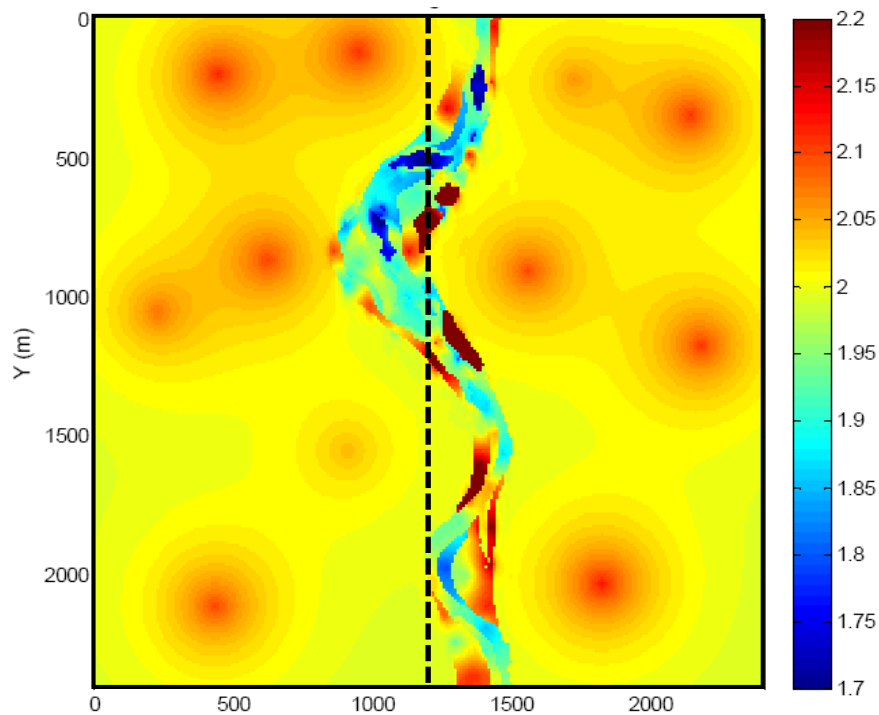
Figure 4.25: V_p/V_s **ratio of the channel model at 1500 m Taken from Lloyd and Margrave, 2010.**

4.2.2.2 Processing

The P-P and P-S radial component dataset were processed at the University of Calgary using a standard processing flow detailed in Figure 4.26, using VISTA software. The final brute stack for P-P data are shown in Figure 4.27 and the Kirchhoff poststack migration is shown in Figure 4.28. The reflector event at about 350 ms can be related to the contrast between layers 2 to 3. The reflector event at about 600 ms can be interpreted with the contrast between layer 3 and 4. According to Lloyd and Margrave, 2010, the top of the channel should appears at 0.9023 sec for P-waves at about 1.4 for P-S, and about 1.8 for S-waves, estimated from time-depth curves. The top of the channel can be identified in these sections at about 1.4 as was predicted by the time-depth curve. P-S and S- wave energy can be identified in these sections at about 1.4 ms and 1.8 ms respectively.

The same EOM processing sequence previously applied for Hussar data were applied to the synthetic dataset. Figure 4.4 shows the processing flow for EOM data.

4.2.2.3 First estimation of V_c Velocities

The following pages describe the result of the process of forming the velocities using the match of traveltime of the velocities method explained in chapter 3. Figure 4.29a shows a comparison of P-wave velocities: RMS, interval velocity and average velocity, $V_{p\text{-}rms,}$ $V_{p\text{-}int}$ and $V_{p\text{-}ave}$ (step 1, using the method 1. Figure 4.29b shows a comparison of RMS velocities for C-wave using method 1, $V_{c\text{-}rms\text{-}1}$ (in blue), and method 2, $V_{c\text{-}rms2}$ (in yellow).

Only for P-S data

Geometry specification

Reversing the polarity of negative offset traces

Bin definition / Header Update

Time shift -100 ms

Mute to kill first breaks

Geometry Spreading compensation

Noise attenuation: FK

Velocity analysis

NMO correction

EOM

Stack

Migration
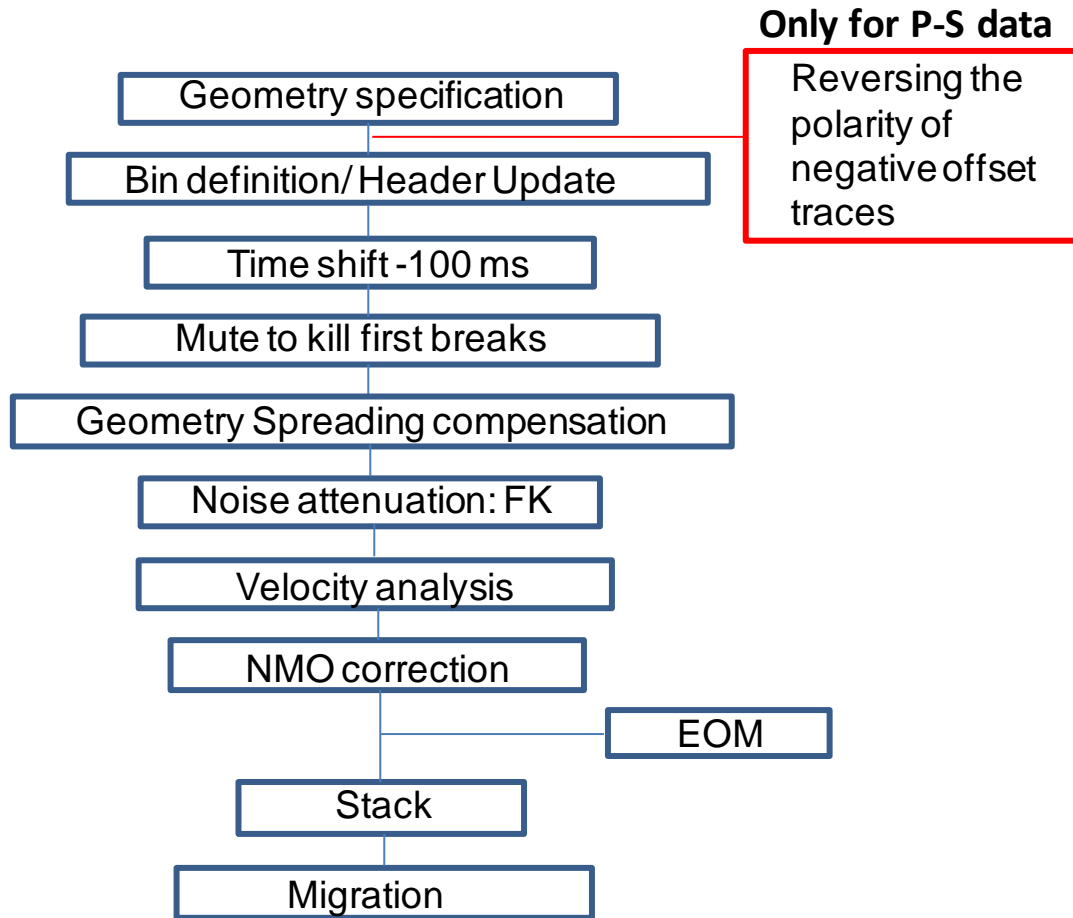
Figure 4.26: Processing flow for the P-P and P-S synthetic datasets.

4.2.2.4 Second estimation of V_c Velocities

Velocity analysis of the LCCSP gathers produced a more accurate velocity estimate of $V_{c\text{-}rms}$ (P) than $V_{c\text{-}rms}$ (G) computed from $V_{p\text{-}rms}$. These velocities are compared in Figure 4.30a which shows the original $V_{p\text{-}rms}$ velocity in blue, $V_{c\text{-}rms}$ (G) computed from $V_{p\text{-}rms}$ in green, and the more accurate $V_{c\text{-}rms}$ (P) in red. It is interesting to note that the two converted wave velocity curves are very close. Figure 4.30b shows a comparison between P-wave interval velocities and converted wave data derived from P-wave velocities using γ=2 and picked from the CSPs in depth.
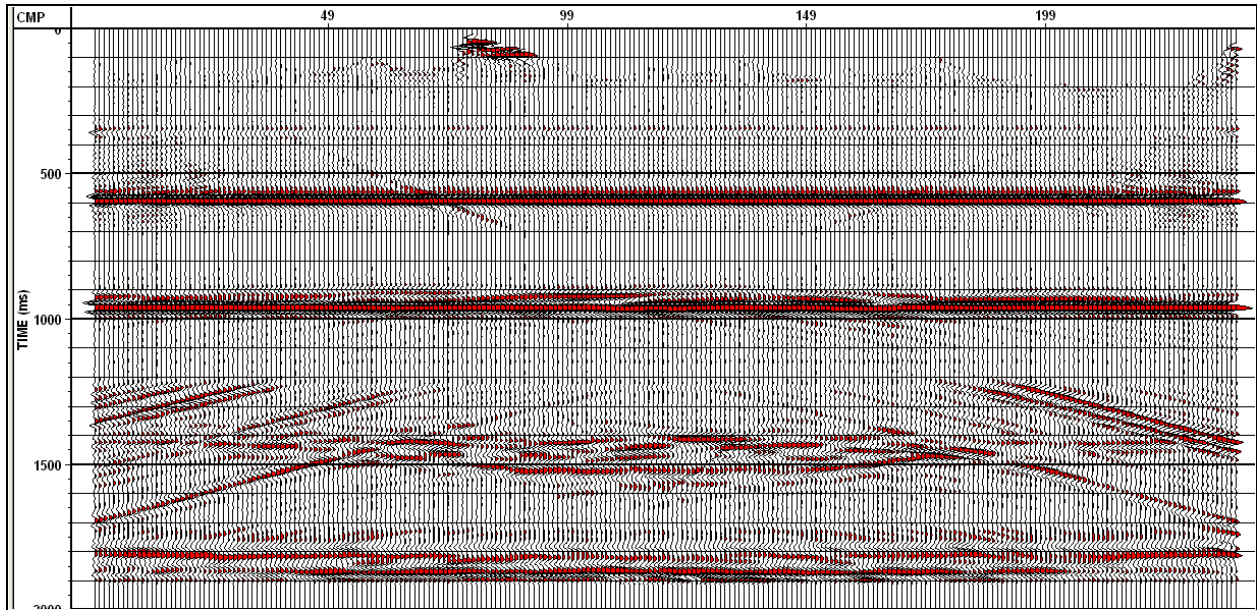
Figure 4.27: P-P stack section.
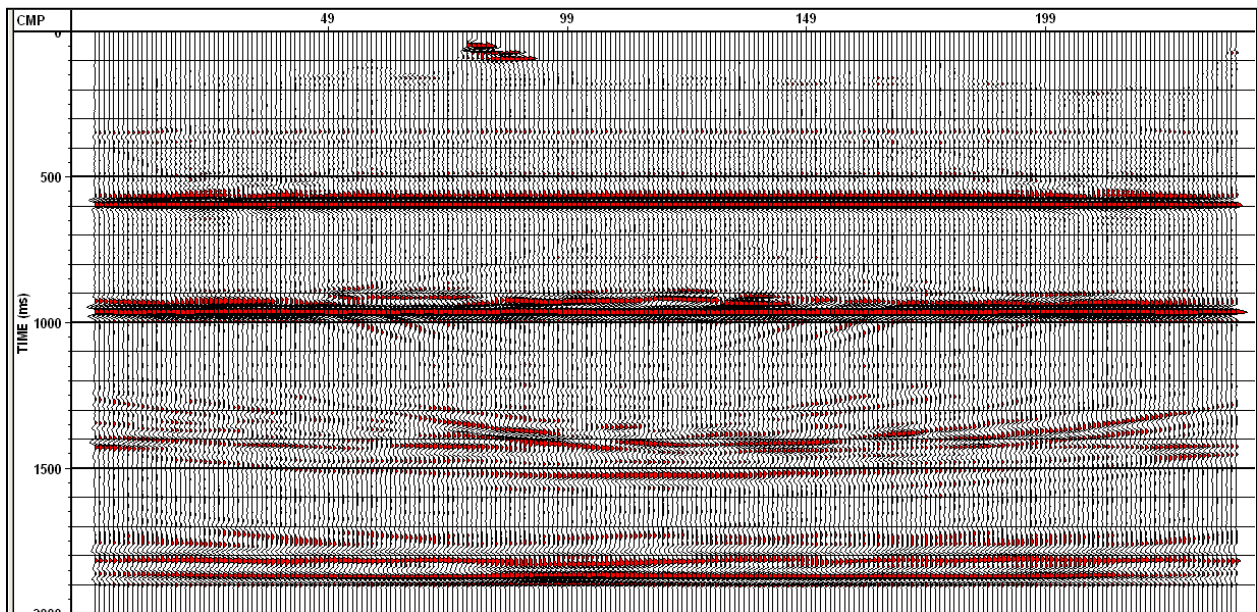
Figure 4.28: P-P Kirchhoff poststack migration section.
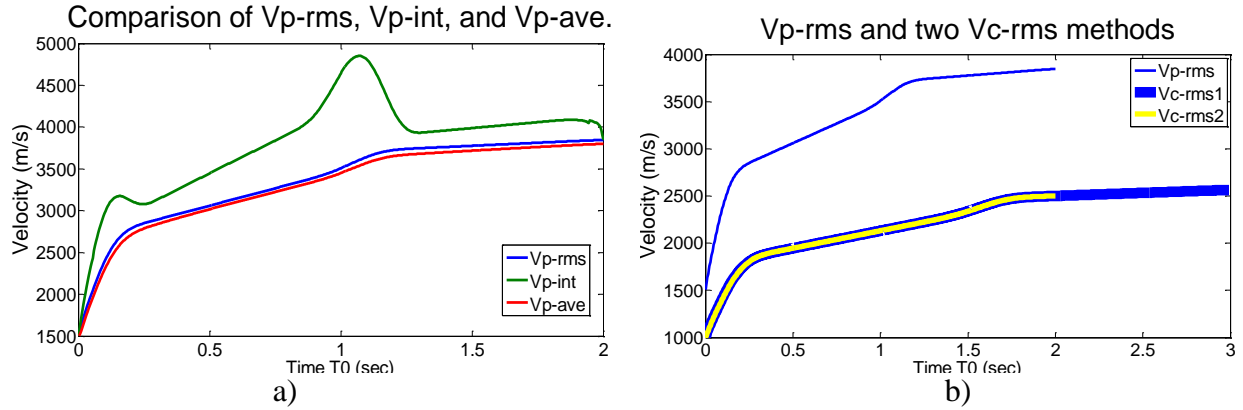
Figure 4.29: a) A comparison of P-wave velocities: RMS, interval velocity and average velocity (b) a comparison of RMS velocities for C-wave using method 1 (in blue), and method 2 (in yellow).
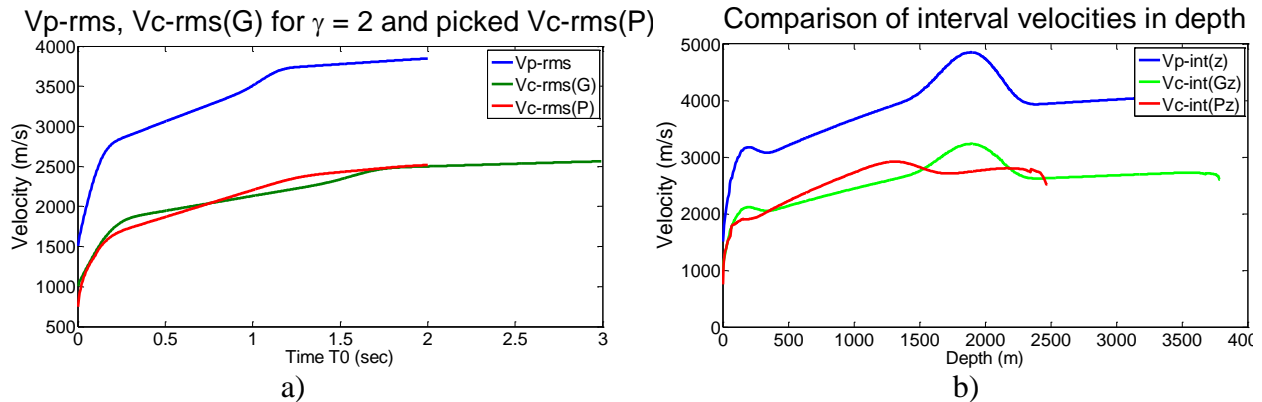
Figure 4.30 a) Comparison of the velocities $V_{p\text{-}rms}$, $V_{c\text{-}rms}$ (G) computed from $V_{p\text{-}rms}$, and a more accurate $V_{c\text{-}rms}$ (P), b) Comparison between P-wave interval velocities $V_{p\text{-}Int}$, and converted wave derived from P velocities using $\gamma=2$ $V_{c\text{-}Int}$ (G), and accurate $V_{c\text{-}Int}$ (P), in depth

After a new and improved $V_{c\text{-}rms}$ is obtained, shear velocities can be estimated. Figure 4.31a shows interval velocities for P-, C-, and S-wave velocities in depth. Figure 4.31b shows the RMS velocities for P-, C-, and S-waves. This last velocity mentioned is shown in t_p time.
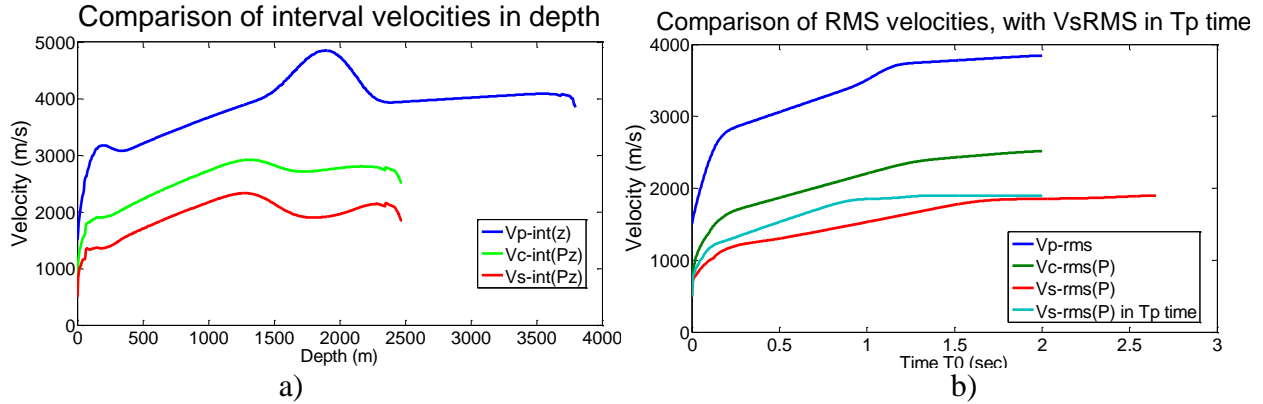
Figure 4.31: a) Comparison between interval velocities for P-wave $V_{p\text{-}Int}$, , C-wave and S-wave in depth, b) Comparison of RMS velocities for P, C and S, $V_{p\text{-}rms}$, $V_{c\text{-}rms,}$, and $V_{s\text{-}rms}$.

After obtaining a more accurate $V_{c\text{-}rms}$, a new estimate of γ can be obtained. Figure 4.32a shows the new estimated γ in time. The new estimate of γ tends to be higher than 3.0 near the surface, and lower than 2.0 deeper in the section, as anticipated. The gamma function derived from $V_{c\text{-}rms}$ from $V_{p\text{-}rms}$ using γ=2, and from picked $V_{c\text{-}rms}$ is now ready to be compared with the γ values shown in Table 4.1, and is shown in Figure 4.32b.
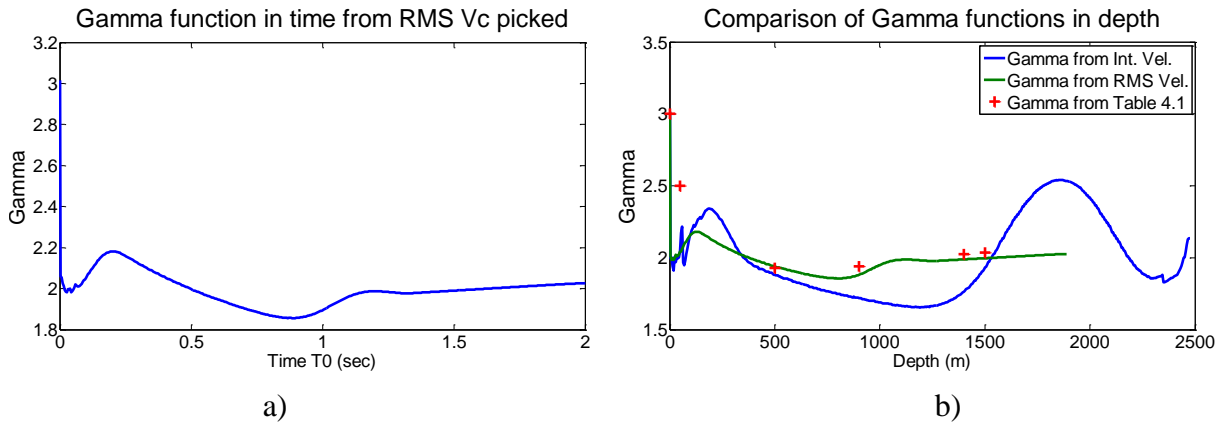
Figure 4.32: a) γ function derived from RMS C velocity picked in time, and b) comparison of the estimated γ function with the interval velocities and RMS velocities and values from Table 4.1.

After the new RMS C velocity has been picked from the LCCSP gathers, normal moveout correction completes the prestack migration. Figure 4.33 shows a final P-S with the complete prestack migration EOM. Figure 4.34 is a zoom of the previous figure where a strong and continues reflector can be interpreted as the top of the channel just below 1400 ms.
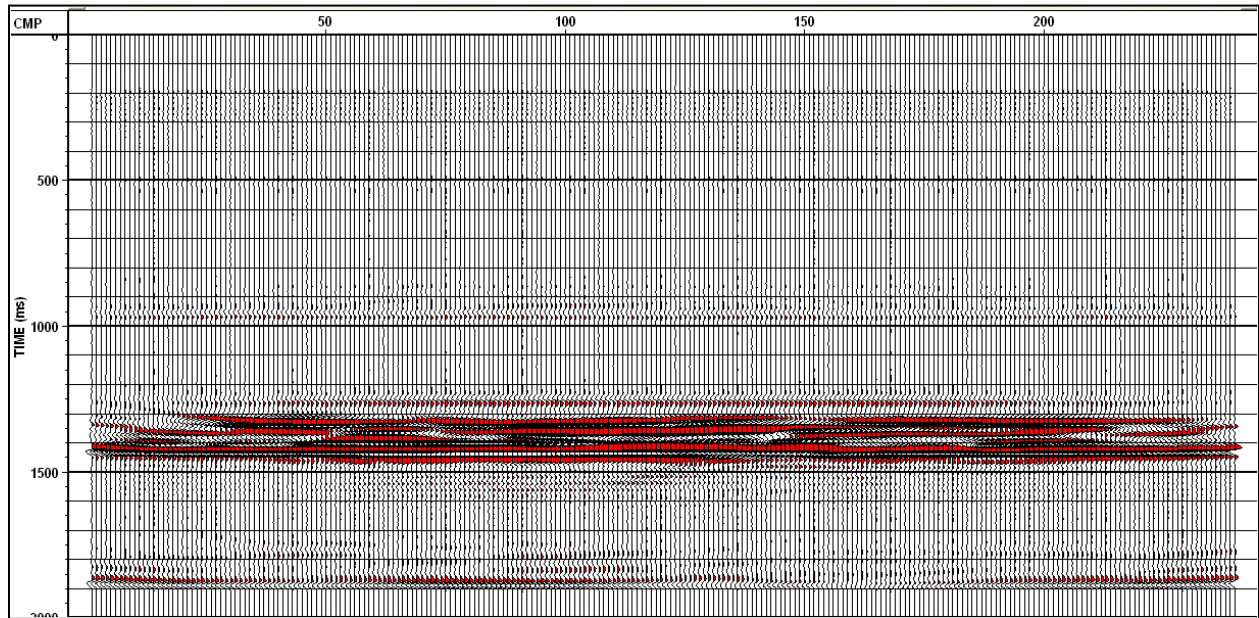
Figure 4.33: P-S EOM stack section.
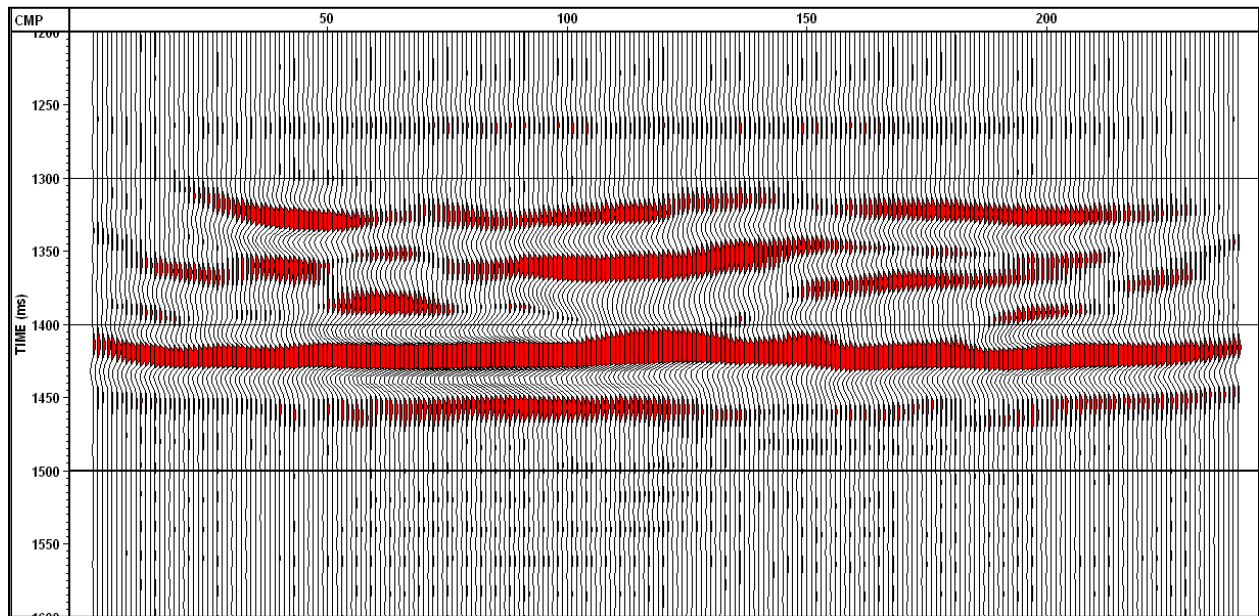
Figure 4.34: P-S EOM stack section from 1200 to 1600 ms

4.2.3 Northeastern British Columbia

4.2.3.1 Acquisition

     This data set was acquired by GeoKinetics for Nexen Inc. in March 2011 as a refraction survey to provide a detailed description of the near-surface P and S-wave velocity-depth structure in Northeast of British Columbia (NEBC).

     The P-wave data were the result of source recorded on the vertical component, and the S-wave data were the result of shear vibrator on one of the horizontal components of the geophones. The Vibroseis sources used produced P-waves and S-waves, and the receivers were Vectorseis SVSM, single 3C geophones. For this project, the shot spacing increment was 10 m, and the receivers spacing increment was 10 m.

     The source information are summarized in Table 4.2

Table 4.2: Sources used in NEBC survey

Source type	interval
Vibroseis, 1 or 2 vibs	10 m
P-wave, 10 or 6 sweep of 10 s, 8-108 linear	
S-wave, 10 sweep of 8 s, 2-256 linear	

4.2.3.2 Processing

The seismic data from NEBC area was preprocessed by Sensor Geophysical, the processing sequence is described by Zuleta, 2011.

4.2.3.3 EOM results

     The following figure (Figure 4.35) is an example of traces from narrow offset gathers, equally spaced across the line. The gathers were formed with x_{max} = 100 m, for $\gamma = 2$, and $\gamma = 2.5$. The panels improved focussing at different times due to the variation of γ in time.

Figure 4.36a shows a comparison of the interval velocities for P-wave $V_{p\text{-}Int}$, C-wave $V_{c\text{-}Int}$ and S-wave $V_{s\text{-}Int}$ in time, (b) shows comparison of the RMS velocities $V_{p\text{-}rms}$, $V_{c\text{-}rms}$, and $V_{s\text{-}rms}$ for P-, C, and S-wave in time. The interval velocities derived from picked velocities are compared with velocities measurements from a well log, as illustrated in Figure 4.36c for P-P data, and (d) for P-S data. Using these velocities, a new γ function can be derivate. Figure 4.36e shows a comparison of the gamma function with the assumed initial value of γ=2, γ derived from the new RMS C velocities picked, and from the well logs.

The full EO method was applied to all CCSP gathers using the best velocity V_c picked from semblance plot and NMO correction applying stretch mute of 90 %. Figure 4.37a shows a CCSP gather around in the middle of the line, with NMO correction in (b) and after applying NMO correction with stretch mute of 90 % in (c). Figure 4.38a is the final EOM stack for P-P dataset. The NMO correction was applied using a stretch mute of 10 % for this dataset. Figure 4.38b is the same final stack compressed spatially. Figure 4.39a is the final EOM stack for P-S dataset (b) is the same stack compressed spatially. A channel can be identified in the section around CMP 1700 to CMP 2000 below 200 msec in the P-P section and below 400 msec in the P-S section.
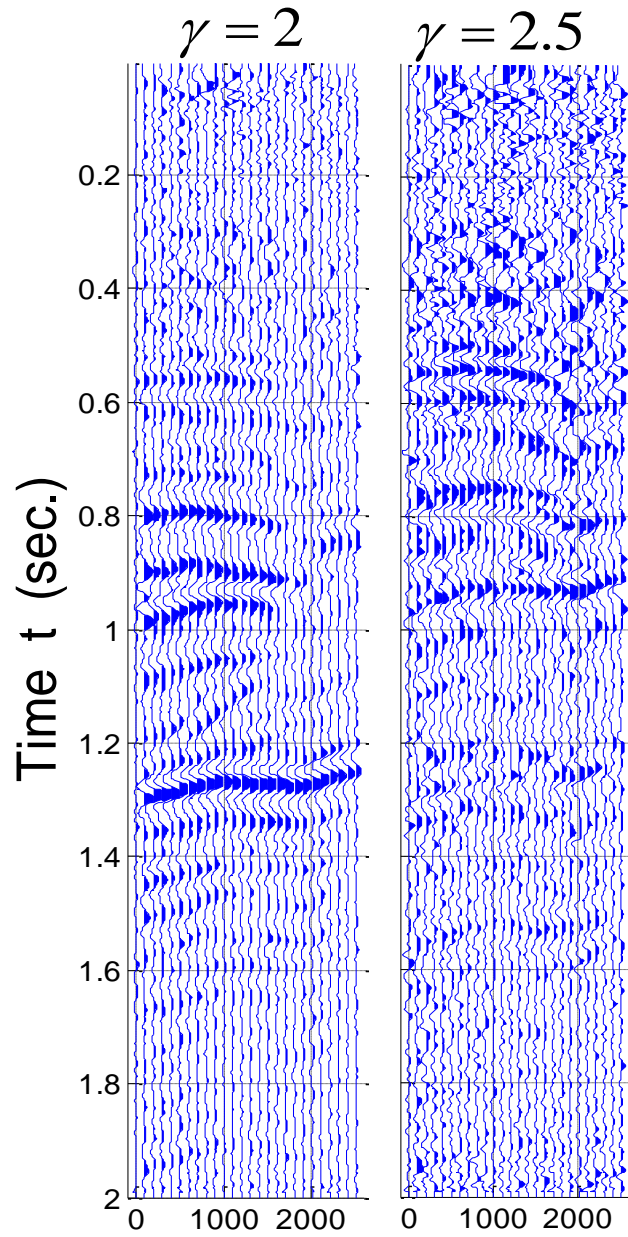
Figure 4.35: Two narrow offset gathers formed with x_{max} = 100 m, equally spaced across the line using different values of γ: γ=2 (left) and γ=2.5 (right)
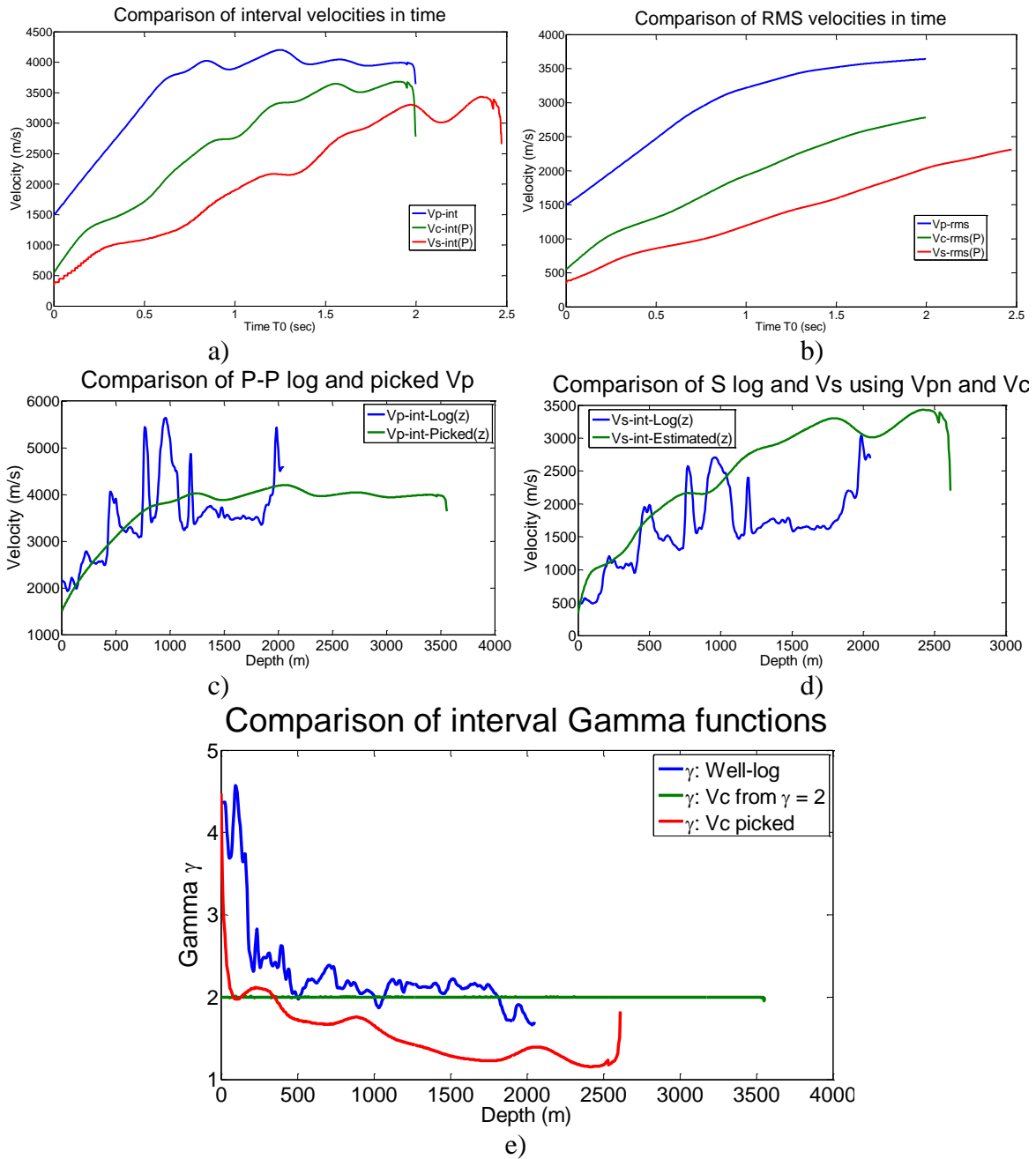
Figure 4.36: : a) Comparison of the interval velocities for P-wave $V_{p\text{-}Int}$, C-wave $V_{c\text{-}Int}$ and S-wave $V_{s\text{-}Int}$ in time, b) comparison of the RMS velocities $V_{p\text{-}rms}$, $V_{c\text{-}rms}$, and $V_{s\text{-}rms}$ for P-, C, and S-wave in time. Comparison between interval velocities from well logs and estimated values with c) Vp and, d) Vs, e) comparison of estimated γ functions derived from the well logs, the assumed initial value of $\gamma=2$, and γ derived from picked P and C velocities.
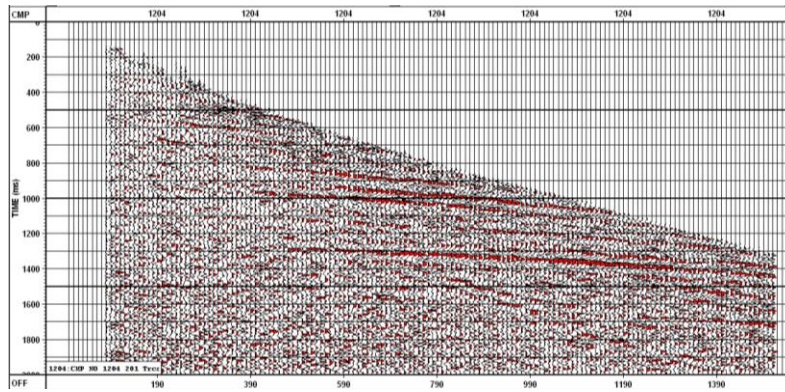
(a)
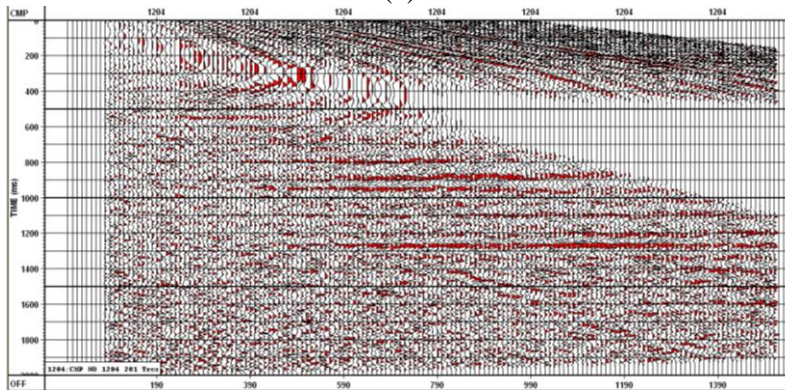
(b)
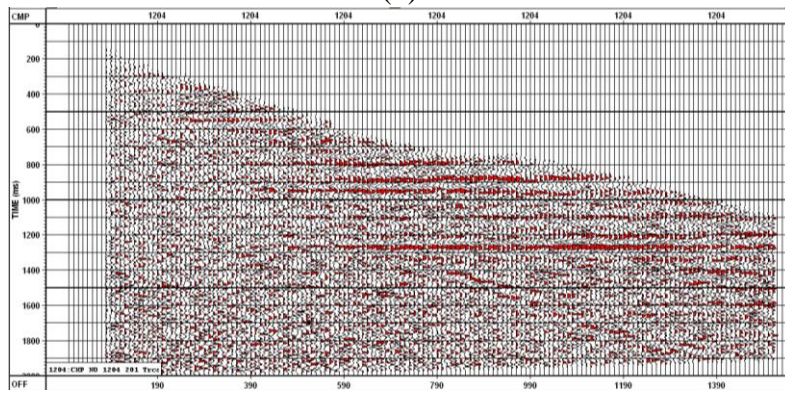
(c)

Figure 4.37: CCSP in the middle of the line formed by Full EO method (a) before NMO correction, b) after NMO correction, and c) and with 90% stretch mute applied.
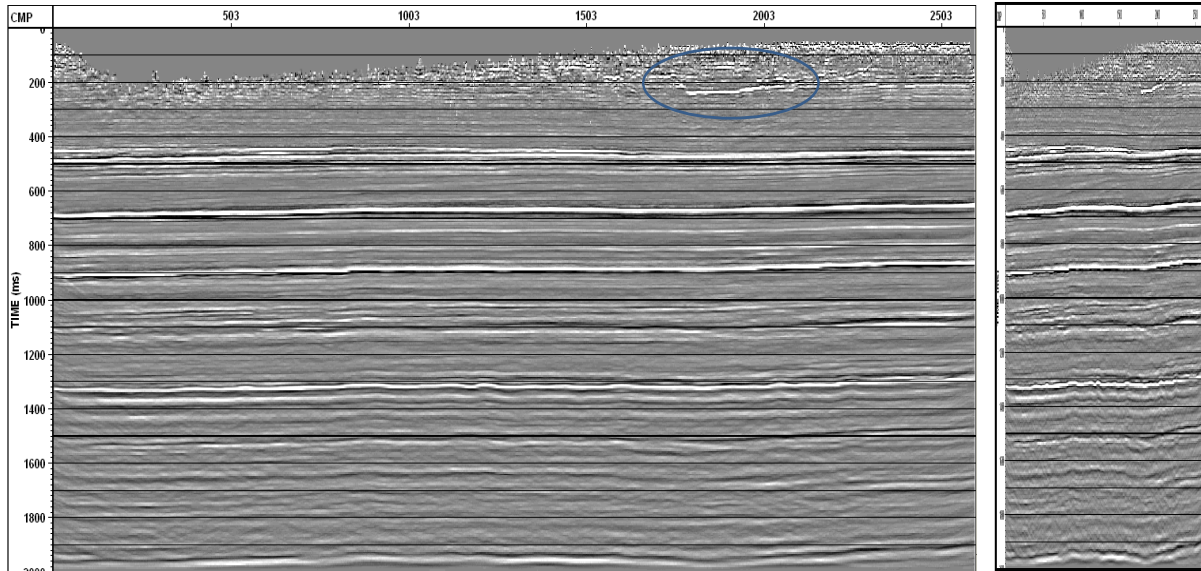
a)   b)

Figure 4.38: P-P EOM stack section, a) normal scale, and b) compressed spatially to identify the structure of the channel.
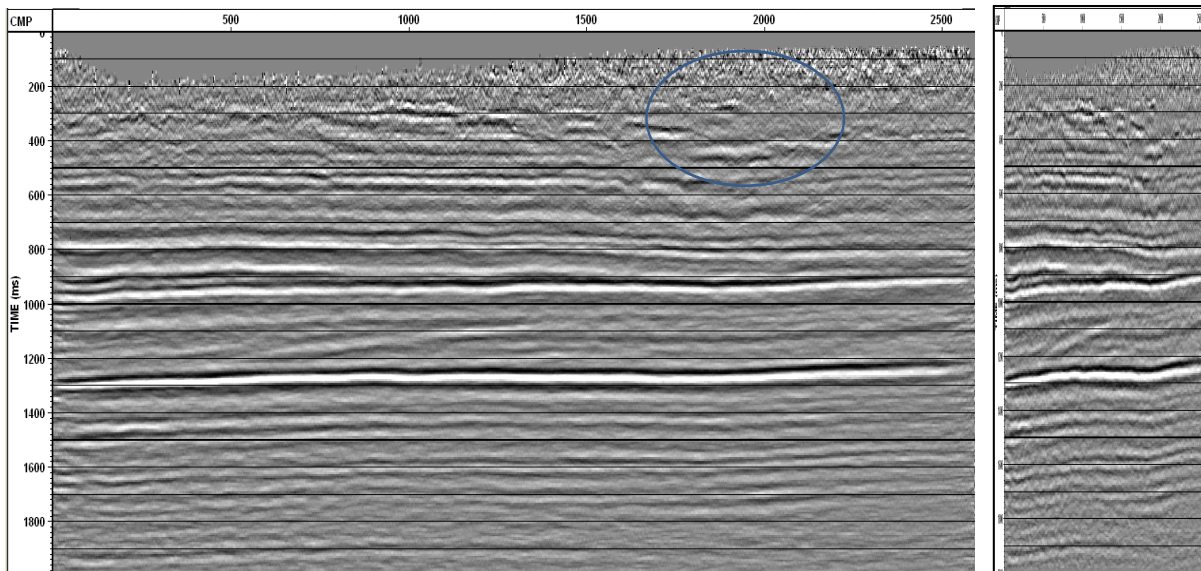
a)   b)

Figure 4.39 P-S EOM stack section, a) normal scale, and b) compressed spatially to identify the structure of the channel.

Figure 4.40 shows an amplitude spectrum graph for unfiltered final stack after EOM for

(a) P-P data, and (b) P-S data.

85

a)   b)
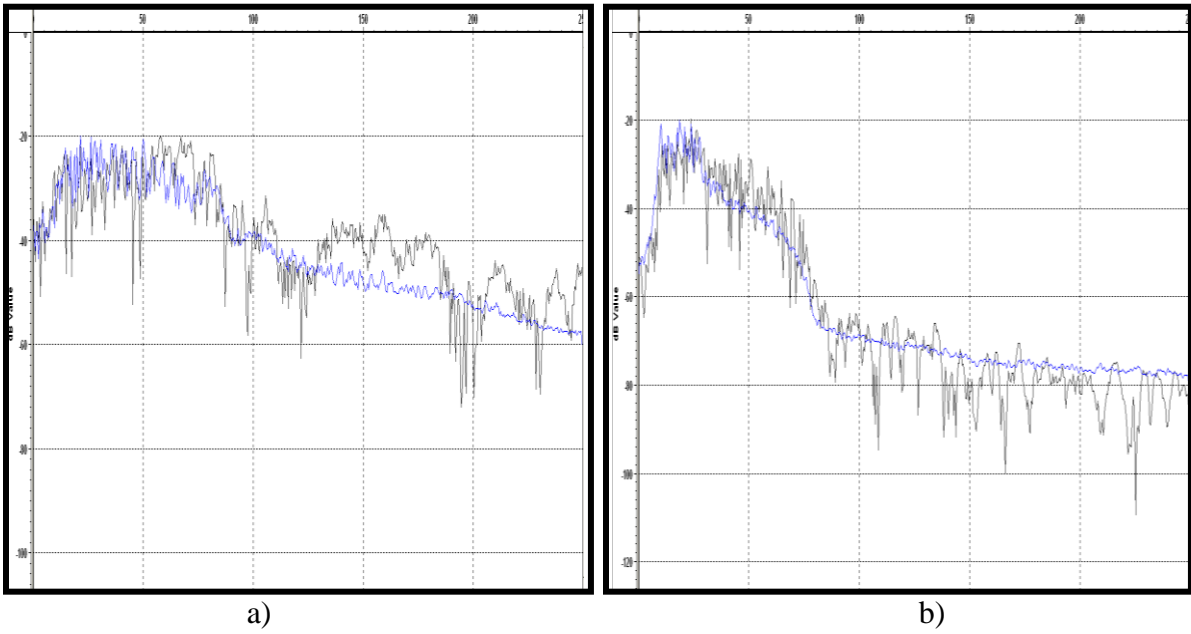
Figure 4.40: Amplitude spectrum a) for final stack P-P section after EOM, and b) for final stack P-S section after EOM

Chapter Five: **Conclusions and Recommendations**

Converted wave data are created using two velocities, V_p and V_s, for the incident and reflected raypaths. During different parts of the processing in this project, these two velocities were then combined into one velocity, V_c. This velocity was used first to form limited converted CSP (LCCSP) gathers that then provided an improved V_c that produces an initial estimate of V_s. V_p and V_s are then used to form complete equivalent offset gathers. These gathers were then analysed to further improve V_c to provide a better moveout correction. Stacking completed the prestack migration.

Converted wave prestack migration by equivalent offset is based on the principles of Kirchhoff migration and uses equivalent offsets to form limited converted CSP (LCCSP) gathers. These gathers are formed using a limited range of displacements between the imaging location and the common midpoint. The method does not require the use of ACCP binning, a major weakness of conventional processing methods.

An acceptable time error may be defined to form a LCCSP gather by assuming a constant converted wave velocity V_c. The intended application is to rapidly form an LCCSP gather to provide an initial estimate of the RMS velocity for converted wave prestack migration using the equivalent offset method.

A reasonably accurate estimate of converted wave velocities, V_c is required to form CCSP gathers as part of the Equivalent Offset Migration of converted waves. This velocity was first estimated from RMS velocities V_p and an initial constant value for the V_p/V_s ratio γ. A refined estimate was then made from narrow displacement gathers. The converted wave velocities were then used to make an initial estimate of the shear wave velocities V_s. These velocities were then used with the V_p velocities for prestack migration.

87

The common converted wave scatterpoint (CCSP) gathers were then used to create accurate estimates of V_c in order to improve V_s and γ.

The CSP gathers were formed using only the geometry of the trace, namely the source and receiver locations relative to the location at which the gather is formed.

The quality of the method is demonstrated for the cases of one synthetic dataset and two real datasets. The results show superior imaging when compared with alternative migration algorithms.

The estimated velocities of V_s are compared with velocities obtained from well-logs and compare favorably.

Recommendations

1. The improved imaging afforded by EOM may allow projects to be designed more efficiently, requiring fewer sources and/or receivers.

2. The EOM method employed in this thesis required data to be processed to a horizontal datum. Improved imaging may occur if the algorithm is modified to migrate from surface.

3. EOM has also been used to estimate statics in P-P processing. It may provide a better estimate of both the source and receiver statics.

4. Consideration of anisotropy for both the P and S velocities may also provide more accurate ties between well and estimated velocities. These more accurate estimates may aid in seismic inversion.

5. The resolution of the data may be improved with a deconvolution after migration.

6. The 2D seismic data set may be re-migrated to image oblique reflectors.

References

Acham, P. A., 1971, The Mannville Group (Lower Cretaceous) of the Hussar area, southern Alberta: M.S. thesis, University of Alberta, Alberta, Canada, 152 p.

Allan, J. A., and Rutherford, R. L., 1934, Geology of Central Alberta: Research Council of Alberta, University of Alberta, Report No. 30, 1-48

Bancroft, J. C., 2012, A Practical Understanding of Post and Prestack Migration, Course Notes, SEG Press Book.

Bancroft, J. C., Geiger, H. D., Foltinek, D. S. and Wang, S., 1994, Prestack migration by equivalent offset and CSP gathers: CREWES Research Report, 6, 27.1-18.

Bancroft, J. C, and Wang, S., 1994, Converted-wave prestack migration and velocity analysis by equivalent offsets and CCP gathers: CREWES Research Report, 6, 28.1-7

Bancroft, J. C, Geiger, H. D., Wang, S., and Foltinek, D. S., 1995, Prestack migration by equivalent offset and CSP gathers: an update: CREWES Research Report, 7, 23.1-29.

Bancroft, J. C, Geiger, H. D., Margrave, G .F, Wang, S., and Foltinek, D. S., 1996, Prestack migration by equivalent offset and CSP gathers: CREWES Research Report, 8, 29.1-19.

Bancroft, J. C., Geiger, H. D., and Margrave, G. F., 1998, The equivalent offset method of prestack time migration: Geophysics, 63, no.6, 2042-2053.

British Columbia Ministry of Energy and Mines, 2009, Summary of shale gas activity in Northeast British Columbia 2008/09. Petroleum Geology Open File 2009-1.

Brown, R. J., Stewart, R. R., Gaiser, J. E., and Lawton, D. C., 2000, An acquisition polarity standard for multicomponent seismic data: CREWES Research Report, 12, 7.1-18

Cary, P. W., and Eaton, D. W. S., 1993, A simple method for resolving large converted-wave (P-SV) statics: Geophysics, 58, no. 3, 429-433

Castagna, J. P., and Backus, M. M., 1993, Eds., Offset-dependent reflectivity – Theory and practice of AVO analysis, Society Exploration Geophysics, 135-171

Castagna, J. P., Batzle, M. L., and Eastwood, R. L., 1985, Relationships between compressional-wave and shear-wave velocities in clastic silicate rocks: Geophysics, 50, no. 4, 571-581

Castagna, J. P., Batzle, M. L., and Kan, T. K., 1993, Rock physics: the link between rock properties and AVO response in Castagna, J. P., and Backus, M. M., Eds., Offset-dependent reflectivity – Theory and practice of AVO analysis, Society Exploration Geophysics, 135-171

Claerbout, J. F., 1984, Imaging the Earth's Interior: Blackwell Scientific.

Denelle, E., Dezard, Y., and Raoult, J. J., 1986, 2-D prestack depth migration in the (S-G-W) domain: 56th Annual International meeting, SEG, Expanded Abstracts 327-330

Deregowski, S. M., 1990, Common-offset migration and velocity analysis: First Break, 8, no. 7, 225-234

Diet, J. P., Audebert, F., Huard, I., Lanfranchi, P., and Zhang, X., 1993, Velocity analysis with prestack time migration using the S-G method: A unified approach: 63rd Annual International Meeting, SEG, Expanded Abstract, 957-960

Domenico, S. N., 1977, Elastic properties of unconsolidated sand reservoirs: Geophysics 42, no. 7, 1339-1368

Ehinger, A., Lailley, P., Marfurt, K. J., 1996, Green's function implementation of common-offset, wave-equation migration, 1996: Geophysics, 61, no. 6, 1812-1821

ERCB, 2009, Table of formations, Alberta

Ferguson, R.F., 1996, P-S Seismic Inversion: Modeling, Processing and Field Examples: M.S. thesis, University of Calgary, Alberta, Canada, 112 p.

Ferri, F., Hickin, A., and Huntley, D. H., 2011, Besa River Formation, western Liard Basin, British Columbia (NTS 094N): Geochemistry and regional correlations, BC Ministry of Energy and Mines. Geocience report.

Fromm, G., Krey, T., and Wiest, B., 1985, Static and dynamic corrections, in Seismic shear waves: Handbook of geophysical exploration, 15a, 191-225, Geophysical Press.

Gedco, 2011, Vista, 2D/3D Seismic data processing, 3component tutorial manual, Version 11.0

Glaister, R . P., 1959. Lower Cretaceous of southern Alberta and adjoining areas. AAPG Bulletin, v. 43, No. 3, p.590-640

Gregory, A. R., 1976, Dynamic elastic rock properties: key to pore fluid identity: Oil and Gas Journal, 74, 130-138

Guirigay, T. A., and Bancroft, J. C., 2010, Converted wave processing in the EOM domain: CREWES Research Report, 22, 23.1-24

Han, D., Nur, A., and Morgan, D., 1986, Effect of porosity and clay content on wave velocities in sandstones: Geophysics, 51, no. 11, 2093-2107

Hickin, A., Kerr, B., Turner, D. G., and Barchyn, T. E., 2008, Mapping quaternary paleovalleys and drift thickness using petrophysical logs, northeast British Columbia, Fontas map sheet, NTS 94I Canadian Journal of Earth Science, 45, 577-591

Ion, D., and Galbraith, M., 2011, A Practical Approach for Estimating Receiver Statics in 2D/3C Seismic Data Processing, Abstract for Recovery, CSEG Convention, 1-4

Isaac, J. H., and Margrave, G. F., 2011, Hurrah for Hussar! Comparison of stacked data: CREWES Research Report, 23, 55.1-23

Isaac, J. H., 1996, Seismic methods for heavy oil reservoir monitoring, PhD. thesis, University of Calgary, Alberta, Canada, 224 p

Kearey, P. and Brooks, M., 1999, An introduction to Geophysical Exploration, Blackwell Science, Second edition

Lee, W. B., and Zhang, L., 1992, Residual shot profile migration: Geophysics, 57, no. 6, 815-822

Levson, V., 2008, Geology of northeast British Columbia and northwest Alberta: diamonds, shallow gas, gravel, and glaciers, Canadian Journal of Earth Science, 45, no. 5, 509-512

Lindsey, J. P., and Herman, A., 1970, Digital migration, Oil and Gas Journal, 38, 112-115

Lloyd, H. J. E., and Margrave, G. F., 2010, CREWES channel model: Description, acquisition, interpretation and data release: CREWES Research Report, 22, 57.1-13

Lumley, D. E., 1989, A generalized Kirchhoff-WKBJ depth migration theory for multi-offset seismic reflection data: reflectivity model constructed by wavefield imaging and amplitude estimation: M. Sc. Thesis, University of British Columbia.

Lumley, D. E. And Claerbout, J. F., 1989, Anti-aliased Kirchhoff 3-D migration: a salt intrusion example: SEG 3-D Seismic Workshop, 115-123

Lynch, T. K., 2002, High resolution sequence stratigraphy and a study of Reservoir controls of the glauconitic sandstone member in the Cessford Mannville C Pool, Southeastern Alberta: M. S. thesis, University of Calgary, Alberta, Canada, 289 p.

Margrave, G. F., Taylor S., and Cooper, J. K., 2008, Toward realistic 3D elastic models of Canada channel and reef structures: CREWES Research Report, 20, 39.1-25

Margrave, G. F., Mewhort, L., Phillips, T., Hall, M., Bertram, M. B., Lawton, D. C., Innanen, K., Hall, K., and Bertram, K., 2011, The Hussar low-frequency experiment: CREWES Research Report, 23, 78.1-24

MatLab version 7.11.0.584. Natick, Massachusetts: The MathWorks Inc., 2010.

McPhail, S., Walsh, W., Lee, C., and Monahan, P. A., 2008, Shale Units of the Horn River Formation, Horn River and Cordova Embayment, Northeast British Columbia, British Columbia Ministry of Energy and Mines, Petroleum Geology Open File 2008-1

Murphy, W. F. III, 1994, Seismic to ultrasonic velocity drift: intrinsic absorption and dispersion in crystalline rock: Geophysics. Res. Let., 11, 1239-1242

Ng, M., 1984, Prestack migration of shot record using phase shift plus interpolation: Canadian Journal of Exploration Geophysics, v. 30, no. 1, 11-27

Nur, A., and Simmons, G., 1969, The effect of saturation on velocity in low porosity rocks: Earth Planet Sci. Let., 7, 183-193

Okaro, P. I., 2001, High resolution sequence stratigraphy, sedimentology, petrology, and reservoir potentials of the Glauconite Member in the Westerose and adjacent fields, Alberta, Canada: Ph. D. thesis, University of Calgary, Alberta, Canada, 352 p.

Pickett, G. R., 1963, Acoustic character logs and their application in formation evaluation: Journal Petroleum Technology, 659-667

ProMAX version 5000.0.3.0, Landmark Graphics Corporation, 2008

Reshef, M., and Kosloff, D., 1986, Migration of common-shot gathers: Geophysics, 51, no. 2, 324-331

Rockwell, D. W., 1971, Migration stack aids interpretation: Oil and Gas Journal, 69, 202-218

Sattlegger, J. W., Stiller, P.K., Echterhoff, J. A., and Hentschke, M. K., 1980, Common offset plane migration (COPMIG): Geophysical Prospecting, 28, 859-871

Simmons, J. L., and Backus M. M., 1999, Radial-Transverse (SV-SH) coordinates for 9-C 3-D seismic reflection data analysis. SEG Expanded Abstracts 18, 728-731

Stewart, R. R, 1994, The present and promise of P-S seismic exploration: CREWES Research Report, 6, 1.1-31

Stewart, R.R., Gaiser, J.E., Brown R.J., and Lawton, D. C., 2002, Tutorial: Converted-wave seismic exploration: Methods, Geophysics, 67, no, 5, 1348-1363.

Stewart, R.R., Gaiser, J.E., Brown R.J., and Lawton, D. C., 2003, Tutorial: Converted-wave seismic exploration: Applications, Geophysics, 68, no, 1, 40-57.

Schultz, P. S. and Sherwood, J. W. C, 1980, Depth migration before stack: Geophysics, 45, no. 3, 376-393

Slotboom, R. T., 1990, Converted wave (P-SV) moveout estimation: Presented at the 60th Annual International Meeting, Society Exploration Geophysics, Expanded Abstracts, 1104-1106

Tanner, M. T., and Koehle, F., 1969, Velocity spectra – Digital computer derivation and applications of velocity functions: Geophysics, 34, no. 6, 859-881

Tatham R. H., and McCormack, M. D., 1998, Multicomponent seismology in petroleum exploration: Investigations in geophysics series – Volume 6, SEG publications

Tatham, R. H., and Stoffa, P. L., 1976, Vp/Vs -A potential hydrocarbon indicator: Geophysics, 41, no. 5, 837-849.

Tatham, R.H., 1982, Vp/Vs and lithology: Geophysics, 47, no. 3, 336-344.

Tessmer, G., and. Behle, A., 1988, Common reflection point data-stacking technique for converted waves: Geophysics Prospecting, 36, 671-688

Timur, A., 1977, Temperature dependence of compressional and shear wave velocities in rocks: Geophysics, 42, no. 5, 950-956

Tosaya, C. A., Nur, A. M., and Daprat, G., 1984, Monitoring of thermal EOR fronts by seismic methods: Proceedings 1984 lf. Reg. Mgt, Soc Petro. Eng. SPE No. 12744

Van der Schoot, A., Romijn, R., Larson, D.E., and Berkhout, A. J. 1989, Prestack migration by shot record inversion and common depth point stacking: a case study: First Break, 7, no. 7, 293-304

VISTA version 11.036.2538. Calgary, Alberta, Canada: Gedco, 2011

Wang, S., Bancroft, J. C, Lawton, D. C., and Foltinek, D. S.,, 1995, Converted-wave (P-S) prestack migration and migration velocity analysis: CREWES Research Report, 7, 27.1-22.

Wang, S., 1997, Three-component and three-dimensional seismic imaging: M.S. thesis, University of Calgary, Alberta, Canada, 83 p

Wang, Z., and Nur, A., 1987, Wave velocities in hydrocarbon saturated rocks: 57th Annual International Meting., Society Exploration Geophysics, Expanded Abstracts, 1-5

Yilmaz, O, and Claerbout, J. F., 1980, Prestack partial migration: Geophysics, 45, no. 12, 1753-1779

Zuleta, L., and Lawton, D. C., 2011, P-wave and S-wave near-surface characterization in Northeast British Columbia (NEBC): CREWES Research Report, 23, 102.1-25

Zuleta, L., 2012, Near-surface characterization and Vp/Vs analysis of a shale gas basin: M.S. thesis, University of Calgary, Alberta, Canada, 120 p

APPENDIX A: DERIVATION HE AS Z TENDS TO ZERO

Starting with the definition for the equivalent offset equation (3-15), we have

$$h_e^2 = \frac{V_c^2}{4} \left(\frac{1}{V_p} \sqrt{z_0^2 + h_s^2} + \frac{1}{V_s} \sqrt{z_0^2 + h_r^2} \right)^2 - z_0^2. \tag{A-1}$$

When z_0 tends to zero, $\tilde{h}_e^2$

$$\tilde{h}_e^2 = \frac{V_c^2}{4} \left(\frac{h_s}{V_p} + \frac{h_r}{V_s} \right)^2, \tag{A-2}$$

if γ is defined as

$$\gamma = \frac{V_p}{V_s}, \tag{A-3}$$

and V_c is defined as

$$V_c = \frac{2\,V_p V_s}{V_p + V_s}, \tag{A-3}$$

or

$$V_c = \frac{2\,V_p}{1+\gamma}, \tag{A-4}$$

and V_s is defined as

$$V_s = \frac{V_p}{\gamma}, \tag{A-5}$$

then

$$\tilde{h}_e^2 = \frac{V_p^2}{(1+\gamma)^2} \left(\frac{h_s}{V_p} + \frac{\gamma\,h_r}{V_p} \right)^2, \tag{A-6}$$

therefore

$$\tilde{h}_e^2 = \frac{1}{(1+\gamma)^2} \, (h_s + \gamma h_r)^2, \tag{A-7}$$

and finally

$$\tilde{h}_{e_{z_0 \to 0}} = \frac{(h_s + \gamma h_r)}{1+\gamma}. \tag{A-8}$$

APPENDIX B: DERIVATION HE AS Z TENDS TO INFINITE

Starting with the definition for the equivalent offset equation (4-15), we have

$$h_e^2 = \frac{V_c^2}{4}\left(\frac{1}{V_p}\sqrt{z_0^2 + h_s^2} + \frac{1}{V_s}\sqrt{z_0^2 + h_r^2}\right)^2 - z_0^2. \qquad \text{(B-1)}$$

with

$$V_c = \frac{2\,V_p}{1+\gamma}, \qquad \text{(B-2)}$$

and V_s is defined as

$$V_s = \frac{V_p}{\gamma}, \qquad \text{(B-3)}$$

When z_0 tends to infinitive, $\hat{h}_e^2$

$$\hat{h}_e^2 = \frac{4\,V_p^2}{4(1+\gamma)^2}\left(\frac{1}{V_p}(z_0^2 + h_s^2)^{1/2} + \frac{\gamma}{V_p}(z_0^2 + h_r^2)^{1/2}\right)^2 - z_0^2, \qquad \text{(B-4)}$$

$$\hat{h}_e^2 = \frac{1}{(1+\gamma)^2}\left((z_0^2 + h_s^2)^{1/2} + \gamma\,(z_0^2 + h_r^2)^{1/2}\right)^2 - z_0^2. \qquad \text{(B-5)}$$

$$\hat{h}_e^2 = \frac{1}{(1+\gamma)^2}\left(z_0\left(1 + \frac{h_s^2}{z_0^2}\right)^{1/2} + \gamma\,z_0\left(1 + \frac{h_r^2}{z_0^2}\right)^{1/2}\right)^2 - z_0^2. \qquad \text{(B-6)}$$

The expression $(1+x)^{1/2}$ can be written in this way:

$$(1 + x)^{1/2} = 1 + \frac{x}{2} - \frac{x^2}{8} + \frac{x^3}{16} + \dots \qquad \text{(B-7)}$$

when x is very small,

$$(1 + x)^{1/2} \approx \left(1 + \frac{x}{2}\right), \qquad \text{(B-8)}$$

Therefore

$$\hat{h}_e^2 = \frac{1}{(1+\gamma)^2}\left(z_0\left(1+\frac{h_s^2}{2z_0^2}\right)+\gamma\, z_0\left(1+\frac{h_r^2}{2z_0^2}\right)\right)^2 - z_0^2, \tag{B-9}$$

$$\hat{h}_e^2 = \frac{1}{(1+\gamma)^2}\left(z_0(1+\gamma)+\left(\frac{h_s^2}{2z_0}+\frac{\gamma h_r^2}{2z_0}\right)\right)^2 - z_0^2, \tag{B-10}$$

$$\hat{h}_e^2 = \frac{1}{(1+\gamma)^2}\left(z_0{}^2(1+\gamma)^2 + 2z_0(1+\gamma)\left(\frac{h_s^2}{2z_0}+\frac{\gamma h_r^2}{2z_0}\right)+\left(\frac{h_s^2}{2z_0}+\frac{\gamma h_r^2}{2z_0}\right)^2\right) - z_0^2, \tag{B-11}$$

$$\hat{h}_e^2 = \frac{z_0{}^2(1+\gamma)^2}{(1+\gamma)^2} + 2z_0\frac{(1+\gamma)}{(1+\gamma)^2}\left(\frac{h_s^2}{2z_0}+\frac{\gamma h_r^2}{2z_0}\right)+\frac{1}{(1+\gamma)^2}\left(\frac{h_s^2}{2z_0}+\frac{\gamma h_r^2}{2z_0}\right)^2 - z_0^2, \tag{B-12}$$

$$\hat{h}_e^2 = z_0^2 + \frac{1}{(1+\gamma)}(h_s^2+\gamma h_r^2)+\frac{1}{(1+\gamma)^2}\left(\frac{h_s^2}{2z_0}+\frac{\gamma h_r^2}{2z_0}\right)^2 - z_0^2, \tag{B-13}$$

and finally

$$\hat{h}_{e_{z0z_0\to\infty}}^2 = \frac{(h_s^2+\gamma h_r^2)}{(1+\gamma)}. \tag{B-14}$$

APPENDIX C: HUSSAR GEOLOGY

Hussar area is located in central Alberta Plains, approximately 50 miles east to Calgary. A generalized statigraphic column for Hussar Area, is shown is Figure C.1.

The oil sands are contained within the Lower Cretaceous Mannville Group, specifically from Glauconitic sandstone, and Upper Mannville and from Pekiski formation the Rudle Group of Mississippian age (Acham, 1971). This field is currently operated by Husky, Cenovus Energy Inc, EnCana Corporation and Oil Points Energy Ltd (2012_annual_Pool_Schedule.xls in hppt://www.ercb.ca).

The Mannville Group and stata equivalent are present over most of the Western Canada Sedimentary Basin (WCSB). This group lies unconformably above carbonates upper Paleozoic and older Mesozoic rocks and is overlain by predominantly marine shale of the Colorado Group.

Mannville Group, known as oil sands were deposited mainly fluvial environment consists of interbedded continental sand and shale in the base, followed by a calcareous sandstone member, marine shale and glauconitic sandstone. Mannville Group was divided in central Alberta into lower and upper units of implied formational status. The Upper Mannville Formation is named Glauconitic sandstone due to the presence of glauconite within marine sandstones. The Glauconite sandstone is overlying by the continental sediments of the undifferentiated Upper Mannville consisting of sandstone, siltstone, shale and coal beds and is underlying by the calcareous shale and lime beds of the marginal Ostracod member (Okaro, 2001, Lynch, 2002).

Age	Stratigraphic Units		
Cretaceous	Belly River Group		Basal Belly River
	Colorado Group		Lea Park Formation
			First White Speckled Shale Formation
			Wapiabi Formation
			Cardium Formation
			Blackstone Formation
			Second White Speckled Shale Formation
			Belle Fourche Formation
			Fish scale Formation
			Westgate Formation
			Viking Formation
			Basal Col. / Joli Fou Formation
	Mannville Group	Upper	Upper Mannville Formation
			Glauconitic Formation
		Lower	Ostracod Formation
			Ellerslie Formation
			Cadomin Formation
			Detrital Formation
Mississippian	Rundle Group		Elkton Formation
			Sunda Formation
			Pekisko Formation
			Banff Formation
			Exshaw Formation

Shales

Carbonates (limestone, dolomite)

Clastic (sandstone, siltstones, conglomerates)

Figure C.1: Generalized bedrock stratigraphy for Hussar area. After ERCB, 2009

APPENDIX D: NORTHEASTERN BRITISH COLUMBIA GEOLOGY

The Horn River Basin and Cordova Embayment are located in northeastern British Columbia (NEBC) are bordered by the reef-fringed carbonate platform of the Middle Devonian Upper Keg River, Sulphur Point, and Slave Point formations. Basinal shales laterally-equivalent to these carbonate units comprise the Evie, Otter Park, and Muskwa members of the Horn River Formation. These shales, particularly Evie and Muskwa members have high silica and organic contents and are the main target of developing shale gas play in this area (McPhail, et al., 2008). A generalized statigraphic column for the Northeastern British Columbia Area, is shown is Figure D.1.

Evie Member overlies limestone and dolostones of the Lower Keg River Formation, is a package of highly radioactivity bituminous shales in the Horn River Formation. Above this member is Otter Park Member that is a calcareous shale. Otto Park Member is the least radioactive of the three members, while Muskwa is the highly radioactive and bituminous part of the Horn River Formation. Muskwa Member is radioactive, rich in organic matter, pyritic (Hickin et al, 2008).

Horn River Formation is overlying by the Redknife Formation. This formation is divided into the Jean Marie Member and an upper shale unit. The Jean Marie Member is composed of argillaceous, silty and dolomitic fossiliferous limestone. The upper unit consists of calcareous shales with silty limestone interbeds (Hickin et al, 2008).

Over an unconformably carbonate of Devonian age, is the Exshaw Formation of Mississippian age, that is composed of shale in the lower part and siltstone in the upper part. This formation is overlying by the Banff Formation.

Banff Formation consists of shales, bedded chart and carbonates. Above this formation is the Rundle Group that also contains important gas-bearing units (Hickin et al, 2008).

The base of the Cretaceous is marked by a regional unconformity. The Triassic Diaber Group is represented by the Montney Formation, and consists of siltstone, shale, and sandstone and is an important gas-bearing unit (Hickin et al, 2008).

The NEBC study area covers an area of approximately 379,000 hectares. The area lies east of the well-established Devonian Jean Marie gas production as well as deeper exploration targets such as Slave Point and Keg River carbonates and Muskwa, Otter Park and Evie formations. Over 335 well have been drilled in the basin since the late 1950s with only a handful targeting shale gas.

This field is currently operated by Nexen Inc, Penn West Energy Thrust and Canadian Natural Resources Ltd.
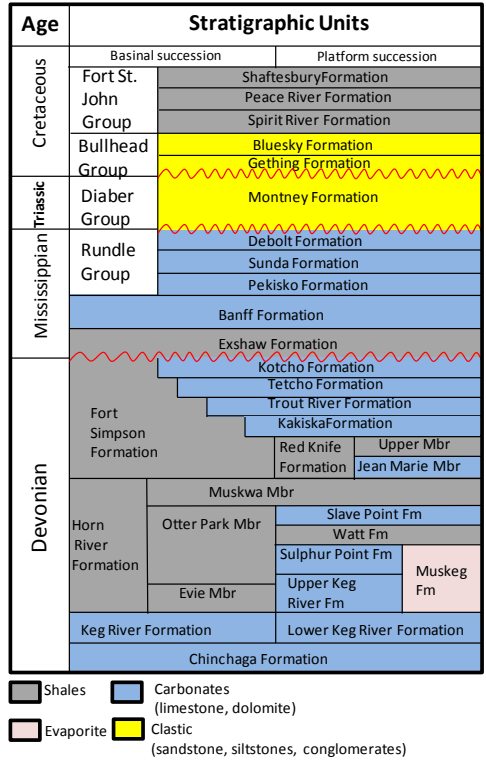
Figure D.1: Generalized bedrock stratigraphy chart along the northwestern part of the WCSB within NEBC and the relationship between shelf and offshelf sequences. After Hickin et al., 2008, McPhail et al., 2008 and Ferri et al., 2011.